TOWARDS A SURFACE CHEMISTRY AND MULTISCALE TEXTURATION TOOLKIT FOR THE SEPARATION AND HANDLING OF VISCOUS HYDROCARBONS

A Dissertation

by

THOMAS EDWARD O'LOUGHLIN

Submitted to the Office of Graduate and Professional Studies of
Texas A&M University
in partial fulfillment of the requirements for the degree of

DOCTOR OF PHILOSOPHY

Chair of Committee,	Sarbajit Banerjee
Committee Members,	Simon North
	James Batteas
	Matthew Sheldon
Head of Department,	Simon North

May 2018

Major Subject: Chemistry

ABSTRACT

The response of a liquid when placed onto a surface depends on the inherent properties of the liquid (cohesive forces within the liquid), the texturation of the surface (which can drastically increase the inherent wettability of surfaces or provide reentrant curvature), and the surface energy at the solid/liquid interface. This dissertation focuses on two main thrusts: (a) the separation of viscous oil and water emulsions using an inorganic membrane comprising ZnO nanotetrapods embedded on a stainless steel mesh to induce hierarchical texturation and exploit the surface-tension-mediated differential wettability of such fluids; and (b) the tuning of surface properties including mesoscale texturation and chemical functionalization to altogether prevent the wetting of surfaces by either oil or water by suspending liquid droplets in metastable states.

The properties of the surfaces can be drastically modified by changing the surface roughness on the micrometer scale and the nanometer scale, as well as by altering the chemistry of the surfaces by functionalizing them with self-assembled monolayers (SAMs). Understanding the influence of these parameters is critical for programmably defining the behavior of liquids and their emulsions when interacting with such surfaces. The development of methods for precisely defining the wettability of surfaces by fluids exhibiting complex rheological properties has implications for the separation of heavy oil/water emulsions, the transportation and handling of oil, and the cleanup of oil spills in marine environments. This dissertation describes the synthesis of such surfaces and membranes, as well as their tunability based on altering the loading of ZnO nanotetrapods and their functionalization with amorphous SiO_2 or perfluorinated phosphonic acid monolayers.

DEDICATION

This dissertation is dedicated to my parents, Ed and Karen, for their unwavering love and support with all my endeavors, and to my sister Helen for her help and guidance. Finally, to all my other friends and family; thank you.

ACKNOWLEDGMENTS

I would like to thank my advisor Professor Sarbajit Banerjee, for the years of guidance and support in my studies. His passion for science has inspired me, and his investment in my future has paved the way for experiences and opportunities I could not have imagined.

I would also like to thank my committee members, Professor Simon North, Professor James Batteas, and Professor Matthew Sheldon, for their guidance and support throughout the course of this research. Thank you to the office staff including Joanna Goodey-Pellois, Valerie McLaughlin, and Sandy Horton for their warm welcome to Aggieland and their help as I transitioned to Texas A&M.

Thank you to my friends and the faculty and staff in the Chemistry Department at the University at Buffalo for their support of the beginning of my graduate career.

Thanks to all the current and past members of the Banerjee group for their support, and friendship. I couldn't have asked to work with a better group of scientists. Your camaraderie and insight helped me along this journey.

Lastly, many thanks to all my undergraduate professors, especially to Professor Jeffrey Peterson for his inspiration to push myself beyond what I believed I could do – by simply placing one foot in front of the other; and to Professor David Geiger for the opportunity to gain valuable undergraduate laboratory experiences that helped shape my passion for scientific research.

CONTRIBUTORS AND FUNDING SOURCES

This work was supervised by a dissertation committee consisting of my advisor Professor Sarbajit Banerjee, and my committee members, Professor Simon North and Professor Matthew Sheldon of the Chemistry Department, and Professor James Batteas of Materials Science and Engineering.

Karl Fischer titrations in Chapter III were performed by Christopher Komatsu of the Department of Chemistry at Texas A&M University.

All other work for the dissertation was completed by the student, under the advisement of Professor Sarbajit Banerjee of the Department of Chemistry.

We gratefully acknowledge Cenovus Energy, Inc. for support of this work.

TABLE OF CONTENTS

Page

ABSTRACT ii

DEDICATION iii

ACKNOWLEDGMENTS iv

CONTRIBUTORS AND FUNDING SOURCES v

TABLE OF CONTENTS vi

LIST OF FIGURES ix

LIST OF TABLES xvii

CHAPTER I INTRODUCTION AND MOTIVATION 1

I.1 Deciphering the Lotus Leaf and Other Lessons in Fluid Dynamics from Nature 6
I.2 The Balance of Forces: Some Physical Principles Underpinning Wettability 8
I.3 Rough at the Edges: Influence of Surface Roughness on Wettability 11
I.4 The Design of Orthogonally Wettable Surfaces 16
I.5 Man versus Rust: In Search of Universal Non-Wettability 19
I.6 Texturation and Surface Chemistry: Mimicking Biological Surfaces to Obtain Universal Non-Wettability 22
I.7 References 25

CHAPTER II ORTHOGONAL WETTABILITY OF HIERARCHICALLY TEXTURED METAL MESHES AS A MEANS OF SEPARATING WATER/OIL EMULSIONS 30

II.1 Outline 30
II.2 Introduction 31
II.3 Experimental Details 33
II.3.1 Materials 33
II.3.2 Characterization 34
II.3.3 Separations 35
II.4. Results and Discussion 36
II.5 Conclusions 48
II.6 References 49

CHAPTER III SEPARATION OF VISCOUS OIL EMULSIONS USING 3D NANOTETRAPODAL ZNO MEMBRANES 52

III.1 Outline 52
III.2 Introduction 53
III.3 Materials and Methods 56
III.3.1 Preparation of ZnO Tetrapods 56
III.3.2 Preparation of ZnO Tetrapod/Stainless-Steel Mesh Membranes 56
III.3.3 Characterization of ZnO Tetrapods and Membranes 57
III.3.4 SAGD Emulsions 57
III.3.5 Separation of Emulsions 58
III.4 Characterization of Permeate 59
III.5 Results and Discussion 59
III.4. Conclusions 70
III.5 References 70

CHAPTER IV MODIFYING BASE METAL SUBSTRATES TO EXHIBIT UNIVERSAL NON-WETTABILITY: EMULATING BIOLOGY AND GOING FURTHER ... 74

IV.1 Introduction 74
IV.2 Experimental 77
IV.2.1 Steel Substrates and Etching Conditions 77
IV.2.2 Synthesis of ZnO Nanotetrapods 78
IV.2.3 Coating of ZnO Nanotetrapods onto Steel Substrate 78
IV.2.4 Characterization of Etched Metal Surfaces 79
IV.2.5 Characterization of ZnO Nanotetrapods 80
IV.2.6 Contact Angle Measurements 80
IV.2.7 Adhesion Testing 81
IV.2.8 Thermal Analysis 81
IV.3 Results and Discussion 81
IV.3.1 Constructing an Artificial Plastron: A Process Outline for Achieving Universal Non-Wettability on Steel Surfaces 81
IV.3.2 Microscale Texturation by Selective Etching 84
IV.3.3 Nanoscale Texturation Using ZnO Nanotetrapods 91
IV.3.4 Adhering ZnO Nanotetrapods to Steel Substrates: Mechanical and Thermal Stability 95
IV.3.5 Surface Functionalization with Molecular Monolayers: Modulating Surface and Interfacial Energies 98
IV.4 Conclusions 106
IV. 5 References 107

CHAPTER V BIOMIMETIC PLASTRONIC SURFACES FOR HANDLING OF VISCOUS HEAVY OILS .....

V.1 Outline 109
V.2 Introduction 110

V.3 Materials and Methods 112
V.3.1 Characterization 112
V.4 Results and Discussion 113
V.5 Conclusions 125
V.6 Associated Content 125
V.7 References 126

CHAPTER VI OUTLOOK, SUMMARY, AND OTHER STRATEGIES 129

VI.1 Introduction 129
VI.2 Experimental Methods for Preparation of Colloidally Templated TiO_2 Surfaces 131
VI.2.1 Preparation of Polystyrene Spheres 131
VI.2.2 Fabrication of TiO_2 Coatings 131
VI.2.3 Characterization 132
VI.3 Colloidally Templated TiO_2 Coated Surfaces: A Potential Addition to the Omniphobic Toolkit 132
VI.4 Future Outlook: Pipeline Coatings 138
VI.4.1 Methodology 138
VI.4.2 Constructing and Benchmarking of an Apparatus for Testing of Fluid Flow 140
VI.4.3 Measurement of Pressure Drops across Coated Tubes 141
VI.5 References 142

APPENDIX A FIGURES 143

LIST OF FIGURES

Page

Figure I.1. A chart displaying the projected global energy consumption by source.[1] Source: U.S. Energy Information Administration (September 2017). 2

Figure I.2. Schematic of the steam-assisted gravity drainage method. In this scheme, two horizontal wells are drilled where steam is injected from the top pipeline (denoted as the injector well), thus creating a steam chamber where the water condenses and the water and oil emulsion flows to the bottom pipeline (denoted as the producer well) for extraction. Reproduced with permission from Connacher Oil & Gas/jwnenergy.com.[4] 4

Figure I.3. Examples of micro and nanoscale texturation in nature that give rise to unusual wettability. Scanning electron microscopy (SEM) images showing micro and nano texturation for A-E) a lotus leaf at different magnifications.[16] Adapted with permission from Beilstein-Institut, Hans J. Ensikat, Petra Ditsche-Kuru, Christoph Neinhuis, and Wilhelm Barthlott, *Belstein Journal of Nanotechnology*, 2011, 152-161. Copyright 2011. F) Digital photograph of a pond skater and SEM image of G) pond skater legs.[8] Adapted with permission from Elsevier, Bharat Bhusan and Yong Chae Jung, *Progress in Materials Science*, 2010, 1-108. Copyright 2011. 7

Figure I.4. Contact angle of a liquid droplet illustrating the balance of forces between interfacial energies. 9

Figure I.5. A) Wenzel regime, representing equilibrium wettability for a rough surface. B) Cassie—Baxter regime representing a metastable suspended state. 12

Figure I.6. SEM images of the integument of a water-walking insect called *Mesovelia* (A-D). The image depicts intermittent and waxy hairs that trap a plastron air bubble. The air trapped in the bubble allows the insect to breathe while underwater. E) Schematic of a plastron geometry designed to trap air.[39] Adapted with permission from Cambridge University Press, Flynn, M. R.; and Bush, J. W. M. *The Journal of Fluid Mechanics*, 2008, 275-296. Copyright 2008. 16

Figure I.7. Optical microscopy image of a SAGD emulsion with a water content of ca. 30 vol.%. The lighter regions correspond to water droplets and darker solid particles are asphaltene residues and silt particles. 18

Figure I.8. Classical photographs from the United States Library of Congress depicting rust degradation (A) of a vehicle and (B) a bridge in the United States. Reproduced from The Library of Congress, Carol M. Highsmith archive. 20

Figure II.1. A schematic representation illustrating the fabrication of surfaces for separating water/oil emulsions. The generation of the ZnO tetrapods and their

subsequent coating onto meshes is depicted. The obtained membranes strongly repel water while allowing for rapid permeation of oil droplets, providing a means for separating the water and oil constituents of emulsions under ambient flow conditions based entirely on differential wettability. 38

Figure II.2. (A-D) SEM images depicting the multiscale textured metal meshes modified by the deposition of ZnO nanotetrapods at various magnifications. (A) Several pores of the metal mesh with spray-deposited ZnO nanotetrapods; (B) Magnified view of a single stainless steel pore wherein interconnected ZnO nanotetrapods define multiscale porosity; (C) Magnified view of a nanotetrapod network and the resulting pore structure; (D) a single free-standing ZnO tetrapod. (E) Raman spectra and (F) XRD pattern acquired for ZnO nanotetrapods. The XRD pattern also indicates the reflections of the hexagonal zincite phase. 39

Figure II.3. Contact angles measured for (A) water on the stainless steel mesh and (B) water on the mesh coated with ZnO nanotetrapods. C—E) Hexadecane exhibits flash spreading to a contact angle of 0° on the coated mesh substrate as indicated by the sequences of images acquired at 0, 0.24, and 0.48 s..... 41

Figure II.4. (I) Schematic illustration of the experimental configuration deployed for water/oil separation. The inset depicts a digital photograph of water droplets (with a blue dye) that do not wet a stainless steel mesh with a spray-deposited coating of ZnO nanotetrapods. (II) A) 1:1 emulsion of water and hexadecane where the aqueous phase has been colored blue by inclusion of a blue dye; the subsequent images show the roll-off fraction (left) and permeate fraction (right) in each instance after effective separation lengths of (C) 21 cm; (D) 35 cm; (E) 60 cm; (F) 130 cm; and (G) 200 cm. In each instance, the emulsified hexadecane and water mixture is allowed to settle after the experiment prior to taking a digital photograph. 42

Figure II.5. (A) Plot of water purity (as defined in the text) as a function of the effective length of the hierarchically textured substrate. The plot is nicely described by a Boltzmann fit as discussed in the text. (B) Efficacy of separation (water purity of roll-off fraction) at an arbitrary path length of 21 cm for different surface treatments. The blank steel mesh is contrasted to the mesh functionalized with heptadecafluoro-1,1,2,2-tetrahydrodecyl)trimethoxysilane and n-octadecyltrichlorosilane. 44

Figure III.1. Process Flow Diagram for the Preparation of ZnO/Stainless Steel Mesh Membrane Architectures and their Utilization in the Separation of SAGD Emulsions. (A) Schematic depicting preparation of ZnO tetrapods from Zn metal; (B) collection and subsequent dispersion of ZnO tetrapods within 2-propanol by ultrasonication; (C) spray coating of ZnO tetrapods dispersed in 2-propanol onto 316 stainless steel mesh substrates with variable pore dimensions; (D) coating with TEOS to increase adhesion of tetrapods to the stainless steel mesh by constituting an interfacial SiO_2 layer; (E) deployment of

the membrane architectures under hydrothermal conditions to bring about the separation of SAGD emulsions based on the differential wettability of water and viscous oil towards these surfaces. 61

Figure III.2. Texturation and Porosity of 3D Nanotetrapodal Membrane Architectures. A—E) SEM images depicting stainless steel meshes exhibiting multiscale texturation as a result of the deposition of ZnO nanotetrapods. In A—E, the mesh size is altered whilst maintaining the ZnO loading constant at ca. 7.0 mg/cm^2. The meshes have square pores defined here by the edge dimensions. A) A 180-gauge textured stainless steel mesh with a pore size of ca. 84 μm; B) 250 gauge textured stainless steel mesh with a pore size of ca. 61 μm; C) 325-gauge textured stainless steel mesh with a pore size of ca. 43 μm; D) 400 gauge textured stainless steel mesh with a pore size of ca. 38 μm; E) 500-gauge textured stainless steel mesh with a pore size of ca. 30 μm. F) SEM image of individual ZnO tetrapods at increased magnification..... 62

Figure III.3. Optical Microscopy Examination of SAGD Emulsions and Permeates: A,B) Optical microscopy image of a SAGD emulsion with a water content of *ca.* 30 vol.%; C,D) optical microscopy images acquired for permeate collected using a 250-gauge mesh membrane with a pore size of 61 μm loaded with 14 mg/cm^2 of ZnO tetrapods; Dean-Stark's distillation indicates that water content within this is sample is *ca.* 14 vol.%. E,F) Optical microscopy images acquired for a permeate fraction collected using a 325-gauge mesh with a pore size of 43 μm loaded with 14 mg/cm^2 of ZnO tetrapods; Dean—Stark's distillation suggests a water content of *ca.* 10 vol.% for this sample. G,H) Optical microscopy images acquired for a permeate fraction collected using a 400-gauge mesh with a pore size of 38 μm loaded with 14 mg/cm^2 of ZnO tetrapods; Dean—Stark's distillation suggests a water content of *ca.* 1 vol. %. I,J) Optical microscopy images acquired for a permeate fraction collected using a 500-gauge mesh with a pore size of 30 μm loaded with 14 mg/cm^2 of ZnO tetrapods; Karl—Fischer titration suggests a water content of *ca.* 0.69 vol. %. The lighter regions correspond to water droplets and darker solid particles are asphaltene residues and silt particles. 65

Figure III.4. Water content and permeation temperature plotted as a function of pore size for varying loadings of ZnO tetrapods with false color map overlaid for clarity. 68

Figure III.5. (A) 3D plot depicting the variation of the flux rate as a function of the pore size and the ZnO loading within the membrane architecture. (B) Plot of the flux rate as a function of the pore size at different ZnO loadings. (C) 3D plot depicting the variation of the water content as a function of the pore size and ZnO loading on the membrane. (D) Plot of the water content as a function of the pore size at different ZnO loadings. 69

Figure IV.1. Water repellency of ant rafts. (A) An individual ant's exoskeleton is moderately hydrophobic, as shown by the contact angle of the water drop. (B) Enhanced water repellency of a raft of ants, as shown by the increased contact

angle of the water drop. (C) Buoyancy and elasticity of the ant raft, as shown by attempted submersion by a twig. (D) The plastron air bubble of an ant in soap-free water. The bubble makes the ant buoyant, necessitating the use of a thread to hold it underwater. (E) An air pocket trapped in a submerged ant raft. The shimmery layer around the ants is the air–water interface. Reproduced with permission from Mlot, N. J.; Tovey, C. A; Hu, D. L. *Proc. Natl. Acad. Sci. U. S. A.* 2011, *108* (19), 7669–7673. 75

Figure IV.2. Schematic illustration of process flow used to prepare omniphobic surfaces integrated onto etched carbon steel. The top panel shows the synthesis of ZnO nanotetrapods by oxidation of Zn metal in an air environment. (a) The steel substrate is etched with acid to define microscale texturation. (b) ZnO nanotetrapods are spray-coated onto the etched carbon steel, thereby adding nanoscale texturation. (c) TEOS is subsequently spray-coated onto the ZnO/etched steel substrates to form a siloxane linkage between the etched steel and ZnO nanostructures. (d) The substrates are functionalized with perfluorinated silanes (or perfluorinated phosphonic acids). The resulting hierarchically textured surfaces trap air pockets below the tetrapods, thereby creating a plastronic architecture. (e) The textured surfaces exhibit a low surface energy by dint of the pendant fluorous phase, thereby yielding omniphobic behavior. 83

Figure IV.3. Optical micrographs obtained at 20× and 50× magnifications indicating the surface topographies of roughened carbon steel surfaces upon chemical etching. The specific etching solutions used are indicated in the figure. 86

Figure IV.4. SEM images of etched carbon steel surfaces. (A,B) SEM images of cleaned A36 carbon steel substrates. (C,D) SEM images of A36 carbon steel substrates upon etching with a mixed acid solution at 93°C for 45 s. Clear terraces are evident, separated by distances of 500nm to 1 μm. However, the steps are generally free of nanoscale topographies. (E,F) SEM images of A36 carbon steel substrates etched using an HCl solution at 80 °C for 1 h, depicting deeper etch pits with accompanying nanoscale porosity. 88

Figure IV.5. Water contact angles of (A) cleaned blank steel, (B) steel after etching with mixed acid solution at 93°C for 45 s. (C) and (D) represent the water contact angles measured for (A) and (B) after immersion in a 2.7 mM butanol solution of nonafluorohexlytriethoxysilane, respectively. 90

Figure IV.6. Water contact angles of (A) cleaned blank steel, (B) steel after etching in HCl solution at 80°C for 1 h. (C) and (D) represent the water contact angles measured for (A) and (B) after immersion in a 2.7 mM butanol solution of nonafluorohexlytriethoxysilane, respectively. 91

Figure IV.7. SEM images of different ZnO morphologies obtained from oxidation of metallic Zn at different oxygen partial pressures.[48] A,B) nanowire arrays, C) nanocombs, and D) nanotetrapods. Adapted with permission from *ACS Applied*

Materials & Interfaces 2013, *5*, 10650-10657. Reproduced by permission of the American Chemical Society. 92

Figure IV.8. Defining nanotexturation using ZnO nanotetrapods. A, B) SEM images acquired for individual ZnO nanotetrapods indicating the four protuberant and tapered arms. The tetrapod morphology results inevitably results in the trapping of air pockets between the nanotetrapods and the base substrate, thereby giving rise to the Cassie-Baxter suspended droplet regime and stabilizing plastrons. C, D) SEM images depicting interconnected ZnO nanotetrapods residing on etched steel substrates. (E) Raman spectra and (F) XRD pattern acquired for ZnO nanotetrapods. The XRD pattern also indicates the reflections of the hexagonal zincite phase (JCPDS 36-1451). Reflections derived from residual Zn are marked with an asterisk. 94

Figure IV.9. A-C) A ZnO nanotetrapod layer adhered to a steel substrate, etched with an HCl solution, using TEOS as the precursor to constitute a SiO_2 layer; D-F) A ZnO nanotetrapod layer adhered to a steel substrate, etched with a mixed acid solution, using TEOS as the precursor to constitute a SiO_2 layer. The panels show SEM images at increasingly higher magnifications..... 96

Figure IV.10. A) Zinc, B) oxygen, C) flourine, and D) carbon energy dispersive X-ray maps of ZnO nanotetrapod samples functionalized with a perfluorinated silane, (heptadecafluoro-1,1,2,2-tetrahydrodecyl) trimethoxysilane. The energy dispersive X-ray maps (A-D) have correspond to a 15 μm x 15 μm area. E) The EDX spectrum of the sample area analyzed in (F). (F) SEM image of the perfluorinated ZnO nanotetrapods; the yellow box delineated the region mapped by EDX. (G) attenuated total reflection (ATR) FTIR spectra of TEOS-coated ZnO soaked for 1 h in a 2.7 mM butanol solution of (heptadecafluoro-1,1,2,2-tetrahydrodecyl)trimethoxysilane. 97

Figure IV.11. Hexadecane contact angles of (A) cleaned blank steel, (B) fluorinated cleaned blank steel, (C) steel etched with HCl at 80°C for 1 h and fluorinated, (D) steel etched with HCl at 80°C for 1 h, coated with ZnO nanotetrapods, and fluorinated, (E) steel etched with HCl at 80°C for 1 h, coated with ZnO nanotetrapods, TEOS coated, and fluorinated. F-J) heavy oil contact angles for samples A-E, respectively. In all cases, surface functionalization was achieved by immersion in a 2.7 mM butanol solution of the C6 perfluorinated silane for 1 h. 100

Figure IV.12. (A) Water contact angles of carbon steel after etching with HCl:H_2O solution at 80°C for 1 h, deposition of 7.8 mg/cm^2 of ZnO nanotetrapods, and surface functionalization with a 27.0 mM THF solution of 1H,1H,2H,2H-perfluorooctanephosphonic acid. (B) demonstrates the contact angle for heavy oil on the same sample. 104

Figure V.1. (A) Schematic depiction of a plastronic architecture designed to glide heavy oil droplets. ZnO tetrapods shown in (B) are arrayed onto a microtextured

stainless steel mesh. The ZnO nanotetrapods are further functionalized with 1H,1H,2H,2H-perfluorooctanephosphonic acid that forms a self-assembled monolayer as depicted in (C). 114

Figure V.2. SEM images of (A) a stainless steel mesh with a pore size of ca. 84 μm coated with ZnO tetrapods; (B) magnified view of a single pore of the ZnO-coated mesh; (C) a lone tetrapod suspended on the stainless steel mesh; (D) an interconnected network of ZnO tetrapods. 115

Figure V.3. Contact angles measured for A,D) a bare stainless steel mesh; B,E) stainless steel mesh with 7 mg/cm^2 of ZnO tetrapods; and C,F) the ZnO-coated mesh further functionalized with of 1H,1H,2H,2H-perfluorooctanephosphonic acid. The top images correspond to water contact angles, whereas the bottom images correspond to heavy oil contact angles. G) Digital photograph of water and sales oil droplets on a functionalized ZnO-coated mesh. Air pockets are discernible below the droplet. H, I) Digital photographs of a dry functionalized ZnO-coated mesh and a mesh immersed in water. 118

Figure V.4. SEM image depicting a single ZnO tetrapod functionalized with 1H,1H,2H,2H-perfluorooctanephosphonic acid (A) and corresponding EDX maps depicting the distribution of zinc (B), oxygen (O), and fluorine (D). E) Integrated EDX spectrum acquired for the tetrapod. (F) C 1s, (G) O 1s, and (H) F 1s high-resolution XPS spectra acquired for functionalized ZnO tetrapods. 119

Figure V.5. (A) FTIR ATR spectra (A) of 1H,1H,2H,2H-perfluorooctanephosphonic acid (black) and 1H,1H,2H,2H-perfluorooctanephosphonic acid functionalized ZnO tetrapods (red). (B) A representation of the helical structure of 1H,1H,2H,2H-perfluorooctanephosphonic acid attached to ZnO. 122

Figure V.6. Time lapse images of heavy oil droplets placed on a (A) ZnO-coated and fluorinated mesh contrasted to (B) images acquired for untreated mesh substrate. Video A.4 (Supporting Information) illustrates the stark contrast between these samples. 124

Figure VI.1. Scanning electron microscopy images of templated 40 nm (A, B), 800 nm (C, D), and 1500 nm (E, F) TiO_2 nanoparticles with microscale pores that have been generated by the permeation of TiO_2 particles within interstitial domains of inverse opal structures constituted from polystyrene spheres, followed by subsequent removal of polystyrene spheres upon annealing of the coated substrates at 400°C for 2 h. The relative ratio of TiO_2 nanoparticles:PS spheres was maintained at a constant at 1:1 (w/w). 134

Figure VI.2. Contact angles for water (A) and viscous oil (B) on templated TiO_2 nanoparticle coatings built from 40 nm TiO_2 particles, water (C) and viscous oil (D) on templated TiO_2 nanoparticle coatings built from 800 nm TiO_2 particles, and water (E) and viscous oil (D) on templated TiO_2 nanoparticle coatings built from 1500 nm TiO_2 particles. All surfaces were made with 1:1 (w/w)

TiO_2:polystyrene coatings on A36 steel substrates and subsequently treated with 2.7 mM 1H,1H,2H,2H perfluorooctane phosphonic acid for a period of 1 hour..... 136

Figure VI.3. Scanning electron microscopy images of different ratios of TiO_2 nanoparticles: polystyrene spheres examined at different loading ratios: 9:1 (A), 8:2 (B), 7:3 (C), 6:4 (D), 4:6 (E), 3:7 (F), 2:8 (G), and 1:9 (H). The particles have been templated onto A36 steel substrates in each case..... 137

Figure VI.4. Contact angles for water and viscous oil of 9:1 (A), 8:2 (B), 7:3 (C), 6:4 (D), 4:6 (E), 3:7 (F), 2:8 (G), and 1:9 (H) TiO_2:polystyrene (w/w) templated into A36 steel substrates. All substrates were treated by soaking in a 2.7 mM 1H,1H,2H,2H perfluorooctane phosphonic acid solution for 1 hour. 138

Figure VI.5. Schematic depictions of two methods for the application and construction of coated pipelines. 140

Figure VI.6. Schematic representation of a possible flow system to be used for pressure drop measurements across a coated pipeline..... 141

Figure A.1. Three different configurations of ZnO nanotetrapods on A36 steel were tested with ASTM D3359 (A). The configuration with a topcoat of TEOS exhibiting drastically improved adhesion with the highest rating of 5B. The top row of A demonstrates the pristine ZnO with a TEOS coating on top; the middle row represents the samples after scribing using a specified scribing tool; and the bottom row displayes the coatings after application and removal of a standardized adhesive tape. ASTM D2197 testing (B) was performed on the sample configuration of ZnO basecoat with a TEOS topcoat. Comparing unmodified ZnO scrape test (B, left) to that of ZnO with a SiO_2 topcoat (B, right) an improvement of 405-550 g was noted. 143

Figure A.2. SEM images at increasing magnification from A to C of ZnO tetrapods integrated onto a stainless steel mesh after functionalization with heptadecafluoro-1,1,2,2-tetrahydrodecyl)trimethoxysilane. The interconnected network of nanotetrapods is preserved after functionalization. 144

Figure A.3. (A) SEM image of an individual ZnO tetrapod. The average length of each of the tetrapod arms is ca. 3.93 μm the average diameter is ca. 0.56 μm. (B), (C) Geometrical reconstruction of the tetrapods approximating the arms as cones. A roughness *r* value of 4.5, is deduced based on these dimensions, and is defined as the ratio of the surface area of an individual tetrapod as compared to the surface area of a smooth surface. 145

Figure A.4. Digital photographs acquired before and after separation of the emulsion. (A) A custom glass insert where the ZnO-tetrapod-coated stainless steel mesh is held between rubber o-rings and the emulsion is placed on top and allowed to permeate at a programmed temperature and pressure. (B) A decanted portion of

the fraction that remains on top of the membrane. The brown coloration is characteristic of produced water contains clay and silt debris. (C) Digital photograph of the top of the membrane containing retained water with soil debris. The membrane utilized in this instance comprises a 180 gauge mesh with a pore-size of 84 μm with a ZnO loading of 7.0 mg/cm^2. (D) The permeated oil, which is darker in color as compared to the original emulsion and contains no visible water. (E) Digital photograph of the bottom of the membrane. The black color is characteristic of permeated viscous oil. 146

Figure A.5. Heating rate of the thermal autoclave as a function of time. The autoclave vessel is filled with 250 mL of deionized water in order to generate steam and replicate the high temperature and pressure conditions characteristic of the SAGD process. The vessel is heated from room temperature (22°C.) to a maximum temperature of 175°C. 147

Figure A.6. Evolution of autogenous pressure as a function of temperature upon heating water within the thermal autoclave used for separation of SAGD emulsions. In this experiment, the autoclave vessel is filled with 250 mL of deionized water in order to generate steam and replicate the high temperature and pressure conditions characteristic of the SAGD process. The vessel is heated from room temperature (22°C) to a maximum temperature of 175°C yielding a maximum pressure of 106 psi at the highest temperature. 148

Figure A.8. SEM image of ZnO tetrapods after surface functionalization with PFOPA. No discernible changes in morphology are observed upon functionalization. 150

Figure A.9. FTIR ATR spectra of PFOPA (black) and PFOPA-functionalized ZnO tetrapods (red). 151

Figure A.10. Thermogravimetric analysis of (A) ZnO tetrapods and (B) PFOPA-functionalized ZnO tetrapods. 152

Figure A.11. Images of contact angles of water on a PFOPA functionalized ZnO coated stainless steel mesh. Here the droplets contact the surface (A) and are completely removed during the dynamic angle measurements (B-D) due to the extreme hydrophobic behavior, precluding an accurate measurement while displaying the complete inability of water to adhere to the surface. 153

LIST OF TABLES

Page

Table IV.1 Water contact angles for carbon steel substrates subjected to different etching conditions to define micro- and nanoscale texturation. Contact angles are listed for freshly etched samples. Water contact angles were acquired in triplicate for each sample and are presented as the mean and the standard deviation. 89

Table IV.2. Selected water, hexadecane, and heavy oil contact angles measured for micro- and nanotextured steel substrates with ZnO nanotetrapods (optimized at 7.8 mg/cm^2) and TEOS (optimized at 3.9 μL/cm^2) and upon functionalization with either the C6 perfluorinated silane or perfluorinated phosphonic acid. The "best-in-class" sample is highlighted in bold. 101

CHAPTER I

INTRODUCTION AND MOTIVATION[*]

Although the use of renewable energy is projected to grow, given the sharp forecasted increase in worldwide energy demands it is unclear whether such energy vectors will be able to entirely bridge the anticipated global energy deficit. Therefore, the continued dependence on traditional fossil fuels is expected to persist in the foreseeable future barring transformative breakthroughs that much more rapidly accelerate the adoption of clean energy (**Figure I.1**). In order to meet the sharp projected increase in energy consumption, it will be imperative to access unconventional petroleum deposits such as the Canadian Oil Sands in Alberta and Saskatchewan. Current estimates by the Energy Information Administration (EIA) peg accessible deposits within this region at approximately 170 billion barrels, which would allow for 100 years of production while maintaining Canada's current production rate of 4.6 million barrels per day.[1]

[*] Reproduced with permission from "Modifying Base Metal Substrates to Exhibit Universal Non-Wettability: Emulating Biology and Going Further." O'Loughlin, T.E.; Waetzig, G. R.; Davidson, R. E.; Dennis, R. V.; Banerjee, S. *Encycl. Inorg. Bioinorg. Chem.* **2017**, p.1. Reproduced by permission of John Wiley & Sons, Inc.

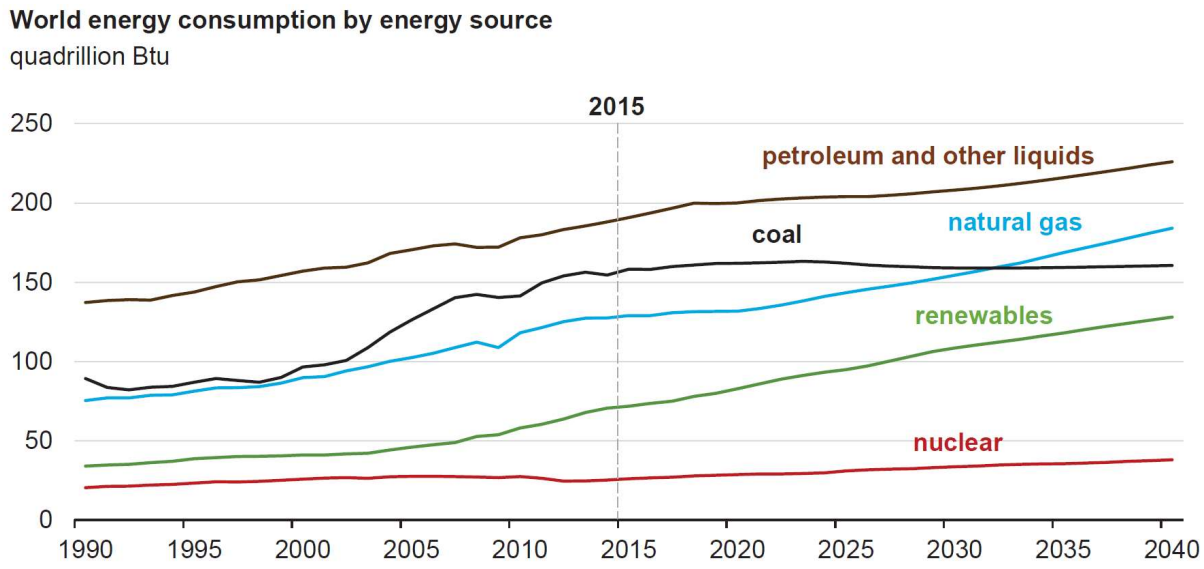

Figure I.1. A chart displaying the projected global energy consumption by source.[1] Source: U.S. Energy Information Administration (September 2017).

In order to utilize this abundant energy resource and to ensure energy security, previously insurmountable challenges must be addressed, specifically in extracting these deep bituminous deposits from the Canadian Oil Sands. The extremely high viscosity of these bituminous deposits prevents the use of conventional methods of oil extraction that are used for lighter crude oil in West Texas or the Middle-East. In order to extract heavy oils, a variety of enhanced oil recovery (EOR) methods have been developed. These methods include the use of chemicals such as surfactants and polymers; CO_2 injection; and thermal injection methods such as cyclic steam stimulation, steam flooding, and the steam-assisted gravity drainage method (SAGD).[2,3] All of these EOR methods are underpinned by the same essential principle related to the challenging rheological properties of heavy oil, requiring that the viscosity of heavy oil be reduced in order to allow it to flow and be pumped to the surface for transportation and processing.

Cyclic steam stimulation utilizes high-pressure steam injection *via* a vertical pipeline over a period of days or weeks, wherein the steam is allowed to permeate and heat the oil, thereby reducing its viscosity. The oil and water are then extracted using the same pipeline that was used to inject the steam. In contrast, steam flooding utilizes a continuous supply of steam through vertical injection wells to heat and loosen the oil deposits and drive them under a pressure gradient towards a second vertical well that is used to extract the water and oil. Such a continuous injection process has the additional benefit of using displacement while injecting the steam to help drive the oil towards the extraction well.

SAGD, which has emerged as the pre-eminent extraction method at the current time, goes further than other thermal injection methods by including the use of a horizontal injection well to insert high-pressure steam for a period of days or weeks, then using a second horizontal production, well, which is drilled 3—5 m below the injection well, to collect the complex oil and water emulsion (**Figure I.2)** where it is collected as a result of gravity drainage. In addition, the use of horizontal wells creates a long steam chamber that is parallel to the hydrocarbon deposit, thereby increasing the recovery factor (R_f) (defined as the percent of original oil in place that can be produced relative to the total deposit) both by increasing the size of the steam chamber as well as keeping the viscous oils hot and thereby reducing their viscosity and aiding in their extraction.[2,3]

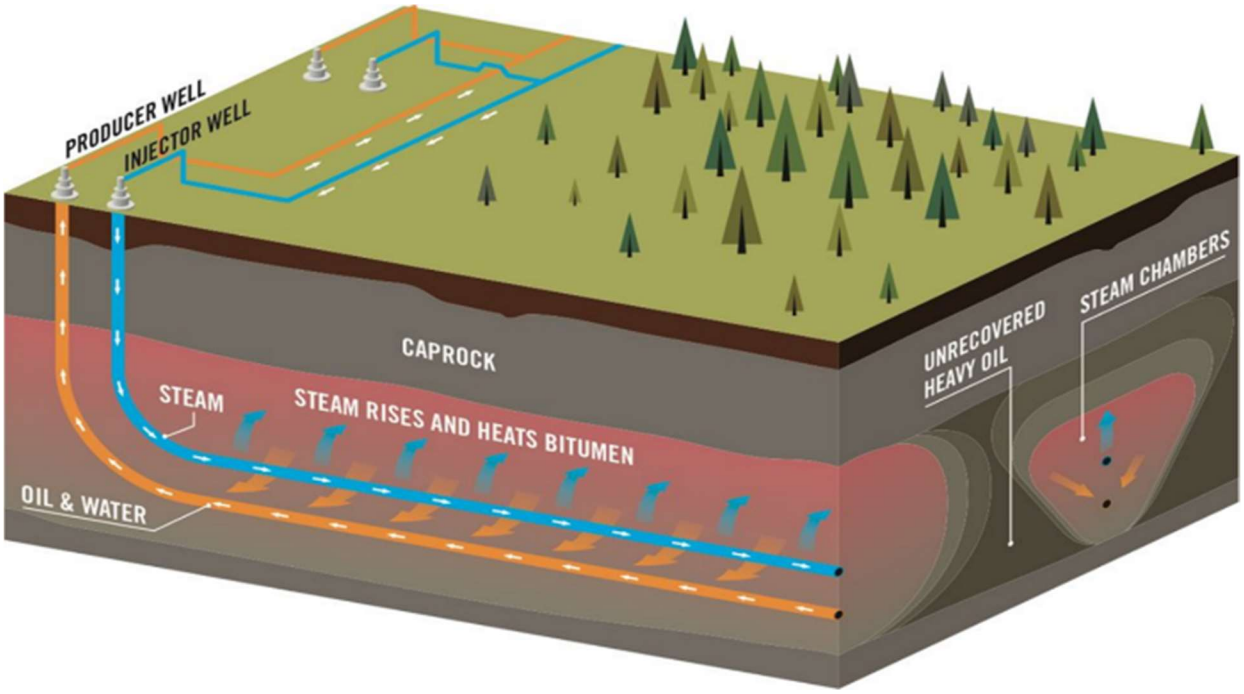

Figure I.2. Schematic of the steam-assisted gravity drainage method. In this scheme, two horizontal wells are drilled where steam is injected from the top pipeline (denoted as the injector well), thus creating a steam chamber where the water condenses and the water and oil emulsion flows to the bottom pipeline (denoted as the producer well) for extraction. Reproduced with permission from Connacher Oil & Gas/jwnenergy.com.[4]

While effective in reducing the viscosity of and extracting viscous oil, the SAGD method is beset by challenges related to the separation of the viscous oil and water emulsions. Owing to the high temperature and mechanical agitation required during the injection of steam and stabilization of the steam chambers, as well as the presence of endogenously occurring surfactants such as humic acids, SAGD generates complex and stable oil-in-water or water-in-oil type emulsions. Separating these emulsions is a critical imperative both for the drying of oil for further processing, as well as for subsequent purification of the "produced" water for reuse in the next SAGD cycle as dictated by stringent environmental regulations. For all of these challenges associated with SAGD, the differences in wetting of water and oil phases may be exploited to

help devise separations using fundamental physical principles, specifically understanding and utilizing the differential in surface tension between hydrocarbons and water.

An additional challenge common to all extraction methods relates to the handling and transportation of oil and the cleaning of oil-laden surfaces. Once separated, the heavy oil again becomes extremely viscous upon cooling. In order to transport and process these liquids exhibiting challenging rheological characteristics, large quantities of diluents, typically low molecular weight hydrocarbons, must be added. Furthermore, pipelines and railcars used for the transportation of oil from the Oil Sands to refineries (typically along the Gulf Coast of the United States) suffer greatly from fouling and the loss of residual oils on surfaces, respectively. The costs of manual labor and risk to human health associated with oil handling and cleaning of railcars and storage containers is yet another factor that cannot be understated. This dissertation will focus on (i) the separation of viscous oil and water emulsions utilizing an entirely inorganic membranes system of ZnO nanotetrapods embedded onto a stainless steel mesh by exploiting the differential wettability of each liquid, and (ii) development and tuning of surface properties such as mescoscale texturation and chemical functionalization to prevent the wetting of surfaces by oil and water.

In order to design surfaces that can better handle fluids exhibiting complex rheological behavior, it is worthwhile reviewing the toolkit that organisms use to direct the permeation and flow of liquids. Nature holds valuable lessons that are tremendously instructive in its ability to separate and flow water based on a careful combination of hierarchical texturation and surface polarity. The creation of physical analogues of such natural fluid handling systems is the primary focus of this dissertation with the added complexity of having to address a high viscosity and low surface tension liquid that is relatively seldomly encountered by most surface-based organisms. The

technologies described herein have been licensed from Texas A&M University and are being piloted by Cenovus Energy, Inc. with production support from the Southern Alberta Institute of Technology.

I.1 Deciphering the Lotus Leaf and Other Lessons in Fluid Dynamics from Nature

Nature has several examples of intricately structured surfaces designed to mitigate fouling such as leaves of the lotus plant (**Fig. I.3a**),[5–7] the legs of a pond skater (Fig. I.3b),[8] and the skin of a shark.[9,10] In each of these examples, the ability to prevent surface fouling has emerged as a primary adaptation that has allowed the species to thrive in its specific habitat. A lotus leaf can optimize photosynthesis even under low light conditions by ensuring the availability of a large exposed surface area by preventing pond debris from accumulating on its surface.[7,10] A shark maintains hydrodynamic efficiency and thereby its underwater speed advantage by keeping its epidermis free from the buildup of surface detritus, thwarting the best attempts of tenacious maritime fouling organisms; a characteristic that incidentally has been difficult to replicate in ocean-going vessels, which incur tremendous costs in fuel consumption and maintenance as a result of fouling. As indicated by the scanning electron micrographs of natural surface topographies exemplified in Figure I.3, nature often turns to hierarchically textured topographies to obtain non-wettability.[11–13] In other words, nature masterfully exploits the high surface tension of water by intricately texturing solid/air interfaces to control the extent of spread of water droplets on surfaces. Much attention has been devoted to synthetic analogs of surfaces that function in much the same way and actively inhibit or strongly induce spread of water droplets.[9,14,15] The subsequent sections in Chapter I will outline some of the fundamental principles underpinning the design of synthetic surfaces based on combinations of texturation and surface chemistry.

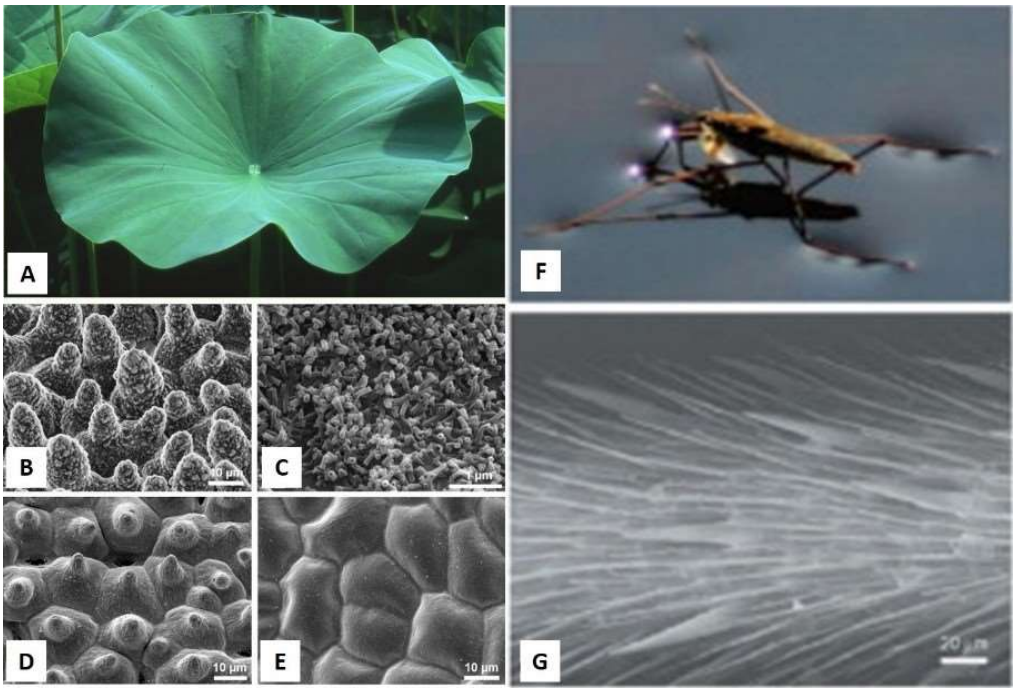

Figure I.3. Examples of micro and nanoscale texturation in nature that give rise to unusual wettability. Scanning electron microscopy (SEM) images showing micro and nano texturation for A-E) a lotus leaf at different magnifications.[16] Adapted with permission from Beilstein-Institut, Hans J. Ensikat, Petra Ditsche-Kuru, Christoph Neinhuis, and Wilhelm Barthlott, *Belstein Journal of Nanotechnology*, 2011, 152-161. Copyright 2011. F) Digital photograph of a pond skater and SEM image of G) pond skater legs.[8] Adapted with permission from Elsevier, Bharat Bhusan and Yong Chae Jung, *Progress in Materials Science*, 2010, 1-108. Copyright 2011.

A major challenge that nature has not had to solve is to render surfaces non-wettable to low-surface tension liquids (such as most liquid hydrocarbons). Nature's inability to handle high concentrations of such liquids, derived almost exclusively from human fossil fuel exploration, is manifest in the devastation wrecked by oil spills on flora and fauna alike. Much of this contribution will focus on emerging ideas and design principles for tackling this more formidable challenge—rendering inorganic surfaces repellant not just towards water but also towards low

surface tension liquids—thereby not just emulating biology but establishing function that surpasses the capabilities of biological architectures.

I.2 The Balance of Forces: Some Physical Principles Underpinning Wettability

When a liquid droplet contacts a solid surface, its (in)ability to wet the surface and the eventual shape of the droplet is determined by the balance between interfacial energies at the solid—vapor, liquid—vapor, and solid—liquid interfaces,[26–28] reflecting the interplay between intermolecular solution forces and interfacial surface energies. As a liquid spreads onto a surface, the solid—vapor interface is replaced by new liquid—vapor and solid—liquid interfaces. The balance of different energetic components is illustrated by considering the wetting of a surface by a single liquid droplet as illustrated in **Figure I.4**. The liquid droplet will stop either when it reaches its universal energetic minimum (equilibrium) or when it becomes pinned in some sort of local minima (a metastable state). The equilibrium contact angle (θ_e), illustrated in Figure I.4, reflects the balance between these interfacial energies and is a directly observable quantity that can be measured and used to understand the balance of surface/interfacial energies. Two distinct parameters strongly affect the balance of energies: (a) the surface tension of the liquid and (b) the chemical compatibility of the surface with the liquid (which is a function of the molecular interactions at the interface). The former is essentially a measure of cohesive forces, typically intermolecular forces, within a liquid, whereas the latter is a measure of adhesive strength between the liquid molecules and the surface. In a qualitative sense, one can immediately appreciate that all other things remaining equal, if there are strong intermolecular interactions within a liquid, it will be more likely to be repelled and remain "beaded up" as compared to a liquid with weaker intermolecular interactions, which will have a tendency to spread on the surface.

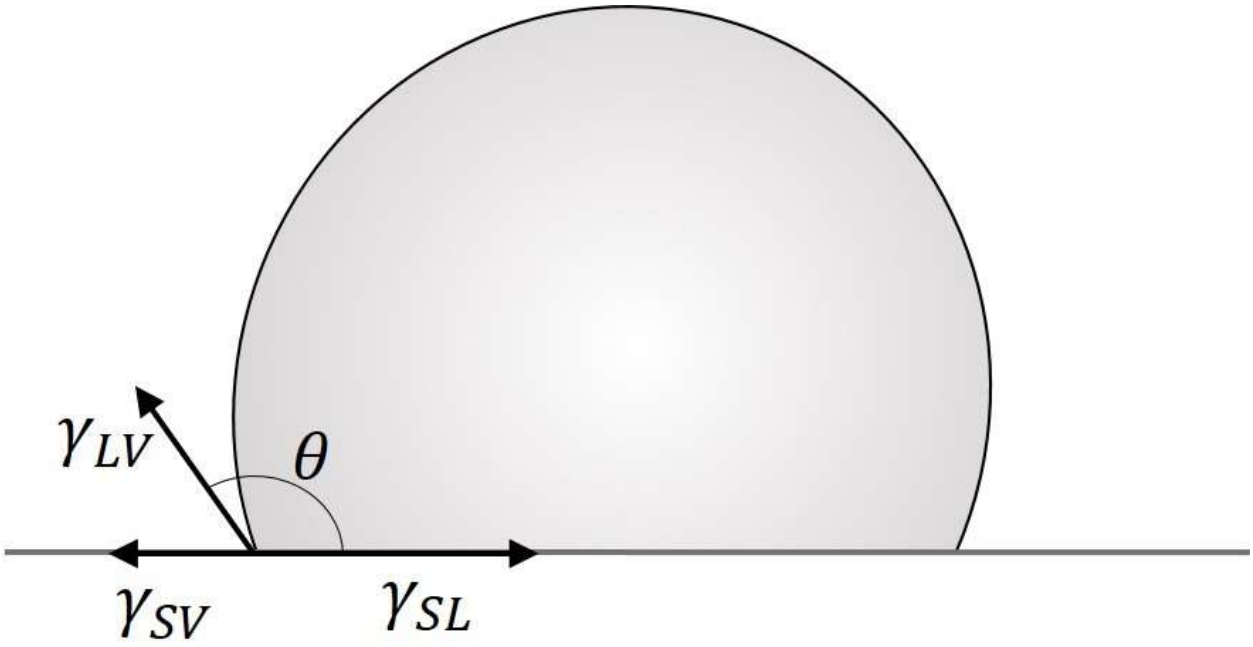

Figure I.4. Contact angle of a liquid droplet illustrating the balance of forces between interfacial energies.

Young developed a formalism relating the spread of a liquid droplet on a (flat) solid substrate (assuming conformal wetting) to the balance of interfacial energies as depicted in Figure I.4. At equilibrium, the drop can spread infinitesimally by an amount ΔA where a solid–liquid interface displaces a solid–vapor interface; the overall change in interfacial energies can be written as:

$$\Delta F = (\gamma_{SV} - \gamma_{SL})\Delta A + \gamma_{LV} cos\theta \Delta A \quad \text{(I.1)}$$

where γ_{SV}, γ_{SL}, and γ_{LV} represent the interfacial energies at solid—vapor, solid—liquid, and liquid—vapor interfaces, respectively.[27] At equilibrium, $\Delta F = 0$ and consequently (1) can be reorganized to yield the equilibrium contact angle (ϑ_e):

$$cos\theta_e = \frac{\gamma_{SV} - \gamma_{SL}}{\gamma_{LV}} \quad \text{(I.2)}^{21,27,29,30}$$

The observed contact angle (which may or may not be ϑ_e depending on whether the system has reached equilibrium) is thus a measure of the wettability of a surface by a liquid. If the water contact angle is <90°, the surface is considered to be wetted by the liquid (and is called hydrophilic or oleophilic for surfaces wetted by water or oil, respectively).[30,31] If the water contact angle is >90°, the surface is considered to (at least partially) repel the liquid. Such surfaces are denoted as being hydrophobic or oleophobic for water or oil, respectively. If the contact angle can be increased above 150°, such a surface is considered superhydrophobic or superoleophobic and will typically strongly repel and even bounce water or oil droplets, respectively. Shark skin and lotus leaves (Figure I.3) are examples of naturally occurring superhydrophobic surfaces.[5–7] However, as briefly noted above, there are no naturally occurring examples of truly oleophobic surfaces.

Let us consider what it takes to make a surface non-wetting towards a liquid. A non-wettable surface implies a high contact angle (typically >150°), which would result in the cosine term being a negative value in the range of -0.5 and -1.0. Based on Equation I.2, this necessitates as a first condition that the interfacial energy at the solid—liquid interface far exceed the interfacial energy of the surface (a solid—vapor term). In other words, a substrate is more likely to repel a liquid droplet if it has a low surface energy (γ_{SV} is low) and if it is chemically incompatible with the liquid droplet under consideration (γ_{SL} is high and positive). The second γ_{SL} term represents interfacial interactions and reflects a balance between disruption of cohesive forces between liquid molecules at the interface, the formation of new interactions between the liquid molecules

and surficial atoms, and the reorganization of surface bonds. A strongly positive value of the latter indicates incompatibility of the liquid and the solid at the interface.

Water and oil wet surfaces very differently. The distinctive behavior of water and oil originates from their vastly different surface tension values. Water has a surface tension of 72.80 x 10^{-3} N/m, whereas as an example of a hydrocarbon, hexadecane has a surface tension of 27.47 x 10^{-3} N/m at 293 K, which reflects the relative magnitudes of their intermolecular interactions;[32] hydrogen bonding in water is much stronger than London dispersion forces typical of hydrocarbons. The latter relatively weak, intermolecular cohesive interactions are much more readily disrupted at surfaces and thus oil droplets tend to more readily spread across surfaces. It is thus much more difficult to make a surface oil repellant (superoleophobic) as compared to making it water repellent (superhydrophobic). For the latter high-surface tension liquid, modifying the surface with a species that does not participate in hydrogen bonding interactions is usually sufficient to render it hydrophobic. The proclivity of oil to wet surfaces needs to specifically be mitigated by modification of the surfaces to expose groups that are incompatible with hydrocarbons (commonly fluorous phases) or by adapting an entirely different tack wherein the droplets are suspended across pockets of air defined by nanoscale topographies (the Cassie—Baxter regime) as discussed below.[33,34]

I.3 Rough at the Edges: Influence of Surface Roughness on Wettability

Apart from the simple balance of interfacial energetics dictated by surface tension and surface energies outlined in Chapter I Section 1.2, surface roughness can also greatly modify the effective interfacial energies by either (i) greatly increasing the effective surface area or (ii) by modifying the proportion of the surface across which the solid and liquid are actually in contact.

The two models used to describe the effects of surface texturation are the Wenzel and the Cassie—Baxter regimes depicted below in **Figure I.5** although realistic samples are often characterized by mixed regimes.[35–37]

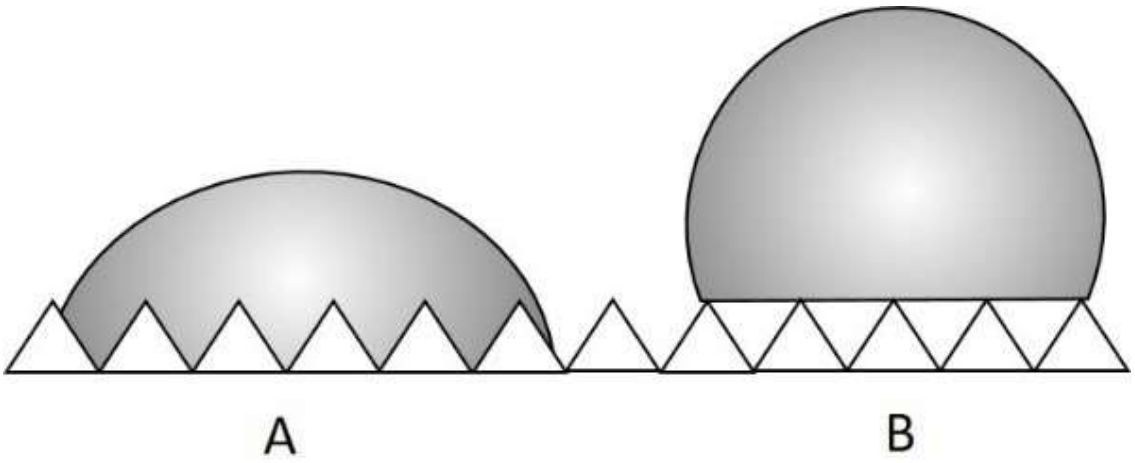

Figure I.5. A) Wenzel regime, representing equilibrium wettability for a rough surface. B) Cassie—Baxter regime representing a metastable suspended state.

The Wenzel regime describes an observed increase in liquid—solid contact area due to the roughening of the surface. In this regime, the liquid droplet still conformally adheres to the contours of the surface but clearly the solid—liquid interactions are greatly enhanced as compared to a smooth surface. The Cassie—Baxter regime describes a situation in which the liquid is in contact with only a small portion of the surface while the other portion sits upon pockets of trapped air (akin to a magician laying down on a "bed of nails").[38] The Cassie—Baxter regime represents a metastable state wherein the liquid droplet is pinned by the features on the surface and thus unable to make contact with the grooves. Such a pinned droplet can

remain suspended in a metastable state unless there is an external force (such as tilting of the substrate) that induces droplet motion.

Surface roughness can alter the formalism written in Equations I.1 and I.2 since the spread of the contact line on a rough surface is best expressed as $r\Delta A$, where r is a factor that reflects the ratio of the actual surface area to the equivalent surface area of a smooth surface. Assuming conformal wetting in the Wenzel regime, Equations I.1 and I.2 are modified by surface roughness to

$$cos\theta w = \frac{r(\gamma_{SV} - \gamma_{SL})}{\gamma_{LV}} = cos\theta_e \qquad \text{(I.3)}^{7,26,27}$$

where θ_W is the observed contact angle, r is a roughness factor that represents the ratio of the actual surface area to the surface area of an equivalent smooth surface, and θ_e is the equilibrium contact angle. Note that this expression is rigorously valid only on a local basis considering three-phase contact lines.[26–28]

This expression introduces us to an observed contact angle that could be different from the equilibrium contact angle. Equation I.3 implies that in the conformal wetting regime, the introduction of roughness or texturation cannot change the sign of the wettability but can amplify the magnitude of the observed $\cos\theta_W$ value. In other words, a surface that is only slightly hydrophobic can be rendered superhydrophobic as a result of surface roughness resulting in water droplets beading up on the surface; conversely, a surface that is oleophilic can be rendered superoleophilic resulting in flash spreading of oil droplets.[31] Such differences are further amenable to modification by surface functionalization (by modulation of the interfacial interactions). Indeed, the self-cleaning effect exhibited by lotus leaves is based on having a

multiscale topography as shown by the scanning electron microscopy images in Figure I.3. Shark skin is also characterized by an intricate pattern of structures spanning multiple length scales.

Additionally, the design of omniphobic surfaces can greatly benefit from architectures that suspend liquid droplets above air pockets according to the Cassie—Baxter formalism.[38] In this regime, the contact angle is modified as follows to an effective contact angle of θ_c:

$$cos\theta_c = f_s(cos\theta_e + 1) - 1 \quad \text{(I.4)}$$

where f_s is the fraction of the solid that touches the liquid and needs to be as small as possible to repel liquid droplets. In this regime, the droplets are suspended between posts protruding from the surface.

Such an architecture is used by numerous insects that have cuticles that can trap air as shown in **Figure I.6**. The trapped air is used by the insect to breathe while it is submerged under water. Figure I.6b illustrates the construction of a "plastron" used by various arthropods as reservoirs of air bubbles. In this contribution, we attempt to replicate similar topographies using tetrapodal ZnO nanostructures. These structures stabilize air pockets analogous to plastrons, enabling them to suspend both water and oil droplets across hierarchically textured substrates. It is with these fundamental principles that are introduced here in Chapter I that we seek to (i) affect the separation of viscous oil and water emulsions with the use of an entirely inorganic membrane system comprised of ZnO nanotetrapods which are embedded onto a stainless steel mesh in order to exploit the orthogonally wettable property of such liquids (described for a model emulsion at room temperature and ambient pressure in Chapter II and for a reconstituted SAGD emulsion at high temperatures and pressures in Chapter III), and (ii) modify the surface properties by inducing micro- and nanoscale texturation and chemically functionalizing such surfaces to

completely prevent wetting by oil and water. The development of such biomimetic (plastron-like) surfaces for the complete repellence of liquids by using a combination of base metals texturized *via* acid etching, spray coating with ZnO nanotetrapods, and further chemical treatments is discussed in more detail in Chapter IV. In Chapter V, these fundamental lessons in forming non-wettable surfaces *via* tuning the surface energy with selected compounds are combined with information from hydrophobic materials developed in Chapters II and III by the arrangement of ZnO nanotetrapods coated onto stainless steel meshes with additional chemical funtionalization. Additionally, Chapter VI explores an alternative metal oxide templating technique is explored with the use of commercially available TiO_2 nanoparticles patterned into an inverse opal structure using a sacrificial polystyrene templating technique, where the remaining TiO_2 is functionalized and rendered omniphobic. Chapter VI also discusses the potential application of both TiO_2 nanoparticles and ZnO nanotetrapods as coatings for oil pipelines to address the challenging rheological characteristics of heavy oil.

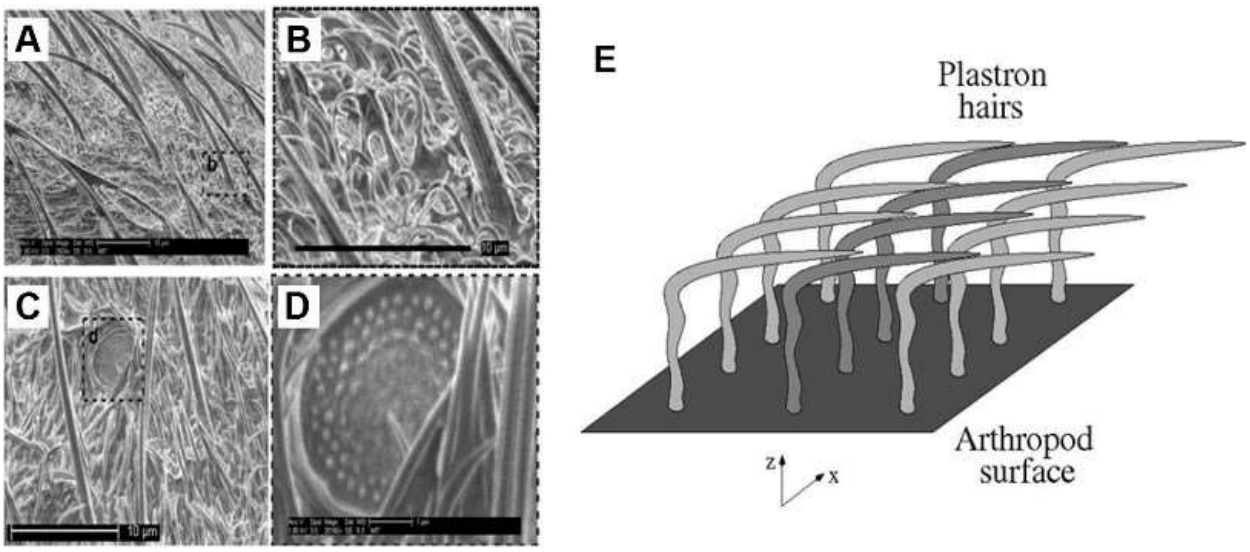

Figure I.6. SEM images of the integument of a water-walking insect called *Mesovelia* (A-D). The image depicts intermittent and waxy hairs that trap a plastron air bubble. The air trapped in the bubble allows the insect to breathe while underwater. E) Schematic of a plastron geometry designed to trap air.[39] Adapted with permission from Cambridge University Press, Flynn, M. R.; and Bush, J. W. M. *The Journal of Fluid Mechanics*, 2008, 275-296. Copyright 2008.

I.4 The Design of Orthogonally Wettable Surfaces

In order to devise surfaces for use as orthogonally wettable membranes that will selectively wet one liquid while repelling another, the fundamental principles of wettability, which have been outlined in Sections I.1—I.3, must be carefully considered and deployed. In the case of membranes, the differences in the surface tension of oil and water can be exploited to ensure the permeation of one phase and the rejection of the other. It is worth noting that the surface tension, and thus the tendency of the liquid to spread across the surface or remain beaded up, cannot be changed as it is a property inherent to the individual liquid. In contrast, how these liquids interact with surfaces can be drastically changed by the texturation (roughening) as well as the surface energy of the surfaces. Towards this end, multiscale texturation from a combination of stainless

steel meshes (which provides microscale texturation) and ZnO nanotetrapods (which provides nanoscale texturation) are used to enhance the inherent wettability of oil and water. Owing to its lower surface tension, oil will have a tendency to spread across a surface, and in the case of a membrane, such increased wettability will ensure its ability to permeate. In contrast, the greater surface tension of water increases its ability to form droplets and prevent permeation. This difference in behavior is intensified with increased roughness. As equation I.3 indicates, a rougher surface will increase the inherent wettability of a liquid in contact with a solid. To this end, increasing the roughness using mesoscale texturation aids in both the permeation of oil as well as the rejection of water, creating an orthogonally wettable surface. With this differential wetting model, oil can be permeated and essentially "dried" of water for use as a purification step before further processing, and water can be separated and removed without containing oil essentially cleaning the water for reuse in the SAGD process. This is especially important with SAGD extracted emulsions, such as shown in **Figure I.7** Here, the complex hierarchical nature of the emulsions including the inclusion of multiscale water droplets is noted.

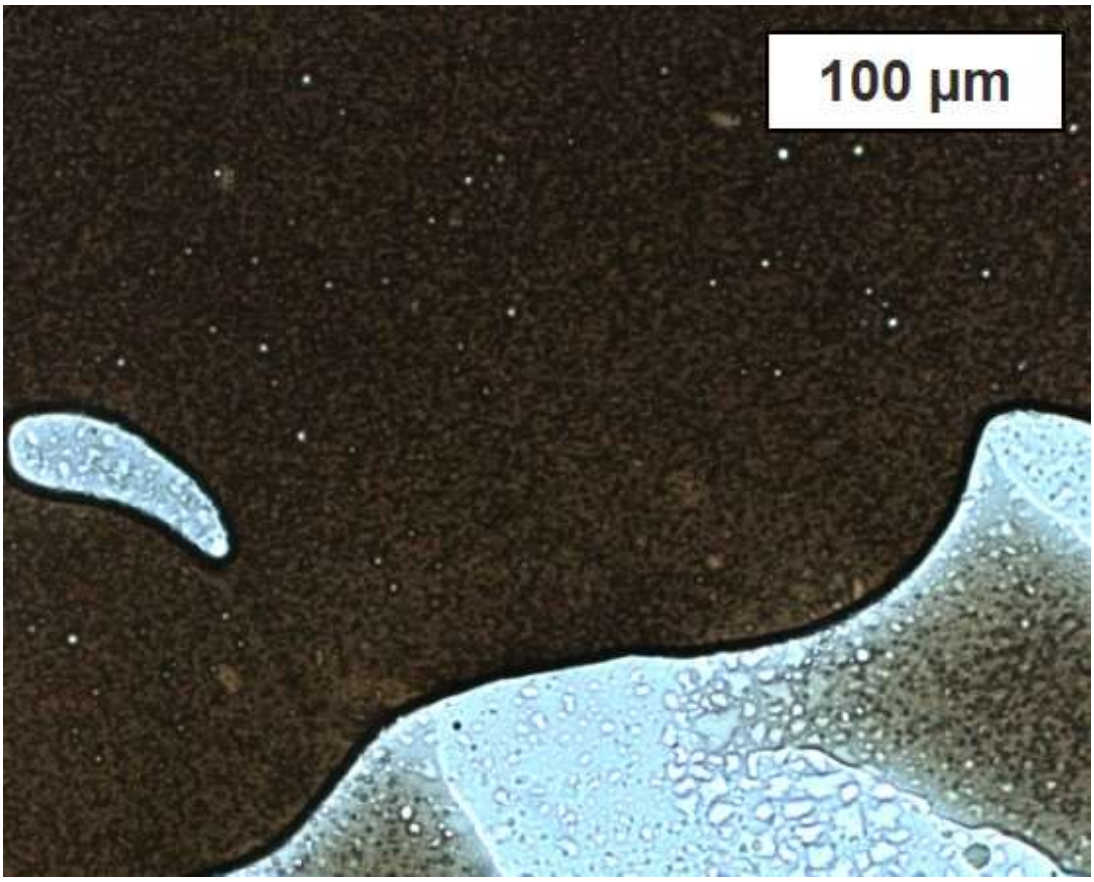

Figure I.7. Optical microscopy image of a SAGD emulsion with a water content of ca. 30 vol.%. The lighter regions correspond to water droplets and darker solid particles are asphaltene residues and silt particles.

While other methods and membranes also seek to realize the separation of viscous oil and water, many of them rely on polymeric materials for de-emulsification.[32,33] The extreme heat and pressure characteristics of the SAGD method severely constrain or entirely preclude the use of such materials as they can be susceptible to failure and fouling. Furthermore, traditional filtration methods, which use pore size to control the retention or exclusion of droplets, are unable to affect the separation of complex hierarchical emulsions commonly observed in complex viscous oil and water emulsions (Figure I.7).[34] This is especially true of SAGD emulsions since at high

pressures, the droplets in such emulsions can distort and pass through the membranes, diminishing their effectiveness.[35] Towards this end, the use of inorganic membrane systems can provide a mechanically resilient and thermally robust platform that allows for the separation of liquids based on their differentially wettability, thereby mitigating some of the challenges faced by conventional polymeric filtration systems.

In this dissertation, model emulsions of hexadecane and water are separated using inorganic membranes comprising ZnO nanotetrapods that are embedded into stainless steel meshes as described in Chapter II. An analytical expression is developed that relates separation efficiency to length of the interfacial area. Additionally, this separation modality is further explored in Chapter III with a parametric study of ZnO nanotetrapod loading, pore size, and temperature, performed using a custom-designed hydrothermal system that emulates the high-pressure and high-temperature conditions typical of SAGD extraction, while using realistic reconstituted viscous oil and water emulsions. The second half of the dissertation focuses on experimental realization of ideas of incommensurate wettability to design surfaces that are resistant to wetting by both water and oil.

I.5 Man versus Rust: In Search of Universal Non-Wettability

Base metals, particularly low alloys of steel underpin the structural infrastructure on which much of modern civilization is founded; e.g., bridges, skyscrapers, railroads, and shipping vessels. Despite their ubiquity, structural materials are inevitably plagued by corrosion and degradation originating from the preferential thermodynamic stability of iron oxide over metallic iron at atmospheric temperature and pressure (**Error! Reference source not found.**). The history of human civilization has reflected the constant trade-offs between the functionality of structural

metals and their inevitable degradation over time. Definitions of wealth have thus long centered on the acquisition of noble metals that are not as easily degraded by time.[17,18] However, noble metals are not in adequate abundance in the crust of the earth to meet infrastructure needs (nor do they have the necessary load-bearing properties). High-alloy steels remain cost prohibitive and their application is confined to niche automotive, domestic, defense, and aerospace applications. Considerable progress continues to be made on alloy development but modern light-metal alloys are plagued by their own set of corrosion issues arising from the presence of surface precipitates. Industrial practice is thus still strongly focused on protection of base metals by impeding corrosion reactions.[17,18]

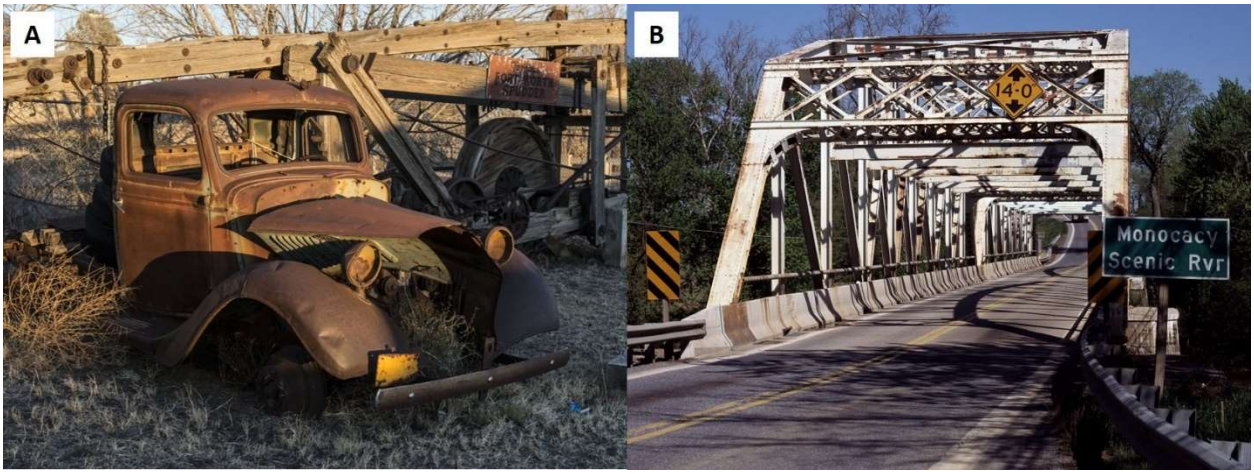

Figure I.8. Classical photographs from the United States Library of Congress depicting rust degradation (A) of a vehicle and (B) a bridge in the United States. Reproduced from The Library of Congress, Carol M. Highsmith archive.

Modern coating systems typically incorporate several different modes of active and passive corrosion protection systems.[17] Barrier protection plays a critical role in inhibiting corrosion

processes since corrosion cannot be initiated if corrodant species cannot be transported to reactive interfaces. A major imperative for designing liquid repellent surfaces is that they can oftentimes be used to protect the underlying metal, thereby greatly expanding the time over which such a component can be used industrially. While corrosion in aqueous media, particularly high salt water content media where ion transport is facile, represents the bulk of corrosion problems, repelling low-surface tension liquids has emerged as an urgent imperative for the vast fossil-fuel-based energy infrastructure. Hydrocarbons form emulsions with water droplets and such mixtures wet surfaces in a complex manner, oftentimes facilitating the transport of corrodant species and accelerating corrosion. Hydrocarbons further dissolve extremely corrosive CO_2 and H_2S species that yield distinctive modes of scale formation and failure. The fouling of oil handling equipment and pipelines represents a tremendous burden on the energy infrastructure and increases risks of environmental contamination from spills.[19,20] The cleaning and repair of components used for the storage, transport, and processing of oil carry a heavy price tag and repair activities are often undertaken at substantial risk to human health and safety. Consequently, there is great interest in the development of omniphobic surfaces that are wetted neither by water nor by oil.[21–25] Illustrating the design of such surfaces on low-alloy steel substrates will be the primary focus of this contribution. Omniphobic surfaces are expected to have non-fouling and self-cleaning characteristics, enabling residual liquids and solid debris to be washed away with minimal human intervention.

Such a topography, upon reduction of surface energy as a result of functionalization with perfluorinated monolayers, allows for suspension not just of water droplets but also droplets of oil. A combination of microscale texturation defined by selective etching, nanoscale texturation defined by integration of nanoscale oxide elements, and chemical modification defined by a

perfluorinated molecular monolayer renders a low alloy steel non-wetting towards heavy oils. To our knowledge, this reflects the first demonstration of non-wettability of a surface towards a realistic heavy hydrocarbon fuel.

I.6 Texturation and Surface Chemistry: Mimicking Biological Surfaces to Obtain Universal Non-Wettability

As discussed in the preceding sections, the behavior of a liquid droplet upon being placed on a substrate is predicated on the surface tension of the liquid (as determined by the cohesive forces between the liquid molecules), the microscale and nanoscale texturation of the surface (which can amplify intrinsic wettability or provide reentrant curvature to surfaces), as well as the specific surface energy at the liquid/solid interface.[21,27,29,30] Consequently, attempts to rationally design omniphobic surfaces have sought to examine the most optimal texturation and surface chemistries necessary to endow universal non-wettability.[21–25,40,41]

While bioinspired successes that deliver universal non-wettability have been realized through various approaches, current solutions do not meet the needs of the energy infrastructure where extreme temperature, pressure, stress, and flow variations as well as highly corrosive environments (with high CO_2 and H_2S concentrations) are typical.[19,20,42,43] Without attempting to be exhaustive, we overview a cross-section of approaches that have thus far been used to prepare omniphobic surfaces. While much mechanistic understanding has derived from studies of lithographically patterned substrates with variably spaced pillars, such substrates are complex to fabricate and are not viable at any realistic scales.[21,33] As an alternative, polymer derived architectures wherein microscale topography is defined by electrospinning or through the use of woven fabric substrates or electrospun fibrous mats are much more readily and inexpensively

prepared but are unable to withstand high temperature and stress gradients[24,33,44] and are further mechanically pliant and thus cannot be deployed in applications requiring high fluid flow (and are thus unviable for applications such as tanker trucks, railcars, and pipe interiors). As a few notable examples of this latter approach, McCarthy *et al*. have altered the topography of woven polyester fabrics to modulate their wettability.[45] The substrate fibers from the fabric provide microscale roughness and are further modified *via* a facile silicone grafting procedure to tune the surface energy and endow hydrophobic characteristics.[46] Similarly, Liu *et al*. have roughened cotton fabrics through a multistep chemical treatment protocol to define microscale texturation and then proceeded to embed poly(butylacrylate)-modified carbon nanotubes within the fabrics to provide nanoscale roughness and lower the surface energy.[47]

Alternative approaches to the use of woven fibers or etching of metals that have emerged in recent years include the layer-by-layer deposition of polymeric and nanocrystalline layers and the stabilization of complexes of polyelectrolytes and fluorosurfactants. For instance, Bhushan and co-workers have reported a polyelectrolyte assembly incorporating SiO_2 nanocrystals with oriented fluorosurfactants as the top layers.[22] These films demonstrate oleophobic but hydrophilic behavior with good resistance to wear and particulate contamination. However, the use of polyelectrolytes gives rise to similar thermal degradation issues as noted above for woven polymer substrates. Furthermore, adhesion of polyelectrolytes to steel represents a substantial challenge under operating conditions.

For viable largescale applications, the coated surfaces need to be mechanically robust, formable, and weldable. Such a consideration brings to the fore metallic substrates. Microscale and even nanoscale texturation can be defined directly onto metallic substrates by selective etching. The fundamental basis for this approach is the accumulation of dislocations at the surfaces of

structural metals, which enable differential pitting corrosion wherein a corrosion cell is established across intact and highly strained regions of the metal surface.[48–50] As an example of this approach, multiscale texturation has been defined within Al substrates by dual etching, first using HCl to define microscale texturation and then a mix of HNO_3 and $Cu(NO_3)_2$ to define nanoscale topographies. The substrate is then functionalized with a perfluorinated siloxane to obtain a mechanically stable omniphobic surface.[40]

This dissertation is structured across six chapters. In Chapter I we introduce challenges associated with the construction of differentially wettable as well as omniphobic surfaces. We further outline the motivation for developing a toolkit to handle complex rheological fluids to facilitate extraction, handling, and processing of viscous oil. The development of differentially wettable surfaces is first explored using a model hexadecane and water emulsion in Chapter II. Next, the task of separating real-world emulsions under realistic temperature and pressure conditions is confronted in Chapter III.

In Chapter IV we will explore the texturation of A36 steel substrates with the texturation induced with acid etching and subsequent deposition of ZnO nanotetrapods. These surfaces are further evaluated as a function of additional functionalization in order to tune the extent of (non)-wettability of water and oil. Next, Chapter V demonstrates a combination of texturization of stainless steel meshes and ZnO tetrapods (similar to the membranes of Chapters II and III), with the additional use of the downselected chemical treatments developed in Chapter IV. This chapter outlines general design principles extrapolating from natural examples, and illustrates the successful design of a “plastron” architecture that traps air in a manner reminiscent of a cuticle coated with hairs that serves as a respiratory reservoir for aquatic insects. Alternative approaches to generate surfaces not wetted be either oil or water include texturation of flat steel substrates

utilizing colloidal crystal templating of TiO_2 nanoparticles.[55,56] This is performed by combining the TiO_2 nanoparticles with polystyrene spheres that act as a sacrificial template, as further discussed in Chapter VI. This process is designed to be a viable method for real-world applications as it circumvents the need for additional etching or patterning steps, but rather only requires application *via* a simple spray coating procedure. The patterned TiO_2 nanoparticles are further functionalized with perfluorinated phosphonic acid to reduce the surface energy, thereby yielding surfaces that demonstrate the efficacious gliding of both water and viscous oil.

I.7 References

(1) U.S. Energy Information Administration. International Energy Statistics http://www.eia.gov/cfapps/ipdbproject/iedindex3.cfm?tid=90&pid=44&aid=8 (accessed Jan 8, 2018)

(2) Dusseault, M. B.; ShafieiI, A. In *Ullmann's Encylopedia of Industrial Chemistry*; 2011; Vol. 25, pp 263–314.

(3) Guo, K.; Li, H.; Yu, Z. *Fuel* **2016**, *185*, 886–902.

(4) Staff, J. Temporarily shutting in oilsands SAGD wells might not be as harmful as you think http://www.jwnenergy.com/article/2016/5/temporarily-shutting-oilsands-sagd-wells-might-not-be-harmful-you-think/ (accessed Dec 30, 2017)

(5) Cheng, Y. T.; Rodak, D. E. *Appl. Phys. Lett.* **2005**, *86* (14), 1–3.

(6) Barthlott, W.; Neinhuis, C. *Planta* **1997**, *202* (1), 1–8.

(7) Feng, L.; Li, S.; Li, Y.; Li, H.; Zhang, L.; Zhai, J.; Song, Y.; Liu, B.; Jiang, L.; Zhu, D. *Adv. Mater.* **2002**, *14* (24), 1857–1860.

(8) Bhushan, B.; Jung, Y. C. *Prog. Mater. Sci.* **2011**, *56* (1), 1–108.

(9) Bixler, G. D.; Bhushan, B. *J. Colloid Interface Sci.* **2013**, *393* (1), 384–396.

(10) Kirschner, C. M.; Brennan, A. B. *Annu. Rev. Mater. Res.* **2012**, *42* (1), 211–229.

(11) Ball, P. *Nat. Eng.* **1999**, *400* (6744), 507–508.

(12) Carman, M. L.; Estes, T. G.; Feinberg, A. W.; Schumacher, J. F.; Wilkerson, W.; Wilson, L. H.; Callow, M. E.; Callow, J. A.; Brennan, A. B. *Biofouling* **2006**, *22* (1–2), 11–21.

(13) Bixler, G. D.; Bhushan, B. *Soft Matter* **2012**, *8* (44), 11271.

(14) Sun, M.; Luo, C.; Xu, L.; Ji, H.; Ouyang, Q.; Yu, D.; Chen, Y. *Langmuir* **2005**, *21* (19), 8978–8981.

(15) Magin, C. M.; Cooper, S. P.; Brennan, A. B. *Mater. Today* **2010**, *13* (4), 36–44.

(16) Ensikat, H. J.; Ditsche-Kuru, P.; Neinhuis, C.; Barthlott, W. *Beilstein J. Nanotechnol.* **2011**, *2* (1), 152–161.

(17) Quéré, D. *Annu. Rev. Mater. Res.* **2008**, *38* (1), 71–99.

(18) Shirtcliffe, N. J.; McHale, G.; Atherton, S.; Newton, M. I. *Adv. Colloid Interface Sci.* **2010**, *161* (1–2), 124–138.

(19) Feng, X.; Jiang, L. *Adv. Mater.* **2006**, *18* (23), 3063–3078.

(20) Tuteja, A.; Choi, W.; Ma, M.; Mabry, J. M.; Mazzella, S. a; Rutledge, G. C.; McKinley, G. H.; Cohen, R. E. *Science* **2007**, *318* (5856), 1618–1622.

(21) Quéré, D. *Reports Prog. Phys.* **2005**, *68* (11), 2495–2532.

(22) Roach, P.; Shirtcliffe, N. J.; Newton, M. I. *Soft Matter* **2008**, *4* (2), 224.

(23) Velázquez, J. M.; Gaikwad, A. V.; Rout, T. K.; Baier, R. E.; Furlani, E. S.; Banerjee, S. *J. Mater. Chem.* **2012**, *22* (8), 3335.

(24) *CRC Handbook of Chemistry and Physics*, 97th ed.; Haynes, W. M., Bruno, T. J., Lide, D. R., Eds.; CRC Press: Boca Raton, 2016.

(25) Tuteja, A.; Choi, W.; Mabry, J. M.; McKinley, G. H.; Cohen, R. E. *Proc. Natl. Acad. Sci.* **2008**, *105*, 18200–18205.

(26) Tuteja, A.; Choi, W.; McKinley, G. H.; Cohen, R. E.; Rubner, M. F. *MRS Bull.* **2008**, *33* (8), 752–758.

(27) Whyman, G.; Bormashenko, E.; Stein, T. *Chem. Phys. Lett.* **2008**, *450* (4–6), 355–359.

(28) Giacomello, A.; Meloni, S.; Chinappi, M.; Casciola, C. M. *Langmuir* **2012**, *28* (29), 10764–10772.

(29) Yildirim Erbil, H.; Elif Cansoy, C. *Langmuir* **2009**, *25* (24), 14135–14145.

(30) Cassie, A. B. D.; Baxter, S. *Trans. Faraday Soc.* **1944**, *40* (5), 546–551.

(31) Flynn, M. R.; Bush, J. W. M. *J. Fluid Mech.* **2008**, *608* (Wenzel 1936), 275–296.

(32) Brown, P. S.; Atkinson, O. D. L. a; Badyal, J. P. S. *Appl. Mater. Interfaces* **2014**.

(33) Takht Ravanchi, M.; Kaghazchi, T.; Kargari, A. *Desalination* **2009**, *235* (1–3), 199–244.

(34) Zhu, Y.; Wang, D.; Jiang, L.; Jin, J. *NPG Asia Mater.* **2014**, *6* (5), e101.

(35) Cobos, S.; Carvalho, M. S.; Alvarado, V. *Int. J. Multiph. Flow* **2009**, *35* (6), 507–515.

(36) Dennis, R. V; Patil, V.; Andrews, J. L.; Aldinger, J. P.; Yadav, G. D.; Banerjee, S. *Mater. Res. Express* **2015**, *2* (3), 32001.

(37) Dennis, R. V.; Fleer, N. A.; Davidson, R. D.; Banerjee, S. In *Graphene Technology: From Laboratory to Fabrication*; Nazarpour, S., Waite, S. R., Eds.; Wiley-VCH Verlag GmbH & Co. KGaA.: Berlin, 2016; pp 155–176.

(38) Cheng, Y. F. *Corros. Eng. Sci. Technol.* **2015**, *50* (3), 161–162.

(39) Crosby, T.; Wolodko, J.; Tsaprailis, H. In *Gap Analysis of Canadian Pipeline Coatings: A Review Study*; 2016; pp 1–12.

(40) Brown, P. S.; Bhushan, B. *J. Colloid Interface Sci.* **2015**, *456*, 210–218.

(41) Tsujii, K.; Yamamoto, T.; Onda, T.; Shibuichi, S. *Angew. Chemie Int. Ed. English* **1997**, *36*, 1011–1012.

(42) Choi, W.; Tuteja, A.; Chhatre, S.; Mabry, J. M.; Cohen, R. E.; McKinley, G. H. *Adv. Mater.* **2009**, *21* (21), 2190–2195.

(43) Pan, S.; Kota, A. K.; Mabry, J. M.; Tuteja, A. *J. Am. Chem. Soc.* **2013**, *135*, 578–581.

(44) Peng, S.; Bhushan, B. *J. Colloid Interface Sci.* **2016**, *461*, 273–284.

(45) Yang, J.; Zhang, Z.; Men, X.; Xu, X.; Zhu, X. *New J. Chem.* **2011**, *35*, 576–580.

(46) Fang, B. Y.; Atrens, A.; Wang, J. Q.; Han, E. H.; Zhu, Z. Y.; Ke, W. *J. Mater. Sci.* **2003**, *38* (1), 127–132.

(47) Kermani, M. B.; Morshed, A. *Corrosion* **2003**, *59* (8), 659–683.

(48) Chhatre, S. S.; Tuteja, A.; Choi, W.; Revaux, A.; Smith, D.; Mabry, J. M.; McKinley, G.

H.; Cohen, R. E. *Langmuir* **2009**, *25* (23), 13625–13632.

(49) Lee, J. A.; McCarthy, T. J. *Macromolecules* **2007**, *40* (11), 3965–3969.

(50) Gao, L.; McCarthy, T. J. *Langmuir* **2006**, *22* (14), 5998–6000.

(51) Liu, Y. Y.; Wang, R. H.; Lu, H. F.; Li, L.; Kong, Y. Y.; Qi, K. H.; Xin, J. H. *J. Mater. Chem.* **2007**, *17* (11), 1071–1078.

(52) Qian, B. T.; Shen, Z. Q. *Langmuir* **2005**, *21* (20), 9007–9009.

(53) Vander Voort, G. F. *Metallogr. Princ. Pract.* **1984**, 59.

(54) Young, F. W. *J. Appl. Phys.* **1961**, *32* (2), 192–201.

(55) Stein, A.; Wilson, B. E.; Rudisill, S. G. *Chem. Soc. Rev.* **2013**, *42* (7), 2763–2803.

(56) Iskandar, F.; Nandiyanto, A. B. D.; Yun, K. M.; Hogan, C. J.; Okuyama, K.; Biswas, P. *Adv. Mater.* **2007**, *19* (10), 1408–1412.

CHAPTER II

ORTHOGONAL WETTABILITY OF HIERARCHICALLY TEXTURED METAL MESHES AS A MEANS OF SEPARATING WATER/OIL EMULSIONS*

II.1 Outline

The removal of submicrometer-sized oil droplets from water remains a key challenge in achieving the separation of emulsions and has emerged as an urgent imperative given the increasing use of unconventional extractive processes such as steam-assisted gravity drainage. In Chapter II, we demonstrate that a substrate with hierarchical texturation shows pronounced differences in the wettability of water and hexadecane, thereby facilitating the separation of these two disparate liquids at room temperature and pressure. The multiscale textured substrates are assembled using a facile and readily scalable process wherein ZnO nanotetrapods prepared by high-temperature treatment of zinc metal are spray-deposited onto a stainless steel mesh with micron-sized features. Separation efficiencies well over 99% are routinely accessible at room temperature and pressure by simply flowing emulsions across these hierarchically textured surfaces. A plot of the separation efficiency as a function of effective path length shows a Boltzmann dependence that can be rationalized as a two-state probabilistic function for oil droplets within the emulsion encountering the hierarchically textured surface. The separation efficiency can further be tuned by altering the solid—liquid interfacial energy by surface functionalization with silane monolayers.

---

* Reproduced with permission from "Orthogonal Wettability of Hierarchically Textured Metal Meshes as a Means of Separating Water/Oil Emulsions." O'Loughlin, T.E.; Martens, S; Ren, S.R.; McKay, P.; and Banerjee, S. *Advanced Engineering Materials,* **2017**, *19* (5), 1600808. Reproduced by permission of John Wiley & Sons, Inc.

II.2 Introduction

Despite the recent emergence and increasing practical feasibility of renewables, the overwhelming reliance of modern economies on conventional sources of energy cannot be understated. Meeting the global demand for fossil fuels requires novel drilling methods and accessing unconventional geological deposits. The high-pressure and high-temperature injection of steam is often used to loosen and extract sub-surface bituminous residues using methods such as steam-assisted gravity drainage. [1,2] As noted in Chapter 1, the extracted fluids are emulsions of hydrocarbons and water that at various stages of processing can be termed water-in-oil or oil-in-water emulsions. Bringing about the efficacious separation of the water and oil components of the emulsions, particularly the separation of emulsified oil, is imperative both for increasing the efficiency of the extractive processes as well as to meet regulatory requirements for the treatment of wastewater. [3] Achieving the separation of emulsions is further critical for addressing oil spills within marine environments. [4] Given increasing industrial emphasis on tapping unconventional deposits and an increasingly stringent regulatory environment, much recent attention has focused on the development of membranes and de-emulsification methods for realizing water/oil separation based on differential affinity, density, flow characteristics, and wettability. [4–11] However, many such methods make use of polymeric systems that have limited viability at the high temperatures and pressures typical of most extractive processes and further tend to be susceptible to degradation and fouling. In Chapter II, we demonstrate an entirely inorganic system for separating the water and oil components of emulsions based on the differential wettability of the two liquids on a hierarchically textured metal mesh surface prepared by integrating nanostructured ZnO tetrapods onto microstructured stainless steel meshes. We further develop this design in Chapter III with the use of real SAGD emulsions.

Conventional filtration systems struggle to separate realistic emulsions that contain a variety of different droplet sizes of one phase dispersed within the second phase. Such systems are typically engineered to separate oil and water droplets based on droplet size differentials. However, this imposes the requirement that the pore size of the membrane has to be smaller than the smallest droplet size contained within the emulsion and is particularly a challenge for submicron size droplets of emulsified oil. At high-pressures, the droplets can be deformed and can break through the membrane substantially degrading the separation efficiency. [7,9,10,12] Membranes with submicron-sized dimensions are often used to mitigate this problem but require unrealistically high-pressure gradients and yield extremely low liquid fluxes. [9]

The high surface area of nanotextured surfaces results in the manifestation of remarkable new wettability phenomena that can be deployed to obtain the separation of dissimilar liquids. [9,13–17] In particular, nanotexturation can greatly amplify the intrinsic wettability of a surface both in the conformally wetted Wenzel and suspended Cassie—Baxter regimes. [14–17] The effect of nanotexturation on the wettability of different liquids can be quite dissimilar depending on the intrinsic wettability of the surface by the liquid, which in turn depends on the solid—liquid interfacial energy and thus the specific modes of intermolecular interaction. Consequently, intrinsic differences in wettability can be greatly amplified by hierarchical texturation. In this work, we demonstrate the separation of a water/hexadecane model emulsion based on such orthogonal wettability. The vastly different surface tensions of the two liquids (at a temperature of 293K, water has a surface tension of 72.80 x 10^{-3} N/m, whereas hexadecane has a surface tension of 27.47 × 10^{-3} N/m) [18] and their contrasting modes of interaction with nanostructured ZnO facilitate their effective separation using a modified metal mesh membrane. Remarkably, the emulsions are efficaciously separated at room temperature and pressure based on wettability

differences alone by dint of the hierarchical multiscale texturation that arises from the combination of ZnO nanotetrapods and microscale features of the underlying meshes without any need for lithographically defining specific morphologies. The use of earth-abundant low-cost frameworks that are readily scalable (units of up to 5″ × 5″ have been developed in our laboratories) suggests the potential of these systems as viable membranes for the large-scale separation of emulsions.

II.3 Experimental Details

II.3.1 Materials

A facile and scalable method for rapidly generating ZnO tetrapods was developed based on the rapid air oxidation of Zn foils. [19] Specifically, Zn metal sheets (99% purity on metals basis, McMaster-Carr) were cut into smaller substrates that were ca. 3 mm × 3 mm in size. The Zn substrates then placed onto a stainless steel mesh and placed within a 1″ diameter quartz tube, which in turn was placed within a tube furnace (Lindburg/BlueM). [20] The substrates were heated at a rate of 43°C/min with the ends of the tube furnace open to achieve a maximum temperature of 950°C. The samples were recovered after heating for 1 min at this temperature. The resulting highly crystalline nanostructures were collected and dispersed in 2-propanol (99.9%, Fisher Scientific) to obtain dispersions with a concentration of 20 mg/μL. Next, the dispersion was spray coated onto 316 stainless steel mesh with a pore size of ca. 84 μm (McMaster-Carr) using a Master airbrush with a nozzle diameter of 0.5 mm with the help of an air compressor at an output pressure of 45 psi. The final coated meshes had a ZnO loading of ca. 3.5 mg/cm^2. For all of the coating processes, the substrates were placed on a heating plate with a surface temperature of ca. 120°C.

The mechanical resilience of the ZnO nanotetrapod coatings under mechanical friction or fluid flow is a critical imperative. An amorphous SiO_2 layer has been constituted at the interface between the ZnO nanotetrapods and the native oxide of the metal meshes by utilizing a modified Stöber method. Tetraethylorthosilicate (TEOS) is used as the precursor in this process and is applied from a solution containing 80 vol.% ethanol, 18.5 vol.% deionized water (ρ = 18.2 MΩ/cm), 1 vol.% of 30% aqueous solution of NH_4OH, and 0.5 vol.% TEOS (99.999+% metals basis, Alfa Aesar). The TEOS layer is sprayed while holding the samples at a temperature of 120°C in order to help facilitate the formation of the siloxane bonds to the hydroxyl groups at ZnO surfaces as well as the surfaces of the native oxides of the metal mesh. An applied volume of 3.9 μL/cm^2 was found to be optimal to facilitate adhesion.

To alter the wettability of the ZnO-tetrapod-coated meshes, their surfaces were functionalized by tethering silanes to constitute monolayers with pendant fluorinated or hydrocarbon chains. Briefly, stock solutions of 2 vol.% of the desired silane were prepared by combining 400 μL of deionized water (ρ = 18.2 MΩ/cm), 400 μL of 28—30% ammonium hydroxide, and 400 μL of the appropriate silane, then diluting to 20 mL using *n*-butanol. The silanes, heptadecafluoro-1,1,2,2-tetrahydrodecyl)trimethoxysilane and *n*-octadecyltrichlorosilane, were purchased from Gelest Inc. The substrates were immersed in the butanol solutions for 1 h, washed with copious amounts of *n*-butanol to remove physisorbed silanes, and then allowed to dry before testing.

II.3.2 Characterization

The morphology of the ZnO tetrapods was evaluated using a JEOL JSM-7500F field emission scanning electron microscope (FE-SEM) equipped with a high brightness conical FE gun and a low aberration conical objective lens. An accelerating voltage of 2—5 kV was used to image the

nanostructures. Phase identification was performed by powder X-ray diffraction (XRD) using a Bruker-AXS D8 Vario X-ray powder diffractometer with Cu-Kα radiation (λ = 1.5418 Å). Raman measurements were acquired with 514.5 nm laser excitation from an Ar-ion laser using a Jobin-Yvon Horiba Labram HR instrument coupled with an Olympus microscope. All contact angles (advancing and receding) were measured using a CAM 200 Optical Goniometer. For all experiments, a drop size of 10 μL was used to apply the test liquids. A mechanical pipette was used to apply doubly distilled and deionized water; a manual micropipette was used to apply hexadecane. All contact angles in this work are a result of at least three averaged values. To evaluate the adhesion of the coatings with and without TEOS, American Society for Testing of Materials (ASTM) tests D3359 and D2197 were implemented on ZnO nanotetrapods embedded onto A36 low carbon steel. In ASTM D3359, a grid was scribed onto the coated substrate and tape from the ASTM kit was applied and subsequently removed. The area under evaluation was then examined for the removal of coating material from the surface and classified from 0B to 5B as prescribed by the ASTM method. In ASTM D2197, a standardized stainless steel u-shaped hook was lowered onto the surface of the A36 low carbon steel surfaces and then the substrate was dragged while the u-shaped hook scraped across the substrate. The hook then had additional weight added to it and was scraped along a new pristine portion of the substrate until the force on the u-shaped hook was great enough to scrape though the coating and expose bare A36 steel. This value was recorded and noted as the failure point of the coating. If no additional weight was needed to penetrate the coating, the failure point was noted as zero grams.

II.3.3 Separations

The emulsions were generated by combining 15 mL of hexadecane (99%, Sigma-Aldrich) and 15 mL of deionized water and shaking vigorously until the two phases were completely mixed. Blue

food dye was added to the water for clarity (propylene glycol, FD&C blue1 and red 40, propylparaben, McCormick).

The experimental apparatus for the separation of water/hexadecane emulsions was custom designed and is discussed in further detail below. The fabricated design consists of a mount to attach the stainless steel mesh, and two separate containers to collect both the roll-off fraction as well as the liquid permeating through the mesh. All oil and water volumes were measured with a graduated cylinder. Multiple sample replicates (at least triplicates in each case) were performed and the reported values indicate the standard deviations for each effective length. Over 100 membranes have been used to separate water and oil components of emulsions.

II.4. Results and Discussion

A fundamental challenge associated with the separation of emulsions includes the presence of submicron-sized droplets that can be difficult to separate based on density differentials or size exclusion. Differential wettability poses an attractive alternative for separating the component of emulsified oil and indeed nanoscale texturation can substantially modify such wettability. [11] Most membranes developed thus far to exploit nanoscale texturation are based on patterned polymeric nanostructures that are susceptible to degradation at high temperatures and pressures and furthermore often require complex patterning processes that can be cost prohibitive for deployment at scale. Ceramics and metals are resistant to high temperatures and pressures and can withstand corrosive environments. Their surfaces can furthermore be readily functionalized to tune interfacial energies and indeed ceramic and metal surfaces and membranes have been found to exhibit interesting wettability phenomena upon nanotexturation. [13,21]

The use of ZnO nanotetrapods is motivated by two central hypotheses: first, that the sharp protruding "arms" of the tetrapods will inevitably give rise to nanoscale texturation of any surfaces incorporating these structures irrespective of the specific orientation of nanostructures, thereby mitigating the need for precise lithographic patterning; and secondly, the irregular geometries of these nanostructures precludes close-packing and will inevitably yield a porous network that will allow for permeation of a liquid that wets the surfaces of these structures (**Fig. II.1**). Indeed, Figures II.2A—C indicate the hierarchical porosity defined by the interconnected network of ZnO nanotetrapods that span across the micron-sized pores of the metal meshes. The magnified SEM images in Figures II.2C and D indicate that the nanotetrapods define a "bed of nails". The Raman spectrum depicted in Figure II.2E is consistent with stabilization of hexagonal ZnO and the symmetry assignments of the modes are indicated in this figure. [20,22] The XRD pattern of the ZnO tetrapods depicted in Figure II.2F can be indexed to Joint Committee on Powder Diffraction Standards (JCPDS) # 36-1451, indicating the formation of phase-pure ZnO in the hexagonal zincite phase.

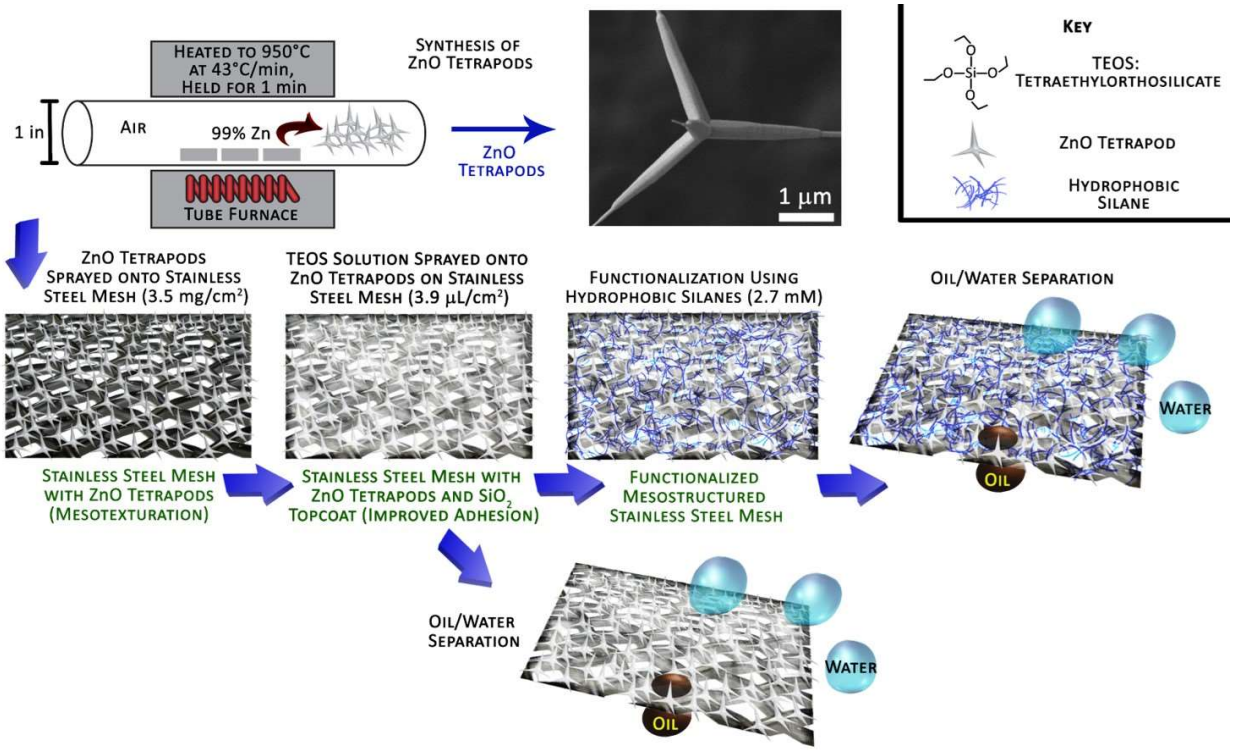

Figure II.1. A schematic representation illustrating the fabrication of surfaces for separating water/oil emulsions. The generation of the ZnO tetrapods and their subsequent coating onto meshes is depicted. The obtained membranes strongly repel water while allowing for rapid permeation of oil droplets, providing a means for separating the water and oil constituents of emulsions under ambient flow conditions based entirely on differential wettability.

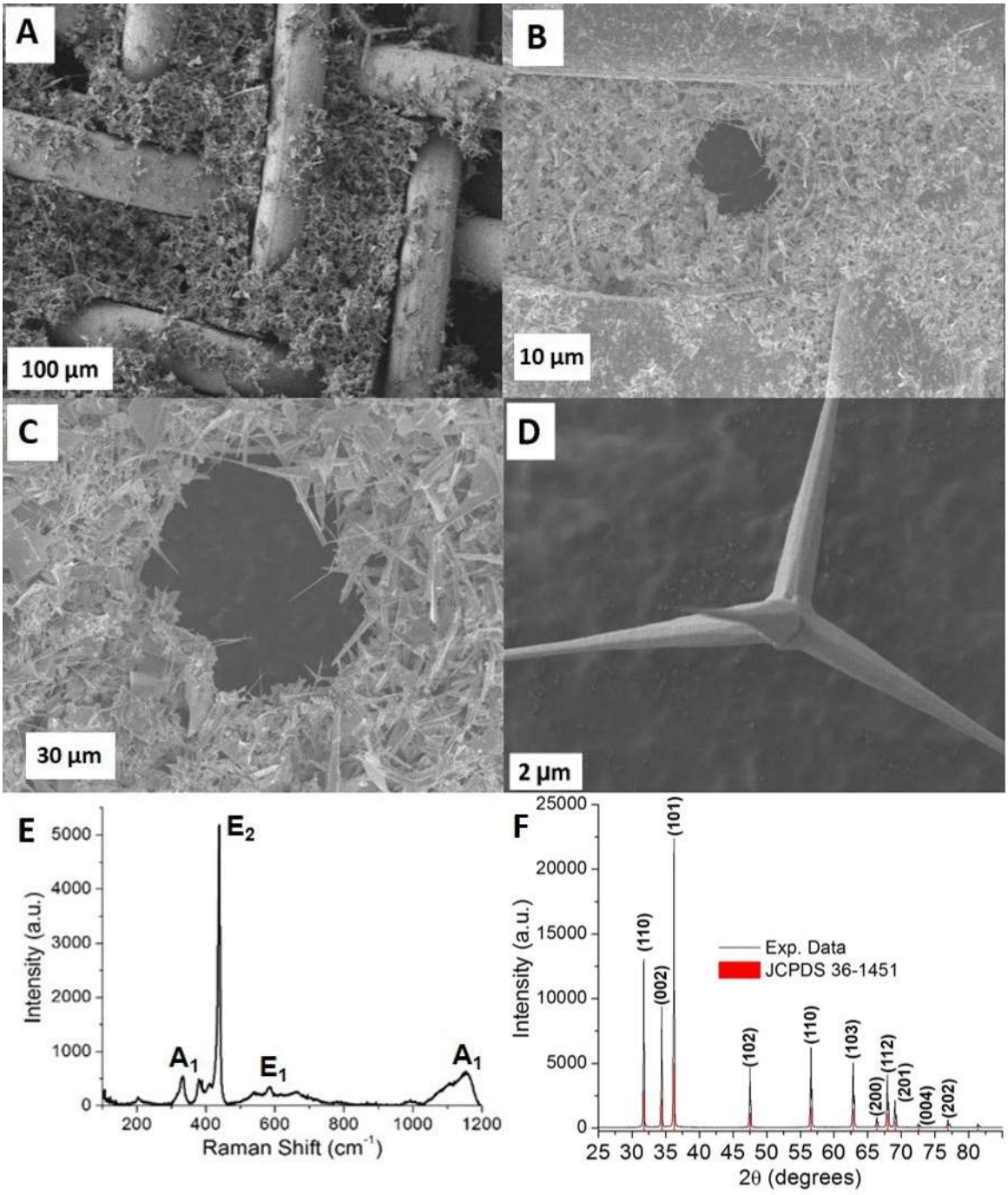

Figure II.2. (A-D) SEM images depicting the multiscale textured metal meshes modified by the deposition of ZnO nanotetrapods at various magnifications. (A) Several pores of the metal mesh with spray-deposited ZnO nanotetrapods; (B) Magnified view of a single stainless steel pore wherein interconnected ZnO nanotetrapods define multiscale porosity; (C) Magnified view of a nanotetrapod network and the resulting pore structure; (D) a single free-standing ZnO tetrapod. (E) Raman spectra and (F) XRD pattern acquired for ZnO nanotetrapods. The XRD pattern also indicates the reflections of the hexagonal zincite phase.

Upon initial spray deposition of the ZnO nanotetrapods onto the meshes, the nanostructures show rather poor adhesion. However, as indicated in Figure II.1, in order to improve the adhesion of the nanotetrapods on the stainless steel meshes, an amorphous SiO_2 shell is deposited by reaction with silanols obtained by the base-catalyzed hydrolysis of TEOS. The SiO_2 layer forms siloxane bonds between the surface hydroxyl groups of the nanotetrapods and the native oxide on the steel surfaces and imparts mechanical resiliency to the system. **Figure A.1** shows the results of ASTM 3359 testing of the samples assessed on a standardized scale of 0B to 5B with higher numerical figures representing better adhesion. In the absence of TEOS, the as-deposited coating is removed from almost every region of the scribed grid with a rating of 0B. However, upon the application of a SiO_2 coating, as schematically illustrated in Figure II.1, the highest rating of 5B is obtained. Notably, the tests have been performed on flat and clean steel substrates and thus mesh substrates with a greater degree of surface roughness are expected to provide a greater extent of adhesion. Figure A.1B indicates that the SiO_2 deposition results in a 450—550 g adhesion strength in ASTM D2197 scrape adhesion tests as compared to 0 g for tetrapods spray deposited without a TEOS layer.

The wettabilities of the hierarchically textured surfaces towards water and hexadecane have been characterized by water contact angle measurements. The hydrophobic nature of the metal mesh surfaces is amplified by the deposition of ZnO nanotetrapods (from 132 ± 3° to up to 154 ± 1°, **Figs. II.3A** and **B**), suggesting the manifestation of "bed of nails" Cassie—Baxter effect as a result of the hierarchical texturation defined by the deposition of nanotetrapods. Indeed, the manifestation of superhydrophobicity is further reflected by the rolling off of water droplets, akin to the "lotus leaf" effect when the substrates are tilted. [17,23] **Video A.1** demonstrates the strikingly amplified hydrophobicity of the samples after deposition of the ZnO nanotetrapods.

Intriguingly, the wettability of hexadecane on this surface provides a study in contrasts. The intrinsic high wettability of hexadecane on the metal mesh surfaces is greatly enhanced upon spray deposition of the ZnO nanotetrapods. Figures II.2C–E illustrate the complete (flash) spreading (to a contact angle of 0°) and permeation of hexadecane within 0.5 s (see also **Video A.1**, Supporting Information). The sharply differing wettability of the hierarchically textured surface towards water and oil, superhydrophobic non-wetting of water (inset to **Figure II.4I**) and flash spreading of hexadecane, suggests a facile means of achieving the separation of water/oil emulsions as clearly illustrated in Video A.1.

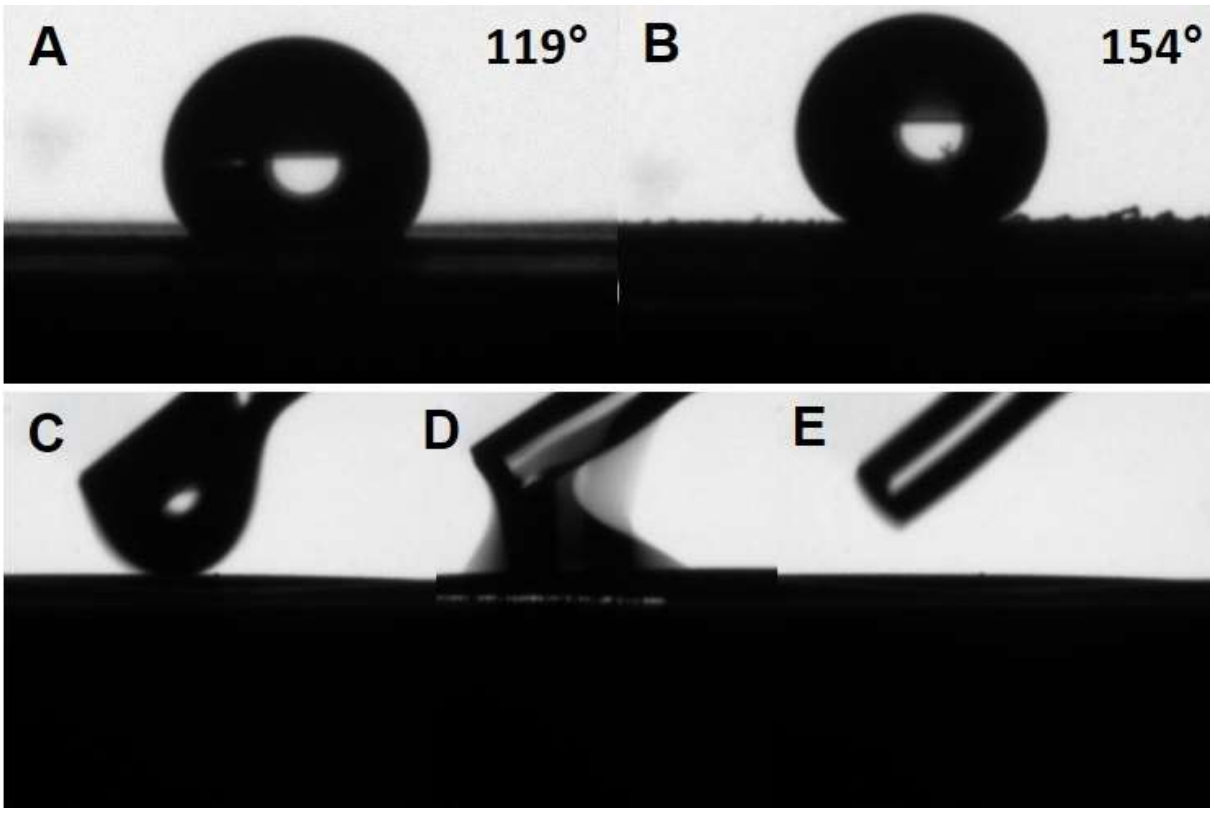

Figure II.3. Contact angles measured for (A) water on the stainless steel mesh and (B) water on the mesh coated with ZnO nanotetrapods. C—E) Hexadecane exhibits flash spreading to a contact angle of 0° on the coated mesh substrate as indicated by the sequences of images acquired at 0, 0.24, and 0.48 s.

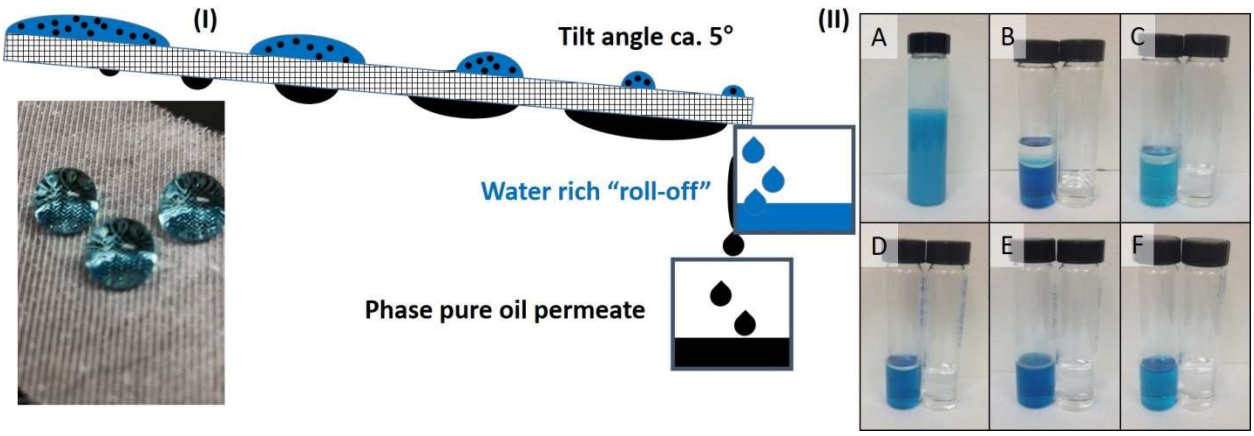

Figure II.4. (I) Schematic illustration of the experimental configuration deployed for water/oil separation. The inset depicts a digital photograph of water droplets (with a blue dye) that do not wet a stainless steel mesh with a spray-deposited coating of ZnO nanotetrapods. (II) A) 1:1 emulsion of water and hexadecane where the aqueous phase has been colored blue by inclusion of a blue dye; the subsequent images show the roll-off fraction (left) and permeate fraction (right) in each instance after effective separation lengths of (C) 21 cm; (D) 35 cm; (E) 60 cm; (F) 130 cm; and (G) 200 cm. In each instance, the emulsified hexadecane and water mixture is allowed to settle after the experiment prior to taking a digital photograph.

Figure II.4I schematically illustrates the experimental configuration used to examine the separation of 1:1 (v/v) water/hexadecane emulsions. Given the wettability of the hierarchically surface towards hexadecane, the permeate fraction is entirely hexadecane as apparent from visual observation and verified colorimetrically by the absence of a discernible spectroscopic signature of the blue dye (Fig. II.4II). In contrast, the fraction that "rolls off" the surface is enriched in water with the specific water to oil ratio dependent on the effective length of the substrate. It is worth noting that given the oleophilicity of the substrate, during the initial use of the membrane, hexadecane is adsorbed within the pores but this represents a one-time loss. The separation efficiency is not degraded by the adsorption of hexadecane in the pores and complete recovery of water and oil fractions is observed in subsequent cycles. The amount of adsorbed hexadecane is deduced to be 0.053 mL ± 0.009 mL of oil lost per square centimeter of the membrane based on

the recovered fractions. The specific flux rate depends on various parameters such as the temperature, mesh size, operational temperature, operational pressure, and design of the separation process. While near complete separation is evidenced here as a proof of concept, a realistic separation system can allow for higher flux rates by implementing a multi-level separation design. In order to quantify the efficacy of the separation process, the following figure of merit is used to define the extent to which the roll-off fraction is enriched in water under these conditions (ambient temperature, pressure, tilt angle of ca. 5°):

$$Water\ purity = \frac{V_W}{V_R} \times 100\% \quad (1)$$

where V_W is the volume of water and V_R is the total volume (oil and water) of the roll-off fraction. Since the starting emulsion is a 1:1 mixture of hexadecane and water, the initial water purity of all the samples is 50%. **Figure II.5** plots the water purity of the roll-off fraction (and thus the separation efficacy) as a function of the effective sample length indicating a clearly sigmoidal shape. A sample length of ca. 200 cm yields a roll-off fraction that is >99% water. The efficacy of separation as a function of path length is described very well by a sigmoidal Boltzmann function of the type:

$$Water\ purity = \frac{A_1 - A_2}{1 + e^{\frac{(effective\ length - x_0)}{\Delta\gamma}}} + A_2 \quad (2)$$

where the fitted parameters are A_1 = 50%; A_2 = 99.30%; x_0 = 27.92 cm; and $\Delta\gamma$ = 9.9. The constant term A_2-A_1 denotes the range of the fit in terms of water purity (from 50—99.3%), x_0 represents the center of the fit (in other words, the water purity is 75% at 27.92 cm), and $\Delta\gamma$ is a term that captures the extent of orthogonal wettability and is proportional to the interfacial energy difference ($\gamma_{hexadecane\text{-}surface} - \gamma_{water—surface}$).

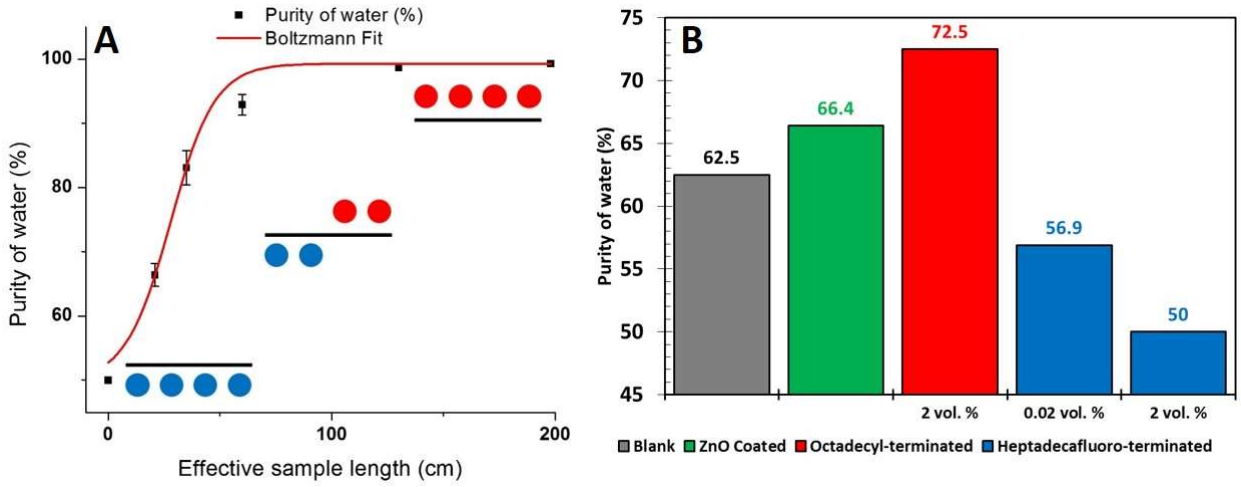

Figure II.5. (A) Plot of water purity (as defined in the text) as a function of the effective length of the hierarchically textured substrate. The plot is nicely described by a Boltzmann fit as discussed in the text. (B) Efficacy of separation (water purity of roll-off fraction) at an arbitrary path length of 21 cm for different surface treatments. The blank steel mesh is contrasted to the mesh functionalized with heptadecafluoro-1,1,2,2-tetrahydrodecyl)trimethoxysilane and n-octadecyltrichlorosilane.

While the specific parameters deduced from this fit are sensitive to the separation conditions deployed here (temperature, pressure, tilt angle, viscosities of liquids), the Boltzmann shape is generalizable and provides insight into the phenomena observed here. The magnitudes of the latter two numbers captures the efficacy of the surface in separating water and oil. The 27.92 cm metric represents the length of the substrate required to obtain a 50% separation efficiency under ambient temperature and pressure; similarly, the higher the value of $\Delta\gamma$, more efficacious the surface at separating water and oil. Such a Boltzmann fit can be rationalized in physical terms considering a two-state probabilistic function wherein an oil droplet within an emulsion can adopt one of two states: either permeating through the hierarchically textured mesh or continuing to propagate along the length of the mesh. The probability of permeation is increased with increasing path length given the energetic preference for wettability of hexadecane. In other

words, permeation corresponds to the low-energy state, whereas propagating along the path is the high-energy state that is nevertheless accessible as a result of the kinetic energy that the droplet possesses. The Boltzmann shape is analogous to an adiabatic system of particles that can access discrete energy states wherein the states are populated depending on the temperature.[24] This description is remarkably useful in describing energetically driven partitioning in systems such as folded and unfolded proteins, open and closed ion channels,[24-26] and coiled and uncoiled DNA. In this system, depending on the energy of the oil droplet and the interfacial energy, the droplet can permeate the membrane or propagate along its length; the Boltzmann shape establishes the discrete population distribution. The continued removal of hexadecane gives rise to an open two-phase system, which drives the system towards increasing water purity. The samples have been reused in excess of 12 times without degradation or failure.

Indeed, such an analysis is supported by the data in Figure II.5B, which contrasts the purity of the roll-off fraction (and thus the separation efficiency) for variously functionalized samples at a path length of 21 cm. Functionalizing the surfaces with octadecyltrichlorosilane results in pendant octadecyl groups, thereby increasing the hydrophobicity and oleophilicity of the substrates (and increasing the value of $\Delta\gamma$). The separation efficiency is seen to be increased by >6% for the same path length. However, functionalizing the surfaces with a fluorinated silane, heptadecafluoro-1,1,2,2-tetrahydrodecyl)trimethoxysilane, renders the surface simultaneously more hydrophobic and more oleophobic, and by reducing $\Delta\gamma$ decreases the separation efficiency (note that functionalization does not alter the hierarchically textured morphology as indicated by the SEM images in **Figure A.2** of the Supporting Information). Upon functionalization of the surfaces with a 2 vol.% solution of heptadecafluoro-1,1,2,2-tetrahydrodecyl)trimethoxysilane, the surface is rendered omniphobic and no separation is possible.

The underlying principle of the separation achieved here is orthogonal wettability of the two liquids as modified by hierarchical texturation and molecular modification. The basis for this separation can be understood keeping in mind that when a liquid droplet comes into contact with a solid surface, the extent of its dispersion on the surface and the eventual shape of the droplet is determined by the balance between interfacial energies at the solid—vapor, liquid—vapor, and vapor—liquid interfaces. As a liquid spreads onto a surface, the existing solid—vapor interface is replaced by new liquid—vapor and vapor—liquid interfaces. The equilibrium contact angle (θ_e) reflects the balance between the three types of interfacial energies and can be written as:

$$cos\theta_e = \frac{\gamma_{SV} - \gamma_{SL}}{\gamma_{LV}} \quad (3)$$

where θ_e is the equilibrium contact angle, and the γ terms are the interfacial energies for the solid—vapor (SV), solid—liquid (SL), and liquid— vapor (LV) surfaces. Even this simple formulation for the contact angle of a flat substrate provides key insight into achieving orthogonal wettability so as to be able to separate disparate liquids. In order for a surface to be non-wettable towards a liquid ($\theta e > 120°$), γ_{SL} must be (substantially) greater than γ_{SV}. In other words, the intrinsic surface energy of the surface (a solid—vapor surface energy) must be as low as possible and the solid—liquid interfacial energy must be as high as possible.[27] Conversely, for the liquid to completely wet the surface ($\theta e = 0°$), the intrinsic surface energy corresponding to the solid—vapor surface energy must be greater than the solid—liquid interfacial energy and the latter term should be as small as possible. [28] When considering the wettability of a single surface by two different liquids, the γ_{SV} term is the same in both cases and thus both the sign and magnitude of $\cos\theta_e$ and ultimately the wettability of the two liquids is dictated by the relative value of γ_{SL} with respect to γ_{SV}. Two distinct parameters strongly affect this balance: (a) the

surface tension of the liquid (in other words, the cohesive forces and the nature of the liquid itself) and (b) the chemical compatibility of the surface with the liquid (which is a function of the molecular interactions at the interface). This analysis suggests that for a specific range of γ_{SV}, two liquids with very different values of γ_{SL} could yield opposite signs of $\cos\theta_e$ for the same surface, thereby allowing one liquid to be selectively retained and permitting the second to flow through without wetting the surface. Water and hexadecane have very different surface tension values (water has a surface tension of 72.80 x 10^{-3} N/m, whereas hexadecane has a surface tension of 27.47 x 10^{-3} N/m at 293 K). [18] The lower surface tension of hexadecane implies that the γ_{SL} term is likely to be smaller enabling this liquid to more readily wet a surface. This difference in surface tension values and interfacial interactions with the coated meshes underpins the efficacious separation of the two liquids observed here. Similar behavior is observed for heavier oil fractions albeit with reduced flux rates.

Considering the balance of interfacial energies alone, the separation of two liquids would be viable only for a relatively narrow range of γ_{SV} surface energies. However, the effect of surface roughness is to amplify the intrinsic wettability of a surface without changing the sign of $\cos\vartheta_e$[15,16,29,30] The hierarchical texturation constituted by integrating ZnO tetrapods with nanoscale features onto micrometer-sized meshes greatly amplifies the differential wettability of hexadecane and water by rendering the surface more wettable to hexadecane and more repellant towards water. **Figure A.3** indicates the dimensions of an individual ZnO nanotetrapod. Based on calculations of the exposed surface area of tetrapods with conical arms (ca. 3.90 μm in length with a diameter of ca. 0.56 μm, a roughness value *r* of ca. 4.5 is deduced for an individual nanotetrapod, where *r* reflects the ratio of the effective exposed surface area to the equivalent surface area of a smooth ZnO surface and would serve as a modifier to Eq. I.3 in the Wenzel

regime. Interconnected networks such as shown in Figures 2C and **A.2** have multiple interconnected tetrapods that would yield *r* values of ca. 9—14, suggesting a high degree of texturation. In other words, for two liquids that present opposite signs of $\cos\theta$, hierarchical texturation serves to exacerbate the differences in wettability. The $\Delta\gamma$ term that is derived from the Boltzmann fit in **Figure II.5A** is thus a measure of this differential wettability. Modifying the surfaces with silane monolayers further allows for modulation of the interfacial interaction term γ_{SL} as noted in Chapter I, Eq. I.3. Upon functionalization with an octadecyl-terminated silane, given that the pendant moiety is non-polar, the surface is rendered more oleophilic and more hydrophobic and thus further increases the magnitude of the wettability difference (and enhances the separation efficiency). In contrast, the fluorinated hydrocarbon exposes C—F bonds that interact only weakly with both water and hexadecane, and thus renders the surface at once more hydrophobic as well as more oleophobic and thus diminishes the wettability difference, thereby degrading the separation efficiency.

II.5 Conclusions

A facile and readily scalable approach has been developed to prepare hierarchically textured architectures by integrating ZnO tetrapods with nanoscale features onto micron-sized metal meshes. The permeable hierarchically textured architectures show pronounced differences in wettability towards water and hexadecane and such orthogonal wettability is used to achieve the separation of water/hexadecane emulsions. Separation efficiencies well over 99% are routinely accessible at room temperature and pressure by simply flowing emulsions across these hierarchically textured surfaces. The separation efficiency as a function of effective path length is fit with a Boltzmann expression that can be rationalized as a two-state probabilistic function for oil droplets within the emulsion encountering the hierarchically textured surface. The

separation efficiency can further be tuned by altering γ_{SL} by surface functionalization with silane monolayers. A viable flow system for separating heavy oil and water components of real-world emulsions with simultaneous optimization of selectivity and flux rate was performed by varying the membrane pore size, ZnO nanotetrapod loading, and temperature as detailed in Chapter III.

II.6 References

[1] A. M. Albahlani and T. Babadagli, *J. Pet. Sci. Eng.* **2009**, 68 (3-4), 135.

[2] A. M. Albahlani and T. Babadagli, *SPE* 2008, No. c, 1-22.

[3] M. Cheryan and N. Rajagopalan, *Memb. Sci.* **1998**, *151* (1), 13–28.

[4] B. Solomon, M. Hyder, and K. Varanasi, *Sci. Rep.* **2014**, *4*, 5504.

[5] J. Howarter and J. Youngblood, *J. Colloid Interface Sci.* **2009**, *329* (1), 127–132.

[6] P. Brown, O. D. L. A. Atkinson, and J. P. S. Badyal, *Appl. Mater. Interfaces* **2014**.

[7] M. T. Ravanchi, T. Kaghazchi, and A. Kargari, *Desalination* **2009**, *235* (1-3), 199–244.

[8] Z. Wang, X. Jiang, X. Cheng, C. H. Lau, and L. Shao, *ACS Appl. Mater. Interfaces* **2015**, *7* (18), 9534–9545.

[9] Y. Zhu, D. Wang, L. Jiang, and J. Jin, *NPG Asia Mater.* **2014**, *6* (5), e101.

[10] Y. Si, Q. Fu, X. Wang, J. Zhu, J. Yu, G. Sun, and B. Ding, *ACS Nano* **2015**, *9* (4), 3791–3799.

[11] K. Li, J. Ju, Z. Xue, J. Ma, L. Feng, S. Gao, and L. Jiang, *Nat. Commun.* **2013**, *4*, 2276.

[12] S. Cobos, M. S. Carvalho, and V. Alvarado, *Int. J. Multiph. Flow* **2009**, *35* (6), 507–515.

[13] J. M. Velázquez, A. V. Gaikwad, T. K. Rout, R. E. Baier, E. S. Furlani, and S. Banerjee, *J. Mater. Chem.* **2012**, *22* (8), 3335–3339.

[14] L. Gao and T. J. McCarthy, *Langmuir* **2007**, *23* (7), 3762–3765.

[15] P. Roach, N. J. Shirtcliffe, and M. I. Newton, *Soft Matter* **2008**, *4* (2), 224.

[16] D. Quéré, *Annu. Rev. Mater. Res.* **2008**, *38* (1), 71–99.

[17] N. J. Shirtcliffe, G. McHale, S. Atherton, and M. I. Newton, *Adv. Colloid Interface Sci.* **2010**, *161* (1-2), 124–138.

[18] W. M. Haynes, *CRC Handbook of Chemistry and Physics, 95th Edition*, 95th ed.; Lide, D. R., Bruno, T. J., Eds.; CRC Press.

[19] J. M. Velazquez, A. V Gaikwad, T. K. Rout, J. Rzayev, and S. Banerjee, *ACS Appl. Mater. Interfaces* **2011**, *3* (4), 1238–1244.

[20] B. J. M. Velazquez, S. Baskaran, A. V Gaikwad, X. He, M. M. Oye, M. Meyyappan, T. K. Rout, J. Y. Fu, and S. Banerjee, *ACS Appl. Mater. Interfaces,* **2013,** 5, 10650−10657.

[21] M. A. Gondal, M. S. Sadullah, M. A. Dastageer, G. H. McKinley, D. Panchanathan, and K. Varanasi, *ACS Appl. Mater. Interfaces* **2014**, 1–26.

[22] R. Cuscó, E. Alarcón-Lladó, J. Ibanez, L. Artús, J. Jiménez, B. Wang, and M. J. Callahan, *Phys. Rev. B* **2007**, *75* (16), 165202.

[23] H. J. Ensikat, P. Ditsche-Kuru, C. Neinhuis, and W. Barthlott, *Beilstein J. Nanotechnol.* **2011**, *2* (1), 152–161.

[24] R. Phillips, J. Kondev, J. Theriot, and H. Garcia, *Physical Biology of the Cell*, 2nd ed.; Garland Science.

[25] J. E. Molloy and M. J. Padgett, *Proc. Nat. Acad. Sci. USA* **2017**, *72*, (11).

[26] D. E. Pulleyblank, M. Shure, D. Tang, J. Vinograd, and H. P. Vosberg, *Proc. Nat. Acad. Sci. USA* **2017**, *72*, (11), 4280-4284.

[27] S. Wang, L. Feng, H. Liu, T. Sun, X. Zhang, L. Jiang, and D. Zhu, *ChemPhysChem* **2005**, *6* (8),

[28] G. A. Horrocks, M. F. Likely, J. M. Velazquez, and S. Banerjee, *J. Mater. Chem. A* **2013**, *1* (48), 15265.

[29] J. Drelich and E. Chibowski, *Langmuir* **2010**, *26* (24), 18621–18623.

[30] J. A. Lee and T. J. McCarthy, *Macromolecules* **2007**, *40* (11), 3965–3969.

CHAPTER III

SEPARATION OF VISCOUS OIL EMULSIONS USING 3D NANOTETRAPODAL ZNO MEMBRANES

III.1 Outline

The steam-assisted gravity-drainage (SAGD) method has emerged as amongst the leading methods of enhanced oil recovery and is predicated on the injection of steam within the wellbore followed by extraction of emulsions of viscous oil and water. The emulsions are stabilized by endogenous surfactants, necessitating extensive processing such as addition of chemical de-emulsifiers and slow gravity-based separation methods. Here, we show that a hierarchically textured membrane exhibiting orthogonal wettability, specifically, superoleophilic but superhydrophobic behavior, allows for effective separation of the water and viscous oil fractions of SAGD emulsions. The membrane is constructed by integrating ZnO nanotetrapods onto stainless-steel meshes using a conformal amorphous SiO_2 layer and is both mechanically resilient and thermally robust. Water content in permeated bitumen is reduced down to as low as 0.69 vol.% through a single-pass filtration step with the further advantage of eliminating silt particles. The permeation temperature and water content are tunable based on modulation of the mesh size and ZnO loading. The membranes allow for operation at SAGD temperatures in excess of 130°C, thereby enabling the thermal disruption of hierarchical emulsions. The membrane-based separation of SAGD emulsions under process conditions paves the way for entirely new process designs for recovering dry viscous oil.

III.2 Introduction

The worldwide consumption of oil has increased at a steady pace since the 2008 global recession and is now greater than at any previous time in history.[1] In order to meet global energy needs, tapping into unconventional geological deposits such as the Canadian Oil Sands in Northern Alberta and Saskatchewan has emerged as a critical imperative.[2] Some estimates suggest that the Canadian Oil Sands hold as much as *ca.*170 billion barrels of readily accessible deposits.[1,3] The production of viscous oil is beset by many challenges due to its remarkably high viscosity under reservoir conditions.[4] A broad spectrum of methods is used to extract viscous oil from subsurface reservoirs that are too deep for strip mining, spanning the range from chemically aided processes to miscible extraction (involving the injection of CO_2 or miscible solvents) and the steam-assisted gravity drainage (SAGD) method.[2,4,5] The latter SAGD method was initially introduced in the 1970's and has since turned out to be one of the most important methods of enhanced oil recovery.[4,6,7] In this process, steam is injected continuously from an upper horizontally drilled well into a growing steam chamber. As the injected steam enters the chamber, it moves to the edges of the chamber where it condenses. As the temperature in the steam chamber increases, the cold oil becomes less viscous and flows down towards a lower production well.[8–10] The major advantage that the SAGD method has over other conventional steam flooding methods is that in SAGD, the temperature in the steam chamber is constant and the same as that of the temperature of the steam. As such, the SAGD-extracted bitumen stays hot as it flows towards the production well.[6,11] Powerful cavity pumps bring the mixture of condensed water and bitumen to the surface from the production well. The recovered fluid oftentimes comprises recalcitrant emulsions stabilized by endogenous surfactants such as natural organic matter.[12–14] Here in Chapter III, we demonstrate the high-temperature separation of SAGD emulsions to obtain viscous oil with

water content as low as 0.69 vol.% based on the orthogonal wettability of a 3D nanotetrapodal ZnO membrane towards water and oil.

Owing to the presence of endogenous surfactants and as a result of the extensive mechanical agitation induced by rapid steam injection and subsurface fluid flow during the SAGD process, water droplets suspended within viscous oil can be quite stable in terms of their dispersion.[4,12,15] Depending on the relative amounts of the two liquids, oil-in-water or water-in-oil emulsions are stabilized. Indeed, hierarchical complex emulsions are often generated. Orchestrating the efficacious separation of the water and oil components of the emulsions, particularly the separation of emulsified oil, is imperative both for increasing the efficiency of the extractive processes as well as to meet regulatory requirements for the treatment of produced water.[16] Current processes to achieve such separations primarily involve gravity based separation and de-emulsification, which require the addition of large volumes of chemicals, necessitates long periods of time to allow complete settling, and is of limited efficacy in terms of removal of emulsified sub-micron-sized droplets.

A number of different porous membrane architectures have been developed for separating the water and oil components of emulsions[17,18] Many such architectures seek to exploit the vast differential in the surface tension values of the two liquids, which leads to substantial differences in how these liquids wet surfaces. Considering Young's formalism for a textured surface characterized by a roughness parameter *r* (corresponding to the ratio of the surface area of the textured surface to the surface area of an equivalent smooth surface), the observed contact angle (θ_w) can be written as:

$$cos\theta_W = \frac{r(\gamma_{SV}-\gamma_{SL})}{\gamma_{LV}} = rcos\theta_e \ldots\ldots \quad \text{(III.1)}$$

where θ_e is the equilibrium contact angle, γ_{SV} represents the interfacial energy of the solid/vapor surface, γ_{SL} represents the solid/liquid interfacial energy, and γ_{LV} represents the liquid/vapor interfacial energy.[19–21] Taking the wettability of a single surface by two different liquids into account, the γ_{SV} term is identical for both cases. The sign and magnitude of $\cos\theta_e$ and the resulting wettability of the two liquids depends ultimately on the numerical value of γ_{SL} with respect to γ_{SV}. This differential is strongly affected by: (a) the surface tension of the liquid and (b) the chemical interaction of the surface and the liquid. Such an evaluation therefore demonstrates that two liquids with disparate values of solid-liquid interfacial energies (γ_{SL}), given a range of solid-vapor interfacial energies (γ_{SV}), can exhibit opposite signs of $\cos\theta_e$ for the very same surface.[18] As a result, interfacial interactions can be used to affect the separation of two such disparately wetting liquids wherein the wetting liquid permeates a porous surface, whereas the non-wetting liquid is retained. The surface roughness parameter acts as a multiplier in Equation III.1 and further boosts the orthogonal wettability by rendering the surface more wettable towards a lower surface tension liquid and less wettable towards a high surface tension liquid. [19,22–24] While the idea of orthogonal wettability is attractive in principle, it has not thus far been used for the separation of SAGD or analogous recalcitrant viscous oil emulsions. The primary reason for this is that a large proportion of orthogonally wettable membrane architectures developed thus far utilize polymeric components that are unable to withstand the high temperatures and pressures required to process SAGD emulsions.[17] Furthermore, many intricately textured surfaces are readily damaged and prone to rapid fouling by clay particles and sediments that are present within SAGD emulsions. Here, we demonstrate the high-temperature separation of SAGD emulsions utilizing mechanically resilient and thermally robust 3D nanotetrapodal ZnO/stainless steel mesh membranes that permeate viscous oil whilst remaining

impervious to water.[18] The pore size of the stainless steel mesh and the loading of ZnO tetrapods can be tuned to modulate the bitumen permeation temperature. Whist the continuous water phase is readily eliminated from the permeated bitumen, high permeation temperatures are imperative to disrupt the complex hierachical emulsions and separate entrapped microdroplets of water. Such readily scalable architectures allow for water content in permeated bitumen to be reduced below 0.70 vol.%, well below the 1.0 vol.% specification necessary for further processing of viscous oil at refineries.

III.3 Materials and Methods

III.3.1 Preparation of ZnO Tetrapods

ZnO tetrapods were prepared based on the rapid oxidation of metallic Zn foils in air as described in Chapter II.[18,25–27] Briefly, Zn metal sheets (0.008 in thickness) were cut into substrates with approximate dimensions of 3 mm x 3mm. The diced Zn substrates were then placed onto a boat like stainless-steel mesh and placed within a 1" diameter quartz tube, which was then placed within a tube furnace (Lindburg/BlueM).[25] The substrates were heated at a rate of 43°C/min until a maximum temperature of 950°C. The furnace was then held at 950°C for 1 min and then allowed to cool.

III.3.2 Preparation of ZnO Tetrapod/Stainless-Steel Mesh Membranes

The collected ZnO tetrapods were dispersed by ultrasonication in 2-propanol (99.9%, Fisher Scientific) to obtain dispersions with a concentration of *ca.* 20 mg/mL. The dispersion was then spray coated onto stainless steel mesh substrates with a variety of pore sizes (McMaster-Carr) using a Master airbrush with a nozzle diameter of 0.5 mm and an air compressor with output

pressure of 310 kPa. To facilitate the removal of solvent during the coating process, the stainless steel meshes were held at a temperature of *ca.* 120°C. Next, a modified Stöber method was used to deposit a layer of amorphous SiO_2 using tetraethylorthosilicate (TEOS) as the precursor in order to covalently link the ZnO tetrapods to the underlying stainless steel mesh.[28,29] The SiO_2 layer prevents sloughing and endows mechanical resilience to the 3D nanotextured membranes. The solution spray coated on the stainless-steel mesh comprised a mixture of 80 vol.% ethanol (99.5+%, Koptec), 18.5 vol.% deionized water (ρ = 18.2MΩ·cm^{-1}), 1 vol.% of an aqueous solution of 28—30% NH_4OH, and 0.5 vol.% TEOS (99.999+% metals basis, Alfa Aesar).

III.3.3 Characterization of ZnO Tetrapods and Membranes

The ZnO tetrapod morphology and the 3D nanotetrapodal membranes were imaged utilizing a JEOL JSM-7500F field-emission scanning electron microscope (FE-SEM). The instrument was equipped with a high brightness conical FE gun with a low aberration conical objective lens. The source was a cold cathode UHV field emission conical anode gun. An accelerating voltage of 10 kV was used to image the structures. Mechanical testing was performed using ASTM method D3359, which used a standardized scraping tool to score the sample. Next, an adhesive tape was applied to evaluate the extent to which the coating was removed. In addition, the ASTM D2197 method was used whereain a U-shaped loop was brought to the surface and weights were added until the coating was removed from the substrate. Both of these standardized tests have been described in detail in Chapter II.[27]

III.3.4 SAGD Emulsions

The viscous oil emulsion used here was extracted from the Northern Alberta Oil Sands by Cenovus Energy, Inc. *via* the SAGD method. While bituminous emulsions are typically quite

stable, some separation may occur during storage and transportation. Therefore, the emulsions were reconstituted by combining one part of the oil phase and five parts of the excess aqueous phase in a 500 mL container. The liquids were then heated to 60°C and stirred vigorously stirred with a magnetic stir bar for 2 h while keeping the temperature constant. The remaining excess aqueous phase was decanted, and the resulting viscous emulsion was used for all testing.

III.3.5 Separation of Emulsions

A thermal autoclave testing apparatus (built from glass to facilitate *in situ* observations of viscous oil permeation) was obtained from Parr Instrument Company (model #5112) and used to model the high-pressure and high-temperature conditions characteristic of the SAGD process. A custom glass insert was placed inside the thermal autoclave to observe the permeation of bitumen through the membranes (**Figure A.4A**). The membrane was held in place using rubber o-rings and the emulsion was added to the top surface. A hole was drilled on the lower end of the insert to ensure pressure equilibration across the membrane. In other words, both sides of the membrane are exposed to the same autogeneous pressure generated within the autoclave by boiling water. The autoclave allows for reactor temperatures of up to 200°C and autogenous pressures of up to 900—1000 kPa.

In order to characterize the process environment, the system was filled with 250 mL of deionized water and heated to temperatures in the range of 110—200°C. The increase of temperature with time and the evolution of the autogenous pressure with temperature are plotted in **Figures A.5** and **A.6**, respectively.

For each membrane configuration, separation experiments were performed in triplicate to obtain statistically meaningful results. Observations of the permeation temperature and flux rates were facilitated by the glass construction of the vessel and insert.

III.4 Characterization of Permeate

Water content in the permeate was examined using the Dean-Stark method. Given the viscous nature of the permeated bitumen, toluene was mixed with the recovered permeate and then refluxed for 2 h to collect and measure water content in the permeate. Typical volumes of permeate were approximately 10 mL or greater. The setup utilized a three-neck round bottom flask as the still; a thermocouple was inserted to measure temperature as the sample was warmed using a heating mantle. A reflux condenser with a graduated glass trap (10 mL) was used to collect the water and toluene upon condensation.

For samples with water content below 0.1 mL, Karl—Fischer titrations were performed using a Mettler-Toledo C20 Coulometric Titrator. The electrolyte used for both the analyte and the catholyte was Hydranal Coulomat E (Sigma Aldrich).

The permeate fractions were further examined by an Olympus BX41 optical microscope. In order to perform the analysis, the permeated fraction was deposited between two thin glass microscope slides with no additional dilution.

III.5 Results and Discussion

The design of an entirely inorganic membrane is imperative to facilitate the separation of SAGD emulsions at high temperatures and pressures. However, to the best of our knowledge, no membrane-mediated separation of SAGD emulsions has been reported thus far in either the

academic or patent literature. In Chapter II, we have demonstrated that ZnO tetrapods integrated onto stainless steel mesh substrates strongly repel water (superhydrophobic with water contact angles >150°) but are wetted by hexadecane (superoleophilic with a contact angle of 0°).[18] Functionalization of the ZnO tetrapods with 1*H*,1*H*,2*H*,2*H*-perfluorooctanephosphonic acid yields a helical monolayer that further renders the surface both superoleophobic (viscous oil contact angles >156°) and superhydrophobic (water contact angles >165°).[26] In Chapter III, we evaluate the efficacy of ZnO/stainless-steel mesh architectures in affecting the separation of SAGD emulsions from the Alberta Oil Sands at high temperatures and pressures. Structure—processing—function maps are developed under realistic hydrothermal process conditions by performing the separation within a custom-designed glass autoclave reactor. The following parameters have been evaluated as a function of the ZnO loading and pore size: (a) the permeation temperature (defined as the temperature at which visible permeation of the bitumen was observed while ramping the temperature in increments of 10°C and where each temperature was held for a minimum of 30 min); (b) the separation efficacy, specifically the water content in the viscous oil permeate (determined by Dean—Stark's distillation or Karl—Fischer titration); and (c) the flux rate (determined by monitoring the collection of the permeate using a calibrated receptacle). **Figure III.1** depicts the process flow beginning from the generation of ZnO tetrapods, to the separation of emulsions under hydrothermal conditions.

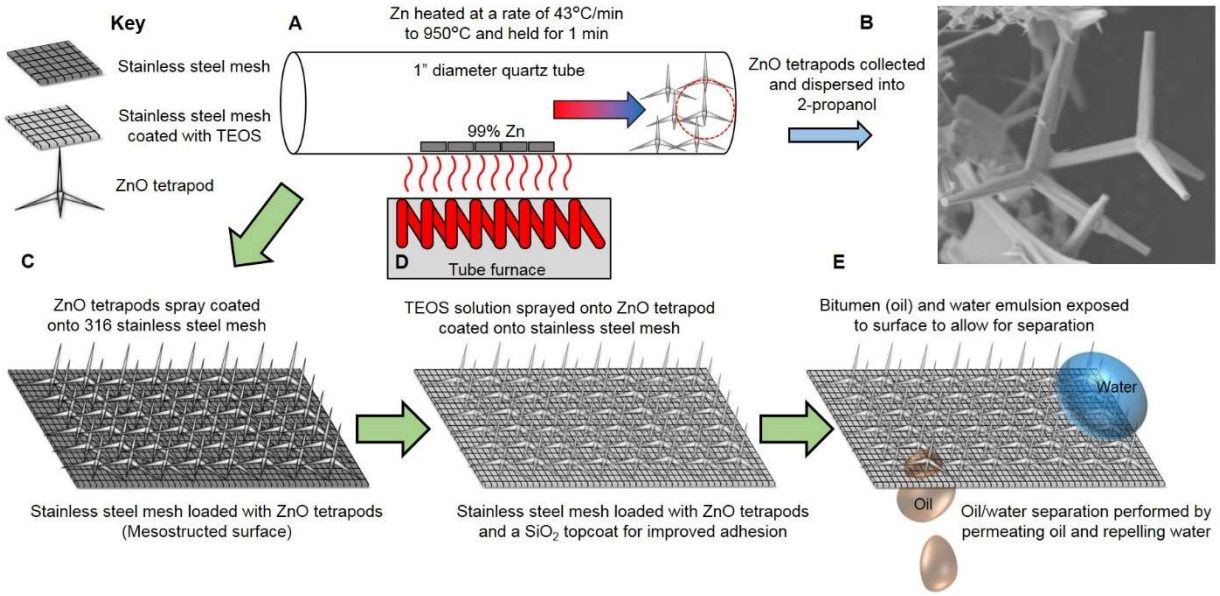

Figure III.1. Process Flow Diagram for the Preparation of ZnO/Stainless Steel Mesh Membrane Architectures and their Utilization in the Separation of SAGD Emulsions. (A) Schematic depicting preparation of ZnO tetrapods from Zn metal; (B) collection and subsequent dispersion of ZnO tetrapods within 2-propanol by ultrasonication; (C) spray coating of ZnO tetrapods dispersed in 2-propanol onto 316 stainless steel mesh substrates with variable pore dimensions; (D) coating with TEOS to increase adhesion of tetrapods to the stainless steel mesh by constituting an interfacial SiO_2 layer; (E) deployment of the membrane architectures under hydrothermal conditions to bring about the separation of SAGD emulsions based on the differential wettability of water and viscous oil towards these surfaces.

The use of ZnO nanotetrapods as the primary building blocks for constructing membranes to bring about the separation of SAGD water/viscous-oil emulsions is motivated by two primary factors. First, the thorn-like structure of the ZnO tetrapods imparts hierarchical multiscale texturation to the stainless steel mesh surfaces, thereby rendering the substrates hydrophobic and facilitating the use of orthogonal wettability to separate liquids with disparate surface tensions.[18,30,31] Secondly, the tetrapodal geometry of the nanostructures precludes close-packed ordering thereby creating a porous architecture that permits the permeation of wetting liquids.

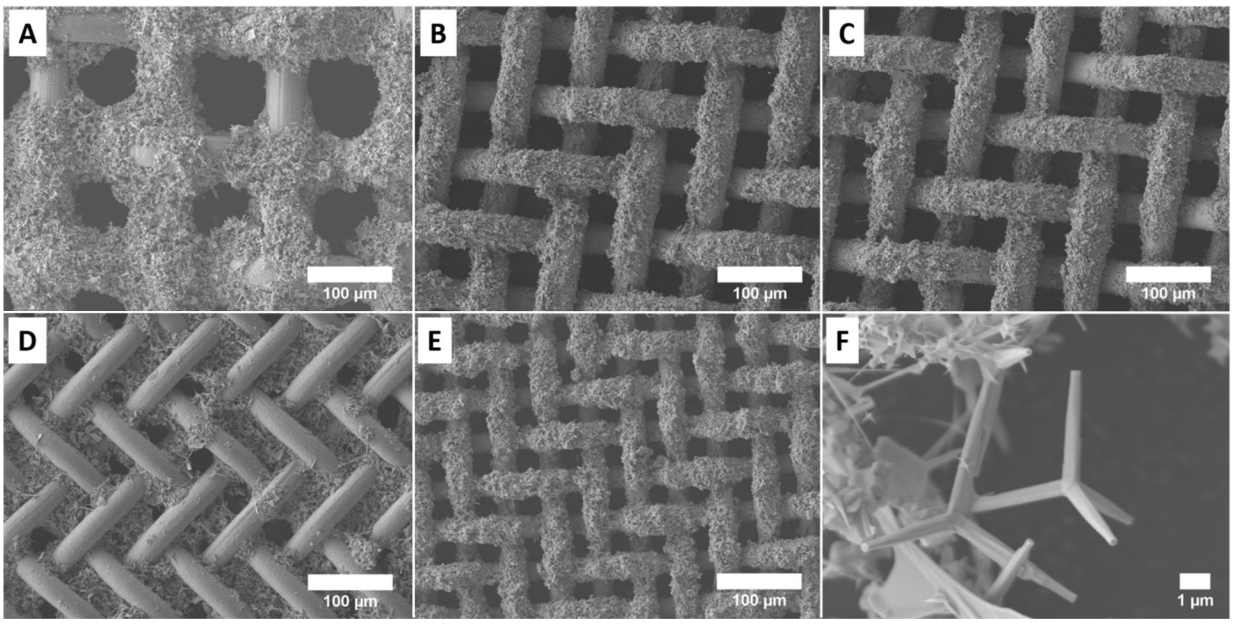

Figure III.2. Texturation and Porosity of 3D Nanotetrapodal Membrane Architectures. A—E) SEM images depicting stainless steel meshes exhibiting multiscale texturation as a result of the deposition of ZnO nanotetrapods. In A—E, the mesh size is altered whilst maintaining the ZnO loading constant at ca. 7.0 mg/cm^2. The meshes have square pores defined here by the edge dimensions. A) A 180-gauge textured stainless steel mesh with a pore size of ca. 84 µm; B) 250 gauge textured stainless steel mesh with a pore size of ca. 61 µm; C) 325-gauge textured stainless steel mesh with a pore size of ca. 43 µm; D) 400 gauge textured stainless steel mesh with a pore size of ca. 38 µm; E) 500-gauge textured stainless steel mesh with a pore size of ca. 30 µm. F) SEM image of individual ZnO tetrapods at increased magnification.

Figure III.2 indicates the multiscale texturation and porosity defined by the interconnected network of ZnO nanotetrapods that span across the pores of the stainless steel mesh substrates, thereby yielding a 3D porous architecture. The SEM images demonstrate that the tetrapods form an enmeshed network atop the steel substrates. The high-magnification SEM image in **Figures III.2F** further shows that the nanotetrapods define an interconnected network that precludes close packing. Increasing the loading (or conversely reducing the pore size) results in greater accumulation of ZnO tetrapods within the pores wherein they reduce the effective pore size.

Membranes for separation of SAGD emulsions need to be mechanically resilient to withstand flow conditions, high pressures, and abrasion from silt particles impinging on the surfaces. The

deposition of a conformal amorphous SiO_2 shell that forms siloxane bonds both to the steel surfaces as well as to hydroxyl groups on the ZnO surfaces helps to adhere the ZnO tetrapods to the stainless steel mesh surfaces. The SiO_2 overlayer is grown by spray coating a mixture of TEOS and NH_4OH onto the mesh substrates thereby facilitating hydrolysis and condensation reactions.[29,32] The TEOS and NH_4OH loading described in the Methods section of Chapter III yields a rating of 5B as per American Society for Testing of Materials (ASTM) D3359 for a test specimen wherein the tetrapods are adhered to a planar steel substrate.[26,27] ASTM D2197 tests furthermore indicate a scrape adhesion strength of 450-550 g. Thermogravimetric analyses for these samples indicate that they retain their structural integrity up to a temperature of 900°C as reported in Chapter IV.[26]

Figures III.3A and B show representative optical microscopy images of SAGD emulsions prior to treatment. The water content for reconstituted SAGD emulsions is estimated to be *ca.* 30 vol.% based on Dean—Stark's distillation. Water and oil are clearly distinguishable with water being the lighter and more transparent fraction. The images indicate that the emulsions have a complex hierarchical structure with water droplets dispersed within a continuous oil phase; the water droplets further contain oil droplets and asphaltene residues. The complex nature of these emulsions, stabilized as a result of endogenous surfactants such as humic acid, render the separation of water and oil emulsions rather difficult.[12–14] **Figures III.3C—J** depict optical microscopy images of (undiluted) permeated fractions collected after separation through various stainless steel meshes all with a loading of 14 mg/cm^2 of ZnO tetrapods. With decreasing pore size, the temperature at which viscous oil permeates the membrane is successively increased (*vide infra*). It is readily evident that with decreasing pore size (while keeping the ZnO tetrapod loading constant) and increasing permeation temperature, the size and concentration of water

droplets is successively decreased. Furthermore, the permeated viscous oil fractions are free of sediment particles. The water content deduced from Dean—Stark's distillation is noted in the captions corresponding to each pair of panels. **Figure A.4** shows the top and bottom surfaces of the membrane indicating the selective permeation of viscous oil. The permeate and residue separated through a 180 gauge mesh at a ZnO loading of 7.0 mg/cm^2 are also pictured in **Figure A.4**. No discernible water is observed in **Figures III.3I** and **J** corresponding to permeation of viscous oil through a 500-gauge mesh with a pore size of 30 μm. The qualitiative optical microscopy observations in **Figure III.3** suggest that while larger water droplets are readily eliminated, smaller pore sizes and higher processing temperatures are required to crack emulsions in order to eliminate water entrained within oil droplets. Such water microdroplets entrained within a continuous oil phase are otherwise able to permeate the oleophilic porous architectures.

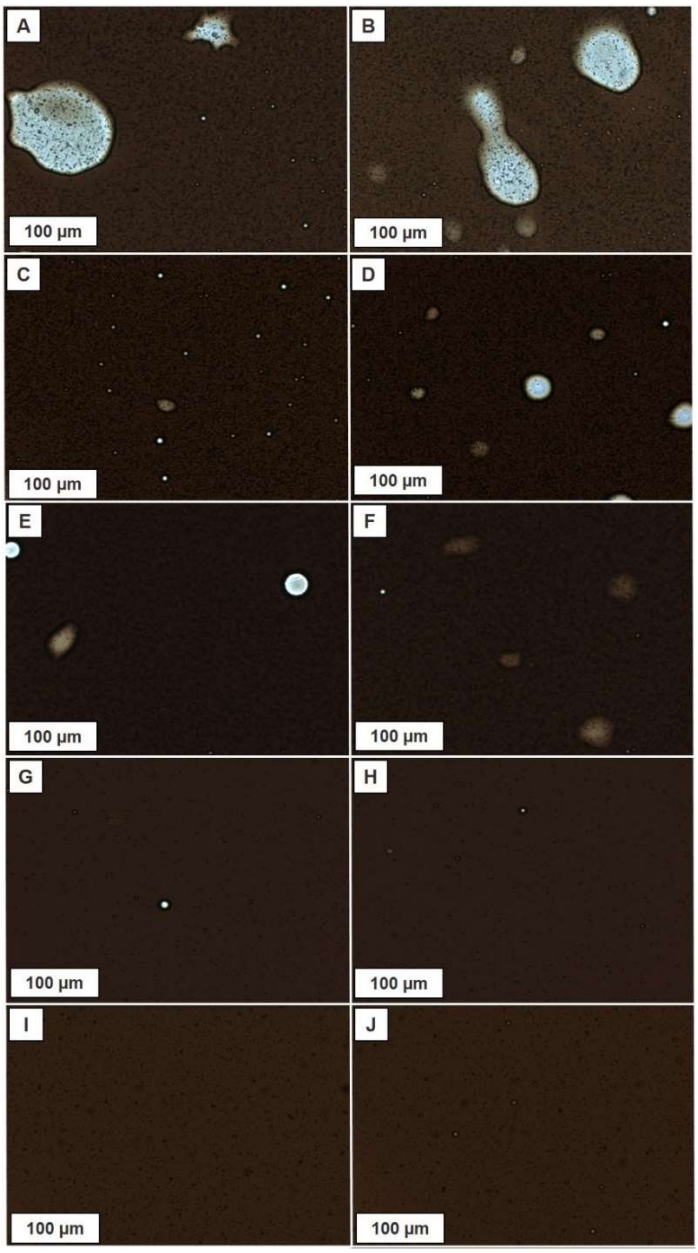

Figure III.3. Optical Microscopy Examination of SAGD Emulsions and Permeates: A,B) Optical microscopy image of a SAGD emulsion with a water content of *ca.* 30 vol.%; C,D) optical microscopy images acquired for permeate collected using a 250-gauge mesh membrane with a pore size of 61 µm loaded with 14 mg/cm^2 of ZnO tetrapods; Dean-Stark's distillation indicates that water content within this is sample is *ca.* 14 vol.%. E,F) Optical microscopy images acquired for a permeate fraction collected using a 325-gauge mesh with a pore size of 43 µm loaded with 14 mg/cm^2 of ZnO tetrapods; Dean—Stark's distillation suggests a water content of *ca.* 10 vol.% for this sample. G,H) Optical microscopy images acquired for a permeate fraction collected using a 400-gauge mesh with a pore size of 38 µm loaded with 14 mg/cm^2 of ZnO tetrapods; Dean—Stark's distillation suggests a water content of *ca.* 1 vol. %. I,J) Optical microscopy images acquired for a permeate fraction collected using a 500-gauge mesh with a pore size of 30 µm loaded with 14 mg/cm^2 of ZnO tetrapods; Karl—Fischer titration suggests a water content of *ca.* 0.69 vol. %. The lighter regions correspond to water droplets and darker solid particles are asphaltene residues and silt particles.

A more quantitative evaluation of water content is facilitated by Dean—Stark's distillation and Karl—Fischer titration. **Figures III.4** and **5** plot the evolution of the water content within the collected permeate fraction (reflecting the efficacy of separation), the permeation temperature and the flux rate as a function of the pore size and ZnO loading. For meshes characterized by larger pore sizes, 180 and 250-gauge corresponding to pore sizes of 84 μm and 61 μm respectively, **Figure III.4** shows that permeation of oil through the membrane occurs at relatively low temperatures. For instance, for a pore size of 84 μm, permeation of bitumen commences at 108°C for a ZnO tetrapod loading of 7 mg/cm^2, 113°C for a ZnO tetrapod loading of 14 mg/cm^2, 125°C for a ZnO tetrapod loading of 22.5 mg/cm^2, and 128°C for a ZnO tetrapod loading of 28 mg/cm^2. **Figure A.6** indicates that the pressure within the autoclave ranges from 15 to 28 psi at these temperatures. Membranes with larger pore dimensions and relatively low ZnO loadings, such as 180 and 250-gauge meshes with ZnO loadings of 7 mg/cm^2 permeate 18.5 vol.% and 15.7 vol.% of water, respectively. While the water content is substantially reduced from the original SAGD emulsion (30 vol.%), much of the water that is eliminated is free water; emulsified water droplets are largely permeated given the low permeation temperatures of 117°C and 127°C, respectively. Indeed, as a result of the complex nature of the emulsions, water microdroplets entrained within oil droplets permeate through the membrane if a separation is achieved at low temperatures based solely on surface tension differentials. Consequently, orthogonal wettability is a necessary but not sufficient condition for devising the efficacious separation of SAGD emulsions; it is imperative that membranes selectively permeate the viscous oil only at high temperatures (greater than 130°C) wherein the complex emulsions can be disrupted. In other words, permeation at low temperatures will inevitably yield samples with high degrees of water contamination since only free water can be separated under these conditions. Notably, the use of high temperatures is further necessary

given the operating conditions under which SAGD emulsions are extracted and handled.[9,15,33] **Figure III.4** shows that with smaller pore dimensions and increased ZnO loadings, permeation of the bituminous phase is shifted to higher temperatures, which allows for substantial reduction of water content within the permeate fractions (**Figures III.5A and B**). For a pore size of 30 μm, the water content is reduced below the limit of quantitation of Dean-Stark's distillation for ZnO loadings including and above 14 mg/cm^2 (**Figure III.5A and B**). Results from Karl-Fisher titration indicate a water content of 0.69 vol.% for the permeate recovered using a 500-gauge membrane with a pore size of 30 μm and ZnO loading of 14 mg/cm^2 (**Figure III.3I,J**). This value is well below the maximum allowed water content required for processing of viscous oil in refineries and demonstrates the viable separation of SAGD emulsions using 3D ZnO nanotetrapodal membranes.

In addition to water content as a function of pore size and ZnO loading, process temperatures above the minimum permeation temperature have also been evaluated. **Figure A.7** (Appendix A) plots the water content in the permeate for a 325-gauge stainless steel mesh with a pore size of 43 μm and a ZnO loading of 14 mg/cm^2. Permeation is initially observed at 135—140°C and the water content in the permeate is found to be *ca.* 10 vol.% by Dean-Stark's distillation. However, upon increasing the processing temperature to 150, 160, and 170°C, the water content is decreased to 3, 1.5, and 0.7 vol.%, respectively. This observation is further consistent with the need to disrupt the stabilized emulsions by operating at high temperatures in order to obtain high separation efficiencies. In other words, process temperature and membrane architecture can both be utilized to achieve the high-efficiency separation of SAGD emulsions. Operation at low temperatures will require higher ZnO loadings and meshes with smaller pore dimensions, whereas at higher temperatures lower ZnO loadings and larger pore dimensions can be used.

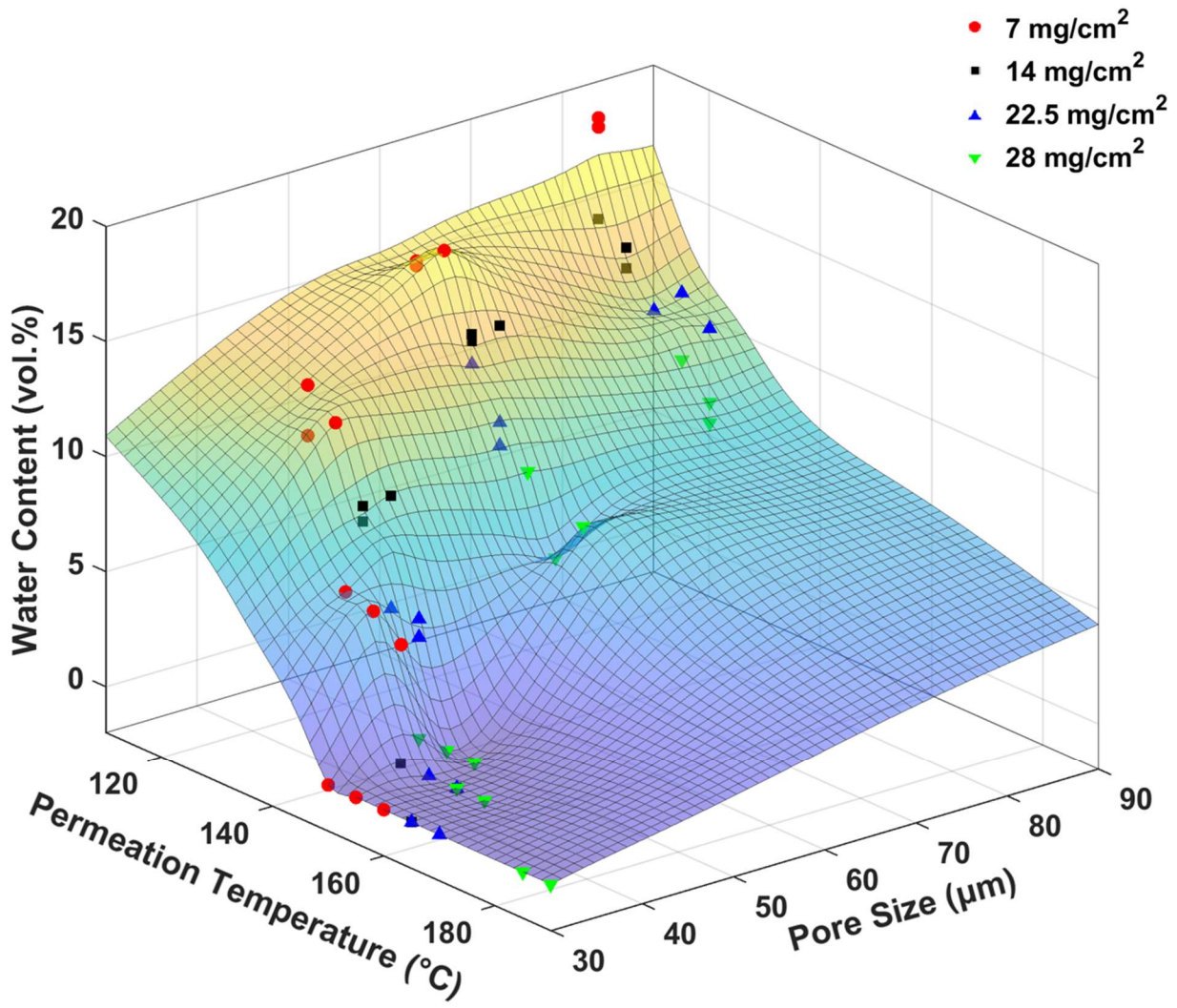

Figure III.4. Water content and permeation temperature plotted as a function of pore size for varying loadings of ZnO tetrapods with false color map overlaid for clarity.

For industrial viability, the flux rate represents an important parameter. **Figures III.5C** and **D** show that the flux rate is inversely correlated to the pore dimensions and ZnO loading, which can be rationalized based on a decrease of the effective pore diameter. For larger pore dimensions and lower ZnO loadings, the flux rate is high (reaching 20 mL/h) despite the relatively low permeation temperatures. In contrast, the flux rate is diminished for smaller pore dimensions and

higher ZnO loadings. Consequently, while smaller pore dimensions and higher ZnO loadings engender very high efficacies of separation in a single pass, the flux rates are low. The design of an effective separation system will therefore involve either the utilization of the mesh substrates within a concentric large-surface-area system and/or utilization of multiple-pass filtration steps that provide a reasonable combination of separation efficacy and flux rate at each step.

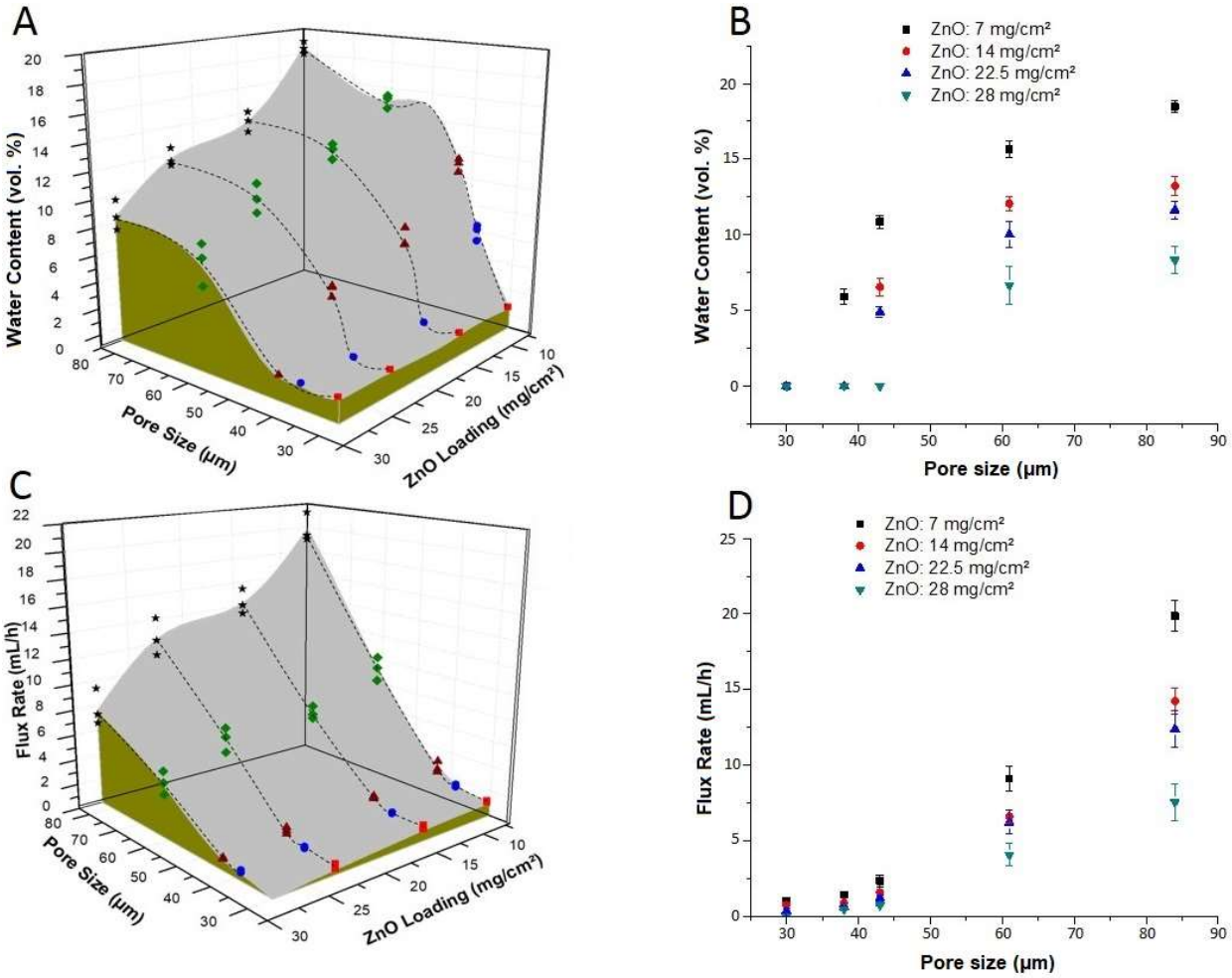

Figure III.5. (A) 3D plot depicting the variation of the flux rate as a function of the pore size and the ZnO loading within the membrane architecture. (B) Plot of the flux rate as a function of the pore size at different ZnO loadings. (C) 3D plot depicting the variation of the water content as a function of the pore size and ZnO loading on the membrane. (D) Plot of the water content as a function of the pore size at different ZnO loadings.

III.4. Conclusions

Heavy oil emulsions extracted using the SAGD process can be difficult to separate owing to their complex structure and high concentration of entrained emulsified droplets stabilized by endogeneous surfactants. An entirely inorganic thermally robust and mechanically resilient 3D membrane architecture has been developed for the separation of viscous oil and water from SAGD emulsions under the high-temperature and high-pressure conditions characteristic of the SAGD process. The membrane architecture is based on the integration of ZnO tetrapods on stainless steel mesh substrates with amorphous SiO_2 serving as an adhesive layer. The texturation derived from the micron-scale features of the meshes and the micron- as well nanoscale geometry of the ZnO tetrapods yields a porous architecture that is superhydrophobic but superoleophilic. As such, the membrane allows for permeation of the viscous oil component of SAGD emulsions while retaining water and silt. The water content in the permeate bituminous fraction has been reduced down to as low as 0.69 vol.%, well below the maximum allowable water content for processing of crude oil in refineries while further eliminating silt particles. The separation efficiency and flux rate can be tuned by adjusting the processing temperature and the membrane geometry (pore dimensions and ZnO loading). The membranes allow for operation at temperatures in excess of 130°C required to thermally disrupt stable emulsions. The facile fabrication process, mechanical and thermal robustness, and high separation efficiency paves the way for applications at scale.

III.5 References

(1) U.S. Energy Information Administration. International Energy Statistics http://www.eia.gov/cfapps/ipdbproject/iedindex3.cfm?tid=90&pid=44&aid=8. (accessed

Jan 8, 2018)

(2) Shah, A.; Fishwick, R.; Wood, J.; Leeke, G.; Rigby, S.; Greaves, M. *Energy Environ. Sci.* **2010**, *3* (6), 700–714.

(3) Alberta Energy Regulator. *Alberta's Energy Reserv. 2014 Supply/Demand Outlook* **2015**, p 299.

(4) Guo, K.; Li, H.; Yu, Z. *Fuel* **2016**, *185*, 886–902.

(5) Druetta, P.; Yue, J.; Tesi, P.; Persis, C. De; Picchioni, F. *Appl. Math. Model.* **2017**, *47*, 141–159.

(6) Ronald E. Terry. *Encycl. Phys. Sci. Technol.* **2001**, *18*, 503–518.

(7) Butler, R.; Stephens, D. *J. Can. Pet. Technol.* **1981**, *20* (2), 90–96.

(8) Butler, R. *Oil & Gas Journal*. **2001**, *99* (20), 74.

(9) Dusseault, M. B.; ShafieiI, A. In *Ullmann's Encylopedia of Industrial Chemistry*; 2011; Vol. 25, pp 263–314. DOI: 10.1002/14356007.a26_129.pub2.

(10) Shafiei, A.; Zendehboudi, S.; Dusseault, M.; Chatzis, I. *Ind. Eng. Chem. Res.* **2013**, *52* (23), 7993–8008.

(11) Wang, D.; Lin, M.; Dong, Z.; Li, L.; Jin, S.; Pan, D.; Yang, Z. *Energy and Fuels* **2016**, *30* (3), 1947–1957.

(12) Razi, M.; Sinha, S.; Waghmare, P. R.; Das, S.; Thundat, T. *Energy & Fuels* **2016**, *30* (12), 10714–10720.

(13) Kokal, S. *SPE Prod. Facil.* **2005**, *20* (1), 5–13.

(14) Razi, M.; Rahimpour, M. R.; Jahanmiri, A.; Azad, F. *J. Chem. Eng. Data* **2011**, *56* (6), 2936–2945.

(15) Al-Bahlani, A.-M.; Babadagli, T. *J. Pet. Sci. Eng.* **2009**, *68* (3–4), 135–150.

(16) Cheryan, M.; Rajagopalan, N. *J. Memb. Sci.* **1998**, *151* (1), 13–28.

(17) Zhang, W.; Liu, N.; Cao, Y.; Lin, X.; Liu, Y.; Feng, L. *Adv. Mater. Interfaces* **2017**, *4*, 1700029.

(18) O'Loughlin, T. E.; Martens, S.; Ren, S. R.; McKay, P.; Banerjee, S. *Adv. Eng. Mater.* **2017**, *19* (5), 1600808.

(19) Quéré, D. *Annu. Rev. Mater. Res.* **2008**, *38* (1), 71–99.

(20) Shirtcliffe, N. J.; McHale, G.; Atherton, S.; Newton, M. I. *Adv. Colloid Interface Sci.* **2010**, *161* (1–2), 124–138.

(21) Velázquez, J. M.; Gaikwad, A. V.; Rout, T. K.; Baier, R. E.; Furlani, E. S.; Banerjee, S. *J. Mater. Chem.* **2012**, *22* (8), 3335–3339.

(22) Roach, P.; Shirtcliffe, N. J.; Newton, M. I. *Soft Matter* **2008**, *4* (2), 224.

(23) Drelich, J.; Chibowski, E. *Langmuir* **2010**, *26* (24), 18621–18623.

(24) Lee, J. A.; McCarthy, T. J. *Macromolecules* **2007**, *40* (11), 3965–3969.

(25) Velazquez, J. M.; Baskaran, S.; Gaikwad, A. V; Ngo-Duc, T.-T.; He, X.; Oye, M. M.; Meyyappan, M.; Rout, T. K.; Fu, J. Y.; Banerjee, S. *ACS Appl. Mater. Interfaces* **2013**, *5*, 10650–10657.

(26) O'Loughlin, T. E.; Dennis, R. V.; Fleer, N. A.; Alivio, T. E. G.; Ruus, S.; Wood, J.; Gupta, S.; Banerjee, S. *Energy & Fuels* **2017**, *31* (9), 9337-9344.

(27) O'Loughlin, T. E.; Waetzig, G. R.; Davidson, R. E.; Dennis, R. V.; Banerjee, S. *Encycl. Inorg. Bioinorg. Chem.* **2017**, p 1, DOI: 10.1002/9781119951438.eibc2493.

(28) Stöber, W.; Fink, A.; Bohn, E. *J. Colloid Interface Sci.* **1968**, *26* (1), 62–69.

(29) Waetzig, G. R.; Cho, J.; Lacroix, M.; Banerjee, S. *Sci. Rep.* **2017**, *7* (1), 1–13.

(30) Mishra, Y. K.; Adelung, R. *Mater. Today* **2017**, 10.1016/j.mattod.2017.11.003.

(31) Gröttrup, J.; Schütt, F.; Smazna, D.; Lupan, O.; Adelung, R.; Mishra, Y. K. *Ceram. Int.* **2017**, *43* (17), 14915–14922.

(32) Destino, J. F.; Kraut, N. D.; Hargrave, L. E.; Bright, F. V. *Mater. Lett.* **2016**, *181*, 47–51.

(33) Albahlani, A. M.; Babadagli, T. In *A Critical Review of the Status of SAGD: Where Are We and What is Next?*, SPE Western Regional and Pacific Section AAPG Joint Meeting, Bakersfield, California, USA, March 29-April 4, 2008; Society of Petroleum Engineers: Richardson, Texas, USA, 2008.

CHAPTER IV

MODIFYING BASE METAL SUBSTRATES TO EXHIBIT UNIVERSAL NON-WETTABILITY: EMULATING BIOLOGY AND GOING FURTHER[*]

IV.1 Introduction

In Chapters I—III, the design of surfaces that permeate oil but repel water was discussed based on the fundamental principle that the two liquids have drastically different surface tensions, which is further amplified with mesoscale texturation to amplify the inherent wettability of the liquids. However, in order to design a surface that doesn't wet either oil or water requires additional considerations such as balancing the cohesive forces of the droplets against the adhesive forces of the solid—liquid interface. This is substantially more difficult with oil, since hydrocarbons have relatively weak intermolecular forces compared to that of water and consequently exhibit a greater predilection for spreading on surfaces. Again, we note that nature provides a plethora of examples of hydrophobic surfaces but struggles to provide examples of oleophobic surfaces. One example of a hydrophobic natural response is the common fire ant, as demonstrated in Figure IV.1. The digital photograph indicates that an individual ant has some hydrophobic behavior, and even forms a plastron upon submersion in water (Figure IV.1D). However, when the ants are assembled in interconnected formations, such assemblies can repel large water droplets and even form a larger interconnected plastron network as seen in Figure IV.1E.

In this chapter, we discuss the design of plastrons embedded onto highly corroded surfaces wherein pitting corrosion is used as a means of inducing surface texturation. Similarly, in

---

[*] Reproduced with permission from "Modifying Base Metal Substrates to Exhibit Universal Non-Wettability: Emulating Biology and Going Further." O'Loughlin, T.E.; Waetzig, G. R.; Davidson, R. E.; Dennis, R. V.; Banerjee, S. *Encycl. Inorg. Bioinorg. Chem.* **2017**, p.1. Reproduced by permission of John Wiley & Sons, Inc.

Chapter V we explore the biomimetic use of ZnO nanotetrapods which are arrayed in great numbers on a stainless steel mesh to generate an analogous plastron network. This is further aided by functionalization to constitute a self-assembled monolayer of a perfluorinated phosphonic acid to tune the surface energy, which reduces interactions at the solid—liquid interface and allows the relatively weaker intermolecular forces of the oil to dominate and preclude its ability to spread across the surface. In doing so, the surfaces can now repel both oil and water, allowing for efficacious gliding of both liquids.

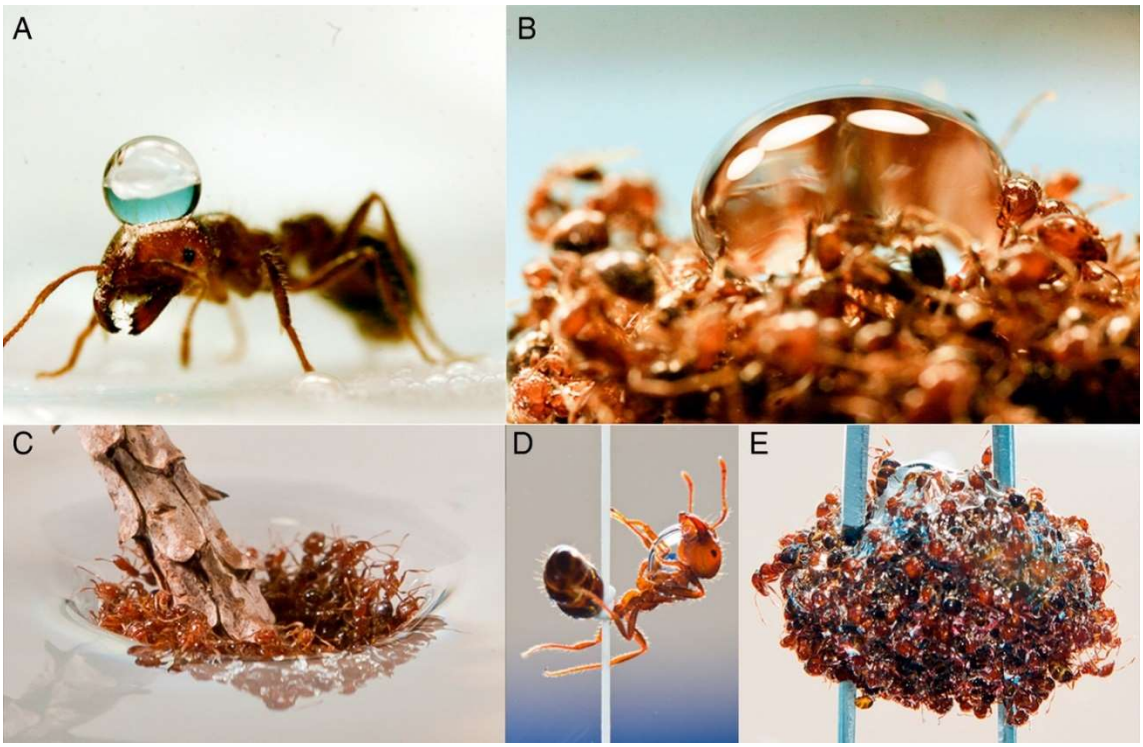

Figure IV.1. Water repellency of ant rafts. (A) An individual ant's exoskeleton is moderately hydrophobic, as shown by the contact angle of the water drop. (B) Enhanced water repellency of a raft of ants, as shown by the increased contact angle of the water drop. (C) Buoyancy and elasticity of the ant raft, as shown by attempted submersion by a twig. (D) The plastron air bubble of an ant in soap-free water. The bubble makes the ant buoyant, necessitating the use of a thread to hold it underwater. (E) An air pocket trapped in a submerged ant raft. The shimmery layer around the ants is the air–water interface. Reproduced with permission from Mlot, N. J.; Tovey, C. A; Hu, D. L. *Proc. Natl. Acad. Sci. U. S. A.* 2011, *108* (19), 7669–7673.

The design and fabrication of surfaces that are not wetted either by water or oil holds much significance for the energy infrastructure, particularly where corrosion represents a significant problem and cleaning, maintenance, and repair of containers, pipelines, and processing equipment is difficult or poses safety hazards. Nature has numerous examples of surfaces that resist fouling by repelling liquid (especially water) droplets. Designing a surface that is not wetted by low-surface-tension liquids such as hydrocarbons is a considerably more difficult task that is beyond the capabilities of most natural systems since the cohesive forces within such liquids are low and most interfacial interactions stabilize the spreading of oil droplets. A combination of hierarchical texturation, reentrant curvature, and low surface energy is thought to be necessary to design omniphobic surfaces. However, such surfaces are often constructed from polymers and thus prone to thermal degradation. In this contribution, we illustrate the modular design and development of a biomimetic architecture incorporating micro- and nanoscale texturation on etched carbon steel.

Etching of the steel substrate endows microscale roughness; the substrate is further coated with ZnO nanotetrapods to define nanoscale texturation and modified to expose pendant fluorous groups that exhibit both superhydrophobic and superoleophobic behavior for both water and oil (including crude oil) droplets. The utilization of ZnO nanotetrapods with protruding arms gives rise to a nanotextured morphology regardless of the specific orientation of the nanostructures and allows for the trapping of air pockets, thereby suspending liquid droplets as per the Cassie—Baxter non-wetting mode. The textured ceramic/metal surfaces are stable up to high temperatures and are well adhered to the metal substrate upon application of a conformal amorphous SiO_2 coating. The incorporation of multiple design elements: microscale roughness, nanotexturation, a “cementing” layer, and surface modification with low energy pendant

perfluorinated chains provides considerable versatility and tunability for specific liquid-handling conditions. The strategy described here is generalizable to other modes of texturation and surface modification and can be broadly adapted to prevent wettability of a surface by a specific liquid, thereby providing an approach for protecting components exposed to corrosive fluid environments.

IV.2 Experimental

IV.2.1 Steel Substrates and Etching Conditions

Flat sheets of low carbon steel (type A36, 9.1 mm in thickness, The Metal Store®, Maple Heights, OH, USA) were cut to the desired dimensions and were thoroughly cleaned by successively washing with hexanes (98.5% millipore), ethanol (99.5+%, Koptec), Alconox® soap solution, and deionized water (ρ = 18.2 MΩ/cm). Three different etching routes were attempted in order to define microscale topographies. In the first method, the substrates were immersed in a 1:1 (*v*/*v*) solution of 12.1 M HCl and deionized water and solid hexamethyelenetetramine was added to obtain a concentration of 24.9 mM. The substrate was etched at 25—80°C for 10—60 min. In the second method, the A36 substrates were immersed in equal parts of 12.1 M HCl and deionized water (by volume). The solution was then heated to 80°C for 10—60 min. In addition, for select substrates a mixed acid solution containing H_2SO_4:HCl:H_2O in a 12%:38%:50% (*v*/*v*/*v*) ratio, using 18.0 M H_2SO_4 and 12.1 M HCl, was also used to etch the substrates. The mixed acid solution was first heated to 93°C before immersing samples for 30—90 s. The samples were rinsed with copious amounts of water after extraction from the acid baths prior to application of ZnO nanotetrapods or surface modification with perfluorinated groups.

IV.2.2 Synthesis of ZnO Nanotetrapods

In order to facilitate the rapid generation of ZnO tetrapods, a previously reported method of using Zn coated steel was adapted for Chapter IV as schematically depicted in Figure IV.2.[1] In this process, Zn metal sheets of 0.25 mm thickness (99% purity, McMaster-Carr) were cut into ca. 3 mm x 3 mm pieces and placed onto a 316 stainless steel mesh (McMaster-Carr) and inserted into a 1" quartz tube. The quartz tube was then placed within a tube furnace (Lindburg/BlueM). The assembly was heated at a rate of 43°C/min to a maximum temperature of 950°C and dwelled at that temperature for 1 min. A crackling sound was observed along with a red glow and a fluffy white residue was collected from the walls of the quartz tube after allowing the furnace to cool to room temperature. The tetrapods were dispersed in 2-propanol (99.9%, Fisher Scientific) at a concentration of 20 mg/mL by ultrasonication.

IV.2.3 Coating of ZnO Nanotetrapods onto Steel Substrate

The ZnO nanotetrapod dispersion in 2-propanol was spray coated onto the etched A36 carbon steel substrates using a Master airbrush with a nozzle diameter of 0.5 mm with the help of an air compressor at an output pressure of 45 psi. The final coated substrates had ZnO loadings ranging from ca. 3.5 to 7.8 mg/cm^2. The substrates were held at a temperature of ca. 120°C during the coating process to facilitate removal of the solvent.

In order to increase adhesion and mechanical resilience of the ZnO nanotetrapod coatings, a SiO_2 layer was constituted using a modified Stöber method.[2] In order to constitute an amorphous SiO_2 shell, tetraethylorthosilicate (TEOS) was used as the precursor and applied from a solution containing 80 vol.% ethanol, 18.5 vol.% deionized water (ρ = 18.2 MΩ/cm), 1 vol.% of 28—30% aqueous solution of NH_4OH, and 0.5 vol.% TEOS (99.999+% metals basis, Alfa Aesar).

The substrates were held at a temperature of 120°C during the spray deposition of the TEOS samples; this temperature facilitates the formation of the siloxane framework. The final loading of TEOS used within the overlayer coatings was optimized to be ca. 3.9 μL/cm^2.

2.4. Surface Modification: To decrease the surface energy (and thus increase the hydrophobicity and oleophobicity) of the acid-etched steel sheets and ZnO-nanotetrapod-coated surfaces, the substrates were functionalized with perfluorinated silanes and phosphonic acid. In order to perform this surface modification, 2.7 mM solutions of the desired fluorinated compounds were prepared by combining 400 μL of ammonium hydroxide (28-30%), 400 μL of deionized water (ρ = 18.2 MΩ/cm), and the appropriate mass of the fluorinated precursor. The mixture was then diluted to 20 mL using 1-butanol (99%, Alfa Aesar). The silanes, heptadecafluoro-1,1,2,2-tetrahydrodecyl)trimethoxysilane, nonafluorohexlytriethoxysilane, and triethoxyfluorosilane were purchased from Gelest Inc. and used without further purification, whereas 1H,1H,2H,2H-perfluorooctanephosphonic acid was purchased from Sigma-Aldrich and perfluorooctane was purchased by Alfa Aesar. The substrates were immersed in *n*-butanol solutions of the fluorinated silanes for 1 h, rinsed with butanol to remove physisorbed silanes, and then allowed to dry before testing. The perfluorinated silanes were selected for more detailed studies of the SiO_2 adhered samples given their compatibility with the siloxane framework, whereas perfluorinated phosphonic acid was used as the modifier of choice to functionalize the surfaces of ZnO nanotetrapods.

IV.2.4 Characterization of Etched Metal Surfaces

The acid etched surfaces were evaluated by optical microscopy using a BX41 Olympus light microscope. The pitting corrosion was further evaluated using a JEOL JSM-7500F field emission

scanning electron microscope (FE-SEM) equipped with a high brightness conical field-emission gun, and a low-aberration conical objective lens. An accelerating voltage of 5—10 keV was used to image the nanostructures.

IV.2.5 Characterization of ZnO Nanotetrapods

In order to evaluate the morphology of the ZnO tetrapods, scanning electron microscopy images were obtained utilizing a JEOL JSM-7500F FE-SEM. An accelerating voltage of 2—5 keV was used to image the nanostructures. Energy dispersive X-ray mapping analysis was conducted using an Oxford EDX system on the same instrument but using an accelerating voltage of 10 keV and an emission current of 10 μA. X-ray diffraction was performed using a Bruker-AXS D8 Vario X-ray powder diffractometer with Cu Kα radiation (λ = 1.5418 Å). Raman spectroscopy measurements were acquired utilizing 514.5 nm laser excitation from an Ar-ion laser using a Jobin-Yvon Horiba Labram HR instrument and an integrated Olympus microscope. Fourier transform infrared (FTIR) analysis was performed using a Bruker Vertex 70 instrument.

IV.2.6 Contact Angle Measurements

All contact angles were measured using a CAM 200 Optical Goniometer. For all experiments, a drop size of 10 μL was used to apply the test liquids. A mechanical pipette was used to apply deionized water (ρ = 18.2 MΩ/cm); whereas hexadecane (99% Sigma-Aldrich) and heavy oil (Cenovus Energy Inc., Calgary, Canada) were applied using a manual micropipette. All contact angles and standard deviations shown are a result of at least three replicates.

IV.2.7 Adhesion Testing

The surface-modified ZnO nanotetrapods films embedded onto A36 low carbon steel were evaluated for their strength of adhesion using American Society for Testing of Materials (ASTM) standardized tests. Adhesion testing of the samples was performed by following ASTM tests D3359 and D2197. In test D3359, a grid was defined on the coated substrate and a tape from the ASTM kit was applied and subsequently removed. The tested area was then evaluated for the removal of coating material from the surface and classified from 0B to 5B based on the standards prescribed by the ASTM method. In ASTM D2197, successive amounts of weight were added to a standardized balanced-beam scrape adhesion apparatus while the coated sample was pulled underneath a stainless steel U-shaped loop. The weight at which the U-shaped loop continuously broke through the coating and reached the substrate was then recorded as the scrape adhesion strength or failure end point.

IV.2.8 Thermal Analysis

Thermogravimetric analysis (TGA) of the samples was performed using a Shimadzu TA-60WS thermal analyzer from 25 to 900°C at 10°C/min with a nitrogen flow rate of 50 mL/min.

IV.3 Results and Discussion

IV.3.1 Constructing an Artificial Plastron: A Process Outline for Achieving Universal Non-Wettability on Steel Surfaces

In Chapter IV, we illustrate a stepwise approach for the preparation of omniphobic surfaces directly integrated onto structural steel using a combination of microscale and nanoscale texturation and surface modification to decrease the surface energy. The steel substrate used is

A36 structural grade carbon steel, a ubiquitous low alloy structural material. Microscale texturation is derived from a mild acid etching step used to remove scale and define micron-scale surface features. Nanoscale texturation is derived from ZnO nanotetrapods that are spray coated onto the substrate[1] and adhered by a modified Stöber method wherein tetraethylorthosilicate (TEOS) is used as the precursor to constitute a conformal amorphous SiO_2 coating that adheres ZnO to the steel substrate.[2] The use of a mixed oxide crystalline-ZnO/amorphous-SiO_2 coating allows for compatibility with high-temperature operation and further lends mechanical resilience to the coating. The substrates showing the most promising non-wettability towards water droplets are further functionalized with perfluorinated molecules to endow oleophobicity. Functionalization with perfluorinated molecules allows for reduction of surface energies and renders the surface omniphobic, thereby enabling the largescale modular design of universally non-wettable surfaces that are compatible with high-temperature operation.

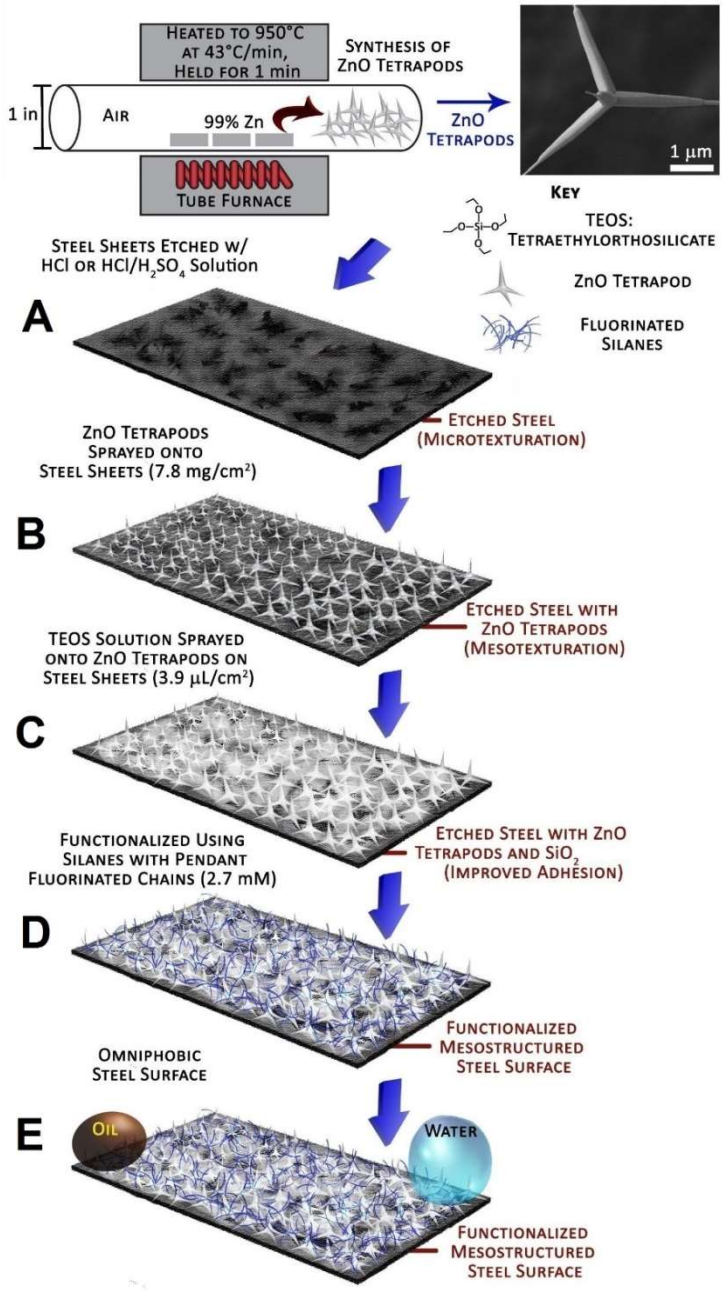

Figure IV.2. Schematic illustration of process flow used to prepare omniphobic surfaces integrated onto etched carbon steel. The top panel shows the synthesis of ZnO nanotetrapods by oxidation of Zn metal in an air environment. (a) The steel substrate is etched with acid to define microscale texturation. (b) ZnO nanotetrapods are spray-coated onto the etched carbon steel, thereby adding nanoscale texturation. (c) TEOS is subsequently spray-coated onto the ZnO/etched steel substrates to form a siloxane linkage between the etched steel and ZnO nanostructures. (d) The substrates are functionalized with perfluorinated silanes (or perfluorinated phosphonic acids). The resulting hierarchically textured surfaces trap air pockets below the tetrapods, thereby creating a plastronic architecture. (e) The textured surfaces exhibit a low surface energy by dint of the pendant fluorous phase, thereby yielding omniphobic behavior.

Figure IV.2 outlines the design of omniphobic surfaces integrated directly onto etched carbon steel substrates. The design incorporates the following elements: (a) microscale texturation defined by acid etching of flat carbon steel substrates; (b) nanoscale topography defined by ZnO nanotetrapods with protruding ends; (c) plastron-like capture of air pockets between ZnO nanotetrapods and the underlying substrate; (d) an adhesive SiO_2 layer that is optionally used to adhere nanotetrapods to steel substrates; and (e) a high-density of surface perfluorinated pendant groups.

Given the large number of process variables and potentially vast matrix of compositional possibilities, contact angle measurements have been used to rapidly screen conditions and to down-select promising candidates for further examination along the process flow depicted in Figure IV.2. Initially, water contact angles are used to modify the process flow to converge upon etching conditions and nanotetrapod loadings (in other words, micro- and nanoscale texturation) that show promising non-wettability. Subsequently, the nanotetrapod loadings and nature and extent of functionalization with perfluorinated compounds is modified and the surfaces thus prepared are challenged with water, hexadecane, and heavy oil.

IV.3.2 Microscale Texturation by Selective Etching

Micrometer-scale texturation is established by chemical etching of flat carbon steel substrates. Immersion of carbon steel within strong electrolyte solutions in an oxygen ambient results in pitting corrosion and roughening of the surface; the specific topographies and extent of roughness depends sensitively on the etching conditions. The etch patterns depend on the etchant and the specific elements that are selectively dealloyed from carbon steel as well as the reactivity along the dislocations. Three types of etch solutions have been examined: (a) an aqueous

solution of 6.05 M HCl and 24.9 mM hexamethylenetetramine at 25 and 80°C (for 10 and 60 min), as reported in ASTM G1 for the cleaning and removal of oxides from carbon steel surfaces; (b) an aqueous solution of 6.05 M HCl at 80°C (for 10 and 60 min);[3] and (c) a mixed acid solution of 4.6 M HCl and 2.2 M H_2SO_4 at 93°C (for 30—90 s).[3] The HCl and H_2SO_4 solutions etch steel along different crystallographic directions and have been used in tandem to obtain hierarchical surface morphologies.[3] **Figure IV.3** shows representative optical microscopy images of the carbon steel surfaces after etching with different solutions for different periods of time showing contours tracing steps defined on the carbon steel surfaces. The HCl/hexamethylenetetramine solution is particularly well suited to the removal of oxide scale but does not greatly roughen the surface. Indeed, optical microscopy images indicate terraces that are tens of microns wide. In contrast, the substrates etched with the mixed acid solution show much more closely spaced steps spanning only a few microns, whereas the substrates etched with HCl alone at 80°C exhibit sub-micron-scale pores in addition to steps. **Figure IV.4** contrasts SEM images acquired at different magnifications for the latter two samples as compared to cleaned A36 carbon steel substrates (Figs IV.4a and b). For the mixed acid sample etched at 93°C for 45 s (Figs. IV.4c and d), large terraces are observed spaced by 500 nm—1 μm suggesting distinctive microscale texturation. In contrast, for the HCl-etched sample prepared at 80°C for 1 h (Figs. IV.4e and f), nanometer sized porosity is evidenced in proximity of deeper etch pits.

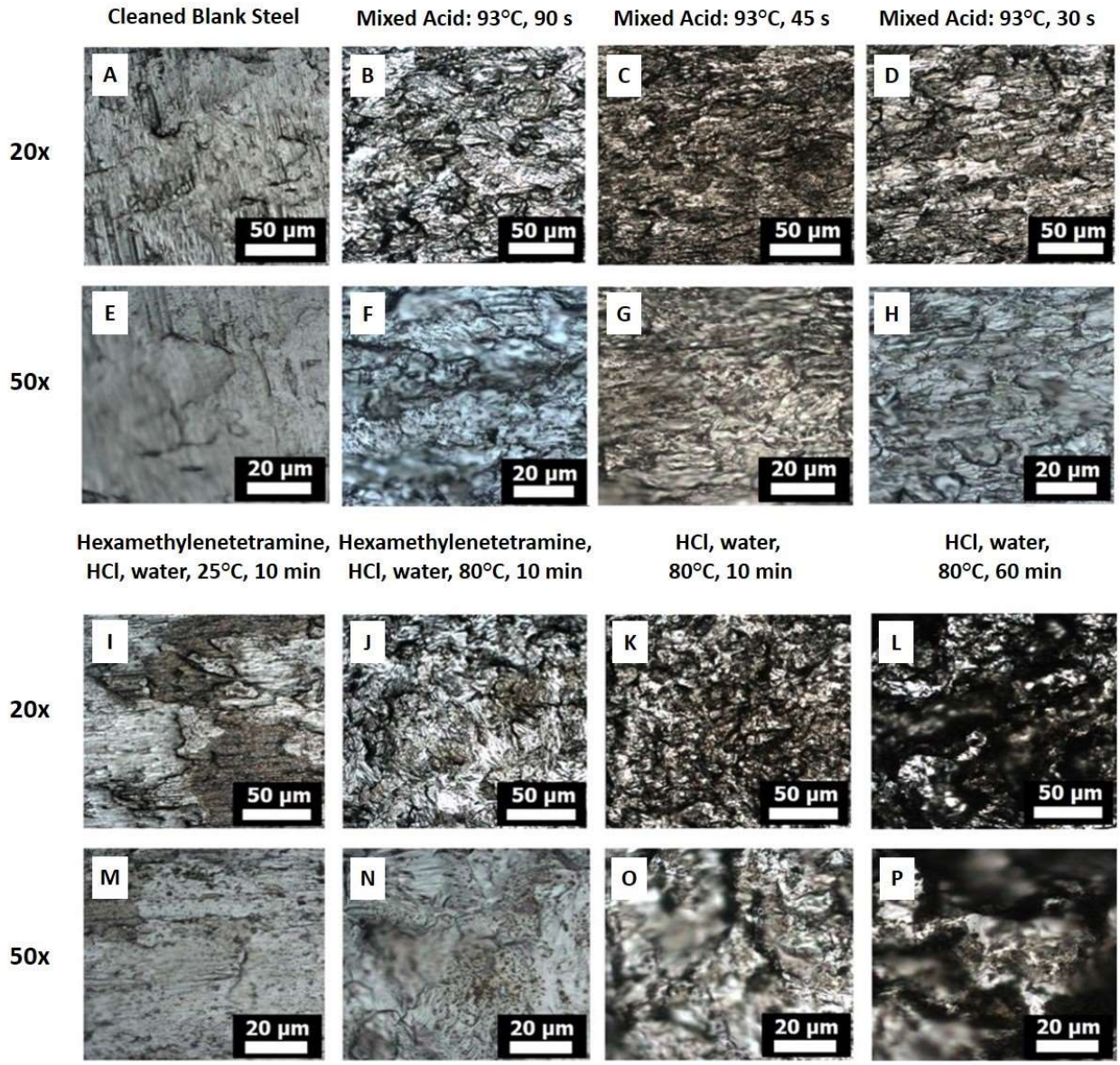

Figure IV.3. Optical micrographs obtained at 20× and 50× magnifications indicating the surface topographies of roughened carbon steel surfaces upon chemical etching. The specific etching solutions used are indicated in the figure.

The efficacy of the etch solutions in defining texturation have been assessed by measuring water contact angles before and after functionalization with a perfluorinated silane (a 2.7 mM solution of heptadecafluoro-1,1,2,2-tetrahydrodecyl)trimethoxysiloxane) as noted in **Table 1** and

illustrated in **Figures IV.5 and 6**. As suggested in Chapter I by Equation I.3, roughness amplifies the intrinsic wettability of the surface. A freshly cleaned steel substrate is fairly hydrophilic with a water contact angle of 63° ± 3°. Etching with a solution of HCl, hexamethylenetetramine, and water at 25°C for 10 min yields topographies illustrated in Figure IV.3I and actually increases the contact angle to 80° ± 5°, suggesting a smoother surface as a result of removal of passivating oxide layers, which yields a smoother surface that better reflects the mildly hydrophilic nature of the carbon steel. In contrast, etching with the same solution at 80°C for 10 min decreases the water contact angle to 26° ± 3°. The much lower contact angle upon etching at 80°C is a result of somewhat increased texturation of the surface as observed in Figures IV.3K. Etching the carbon steel substrates in a 1:1 HCl:H_2O solution at 80°C for 10 min induces a comparable degree of texturation and also decreases the contact angle to 27° ± 8°. When this same etching solution is used for an extended time of 1 h, the water contact angle decreases to 10° ± 1° indicating a high degree of surface roughness (Fig. IV.3L). In comparison, the mixed acid etchant deployed at 93°C for only 45 s decreases the contact angle to 40° ± 8° (Fig. IV.5). When comparing the mixed acid etch at shorter and longer times of 30 and 90 s, the water contact angle decreases to <10° and 14° ± 3°, respectively. The decrease of contact angle for these substrates with increasing roughness is consistent with the amplification of intrinsic wettability predicted in Chapter I by Equation I.3. The lower contact angle for the more extensively etched samples (mixed acid for 90 s or HCl etch for 60 min) suggests a higher degree of nanoscale texturation (and thus a higher *r* value as noted in Chapter I, Eq. 3), which is consistent with the deeper etch pits and nanoscale surface porosity discernible in Figure IV.4 for these samples.

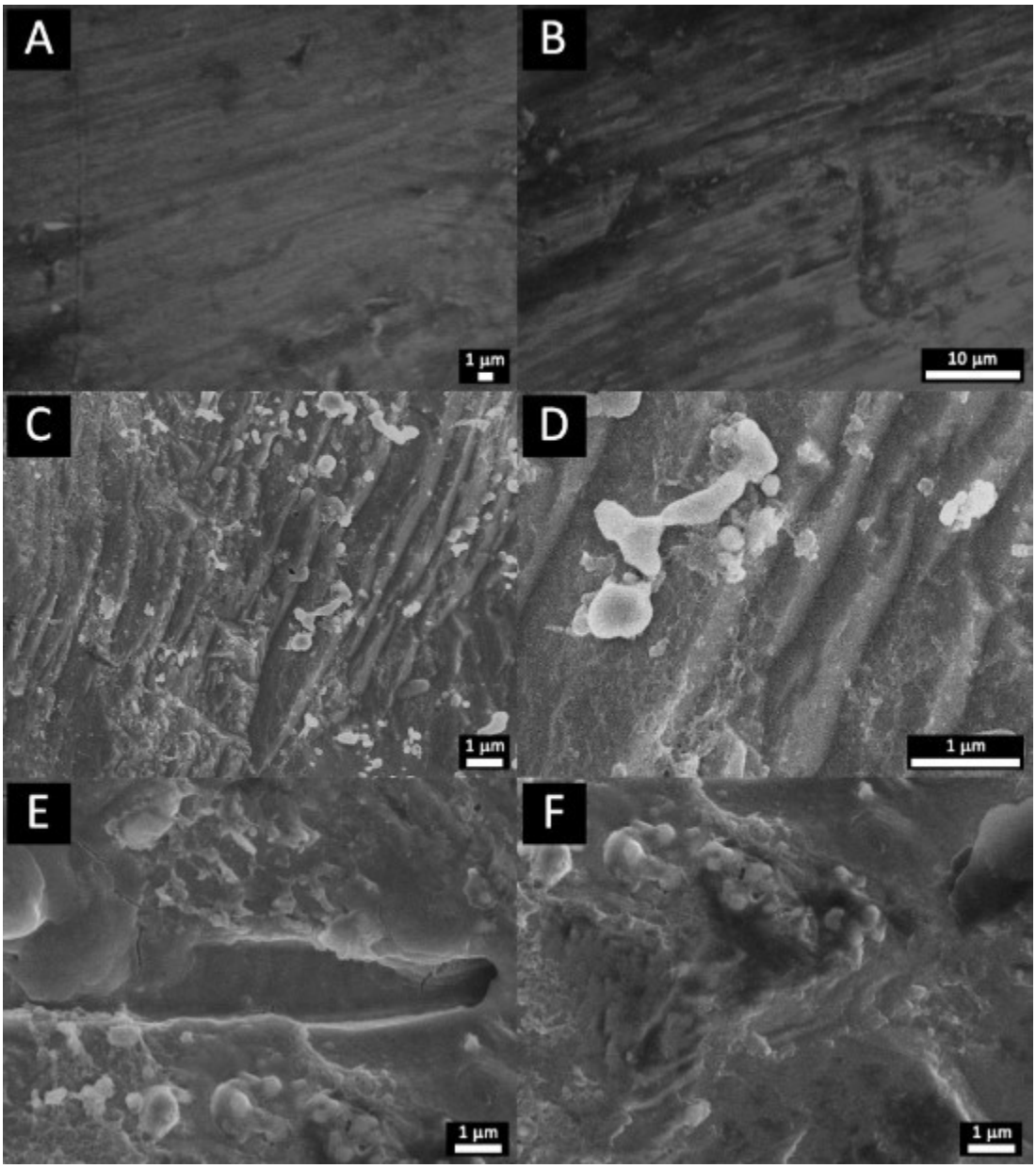

Figure IV.4. SEM images of etched carbon steel surfaces. (A,B) SEM images of cleaned A36 carbon steel substrates. (C,D) SEM images of A36 carbon steel substrates upon etching with a mixed acid solution at 93°C for 45 s. Clear terraces are evident, separated by distances of 500nm to 1 µm. However, the steps are generally free of nanoscale topographies. (E,F) SEM images of A36 carbon steel substrates etched using an HCl solution at 80 °C for 1 h, depicting deeper etch pits with accompanying nanoscale porosity.

Next, we have sought to examine the extent to which such textured surfaces are rendered hydrophobic when the surface is modified to present pendant fluorinated groups. The lower row of contact angle measurements shown in Figures IV.5 and 6 indicate that after functionalization with a perfluorinated silane, the water contact angle of clean steel has been increased to 114° ± 3° suggesting that the pendant perfluorinated groups have rendered the surface hydrophobic. Again, as predicted by in Chapter I Equation I.3, the texturation induced by etching amplifies this intrinsic non-wettability of the (now) low-surface-energy substrate. The steel sample etched with a solution of HCl, hexamethylenetetramine, and water at 25°C for 10 min provides a water contact angle of 115° ± 2° after surface modification again suggesting that this set of etching conditions does not induce substantial texturation of the surface.

Table IV.1 Water contact angles for carbon steel substrates subjected to different etching conditions to define micro- and nanoscale texturation. Contact angles are listed for freshly etched samples. Water contact angles were acquired in triplicate for each sample and are presented as the mean and the standard deviation.

Etching Agent	Time	Fluorinated Silane	CA Water
None	None	None	63° ± 3°
HCl/HMT 25 °C	10 min	None	80° ± 5°
HCl/HMT 25 °C	60 min	None	41° ± 4°
HCl/HMT 80 °C	10 min	None	26° ± 3°
HCl/HMT 80 °C	60 min	None	15° ± 5°
Mixed acid	30 s	None	<10°
Mixed acid	45 s	None	40° ± 8°
Mixed acid	90 s	None	14° ± 3
HCl	10 min	None	27° ± 8°
HCl	60 min	None	<10°

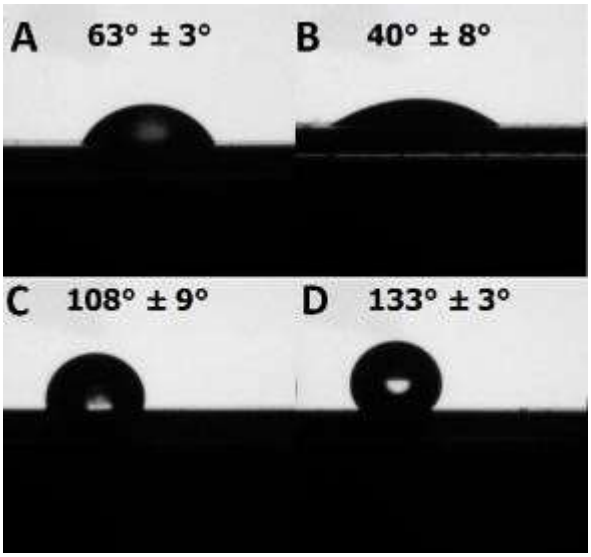

Figure IV.5. Water contact angles of (A) cleaned blank steel, (B) steel after etching with mixed acid solution at 93°C for 45 s. (C) and (D) represent the water contact angles measured for (A) and (B) after immersion in a 2.7 mM butanol solution of nonafluorohexlytriethoxysilane, respectively.

When the temperature of this etching solution is increased to 80°C for 10 min the contact angle is modestly increased to 118° ± 1° showing that as compared to the texturation of the cleaned blank steel, this etchant does not substantially add any additional texturation. These values are a good representation of the surface energy of a relatively planar carbon steel surface capped with the perfluorinated silane.

For the samples etched with a 1:1 HCl:H_2O solution for 10 min at 80°C and then modified with the perfluorinated silane, the water contact angle is slightly increased to 120° ± 3°; in contrast, just a 30 s etch with mixed acid solution at 93°C yields a contact angle of 133° ± 5° after surface functionalization. Surfaces etched by a 1:1 HCl:H_2O solution at 80°C for 1 h and with a mixed acid solution at 93°C for 45 s that show much more extensive texturation exhibit water contact angle values of 151° ± 4° and 143° ± 6°, respectively, after surface modification with the

fluorinated silane. The two most optimal etching conditions, 1:1 HCl:H_2O solution for 60 min at 80°C and mixed acid solution at 93°C for 45 s, have been selected for further enhancement of non-wettability based on the addition of ZnO nanotetrapods and surface modifiers as described in subsequent sections of Chapter IV.

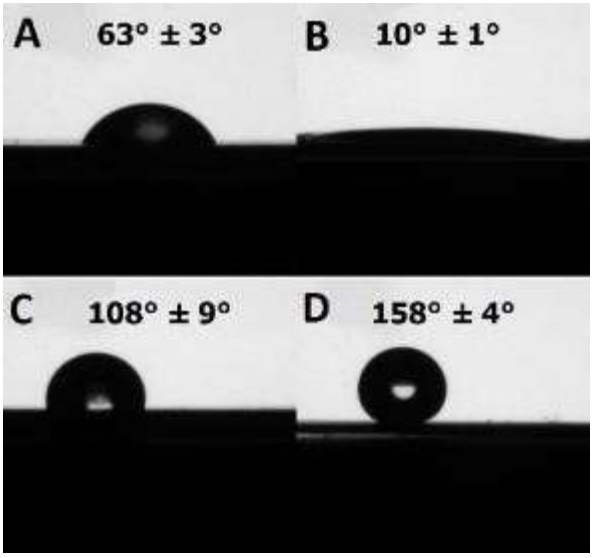

Figure IV.6. Water contact angles of (A) cleaned blank steel, (B) steel after etching in HCl solution at 80°C for 1 h. (C) and (D) represent the water contact angles measured for (A) and (B) after immersion in a 2.7 mM butanol solution of nonafluorohexlytriethoxysilane, respectively.

IV.3.3 Nanoscale Texturation Using ZnO Nanotetrapods

The air oxidation of metallic zinc at high temperatures yields ZnO nanostructures with starkly different morphologies as illustrated in **Figure IV.7** depending on the partial pressure of oxygen. Nanowire arrays, nanotubes, nanocombs, and nanotetrapods are obtained depending on the oxygen partial pressure, which likely mediates the extent of supersaturation of monomeric vaporized Zn species.[1,4,5] The growth of nanowires as well as the 1D elements of the other nanostructures is likely mediated by growth along screw-dislocations;[1,6,7] the wires and tetrapods

alike taper to a sharp point as the monomer is depleted during the course of the reaction. The nanotetrapods have been selected to endow nanoscale texturation to the etched substrates discussed in the preceding section. The tetrapodal nanostructures are accessible by a readily scalable open-air oxidation approach and upon deposition onto the substrates will always expose one or more protruding ends facilitating the entrapment of air bubbles and suspension of liquid droplets in the Cassie—Baxter state.

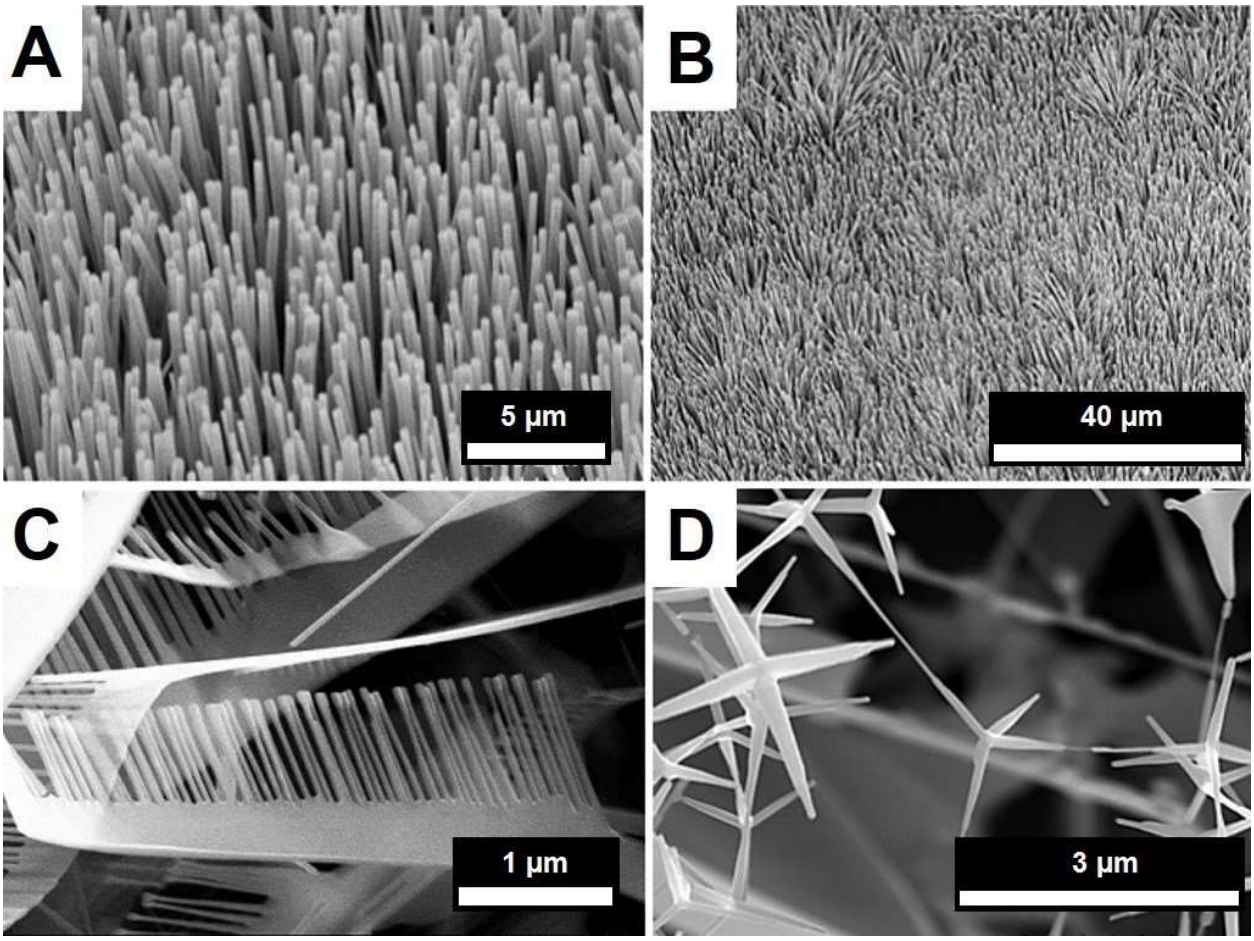

Figure IV.7. SEM images of different ZnO morphologies obtained from oxidation of metallic Zn at different oxygen partial pressures.[48] A,B) nanowire arrays, C) nanocombs, and D) nanotetrapods. Adapted with permission from *ACS Applied Materials & Interfaces* **2013**, *5*, 10650-10657. Reproduced by permission of the American Chemical Society.

Figures IV.8A and **B** shows two different orientations of individual ZnO nanotetrapods, whereas Figures IV.78 and D depict low and high-magnification views of ZnO nanotetrapods integrated onto etched steel substrates. The Raman spectrum acquired for harvested ZnO powders depicted in Figure IV.8E is consistent with stabilization of hexagonal ZnO and the symmetry assignments of the phonon modes are indicated in the figure.[1,8] The XRD pattern of the ZnO tetrapods shown in Figure IV.8D can be indexed to Joint Committee on Powder Diffraction Standards (JCPDS) # 36-1451, indicating the formation of phase-pure ZnO in the hexagonal zincite phase.

While a few tetrapodal arms are broken during harvesting and spray coating, the structures nevertheless define a continuous nanoscale topography on the etched steel substrates as a result of their protruding arms. The nanotetrapods are an essential design element for the preparation of non-wettable surface and offer the following distinct advantages: (i) the tetrapod morphology with protruding arms gives rise to a nanotextured morphology regardless of the specific orientation of the nanostructures, which is much more advantageous as compared to nanowire arrays that can potentially buckle and flatten under an applied stress; (ii) the tetrapod morphology is impossible to close pack and thus nanotetrapods yield nanoscale porosity as evidenced in Figures IV.8C and D. Such porosity enables the nanotetrapods to define a “bed of nails” geometry enabling classical Cassie—Baxter or plastron-like behavior by trapping air beneath suspended water or oil droplets.

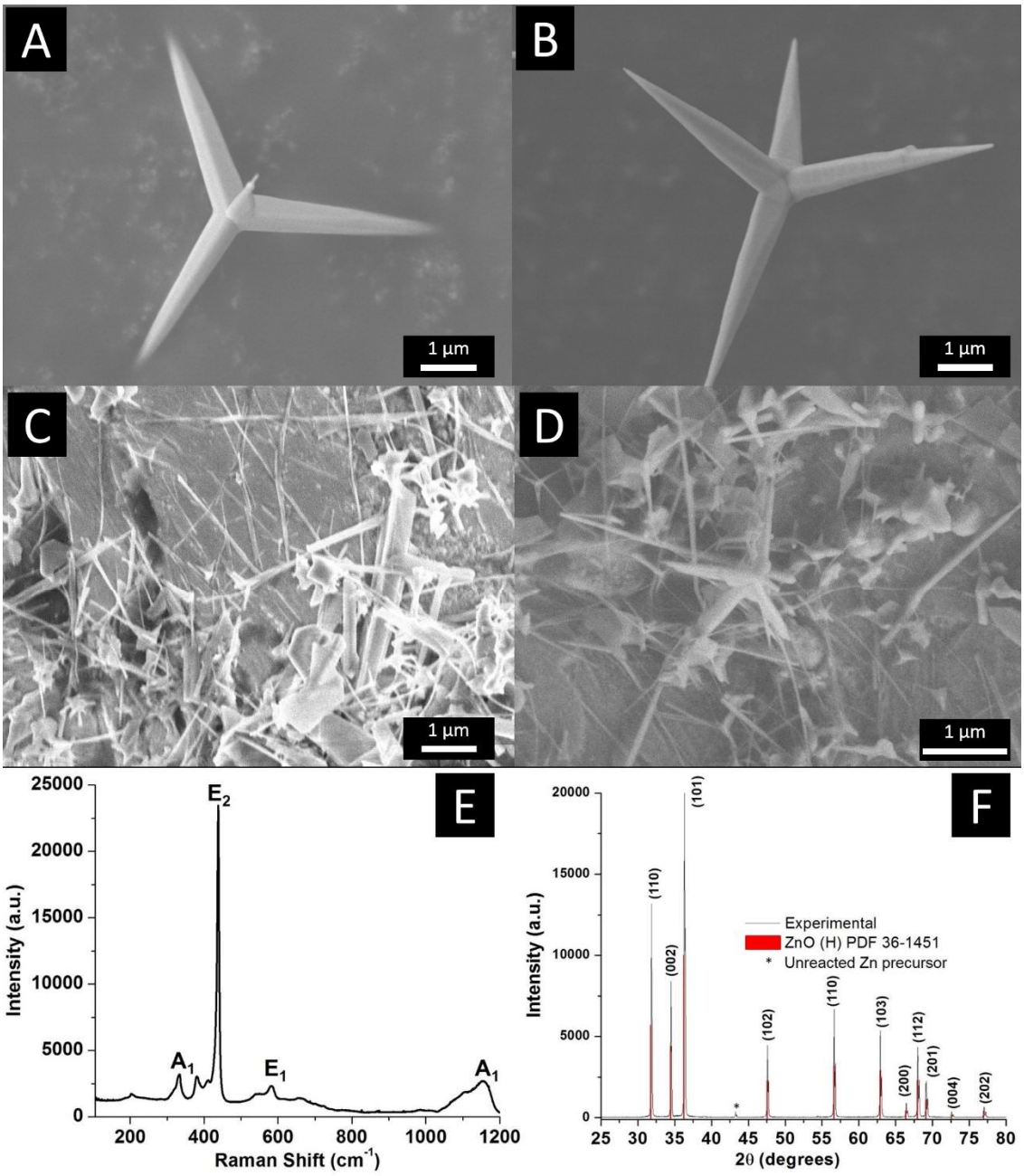

Figure IV.8. Defining nanotexturation using ZnO nanotetrapods. A, B) SEM images acquired for individual ZnO nanotetrapods indicating the four protuberant and tapered arms. The tetrapod morphology results inevitably results in the trapping of air pockets between the nanotetrapods and the base substrate, thereby giving rise to the Cassie-Baxter suspended droplet regime and stabilizing plastrons. C, D) SEM images depicting interconnected ZnO nanotetrapods residing on etched steel substrates. (E) Raman spectra and (F) XRD pattern acquired for ZnO nanotetrapods. The XRD pattern also indicates the reflections of the hexagonal zincite phase (JCPDS 36-1451). Reflections derived from residual Zn are marked with an asterisk.

IV.3.4 Adhering ZnO Nanotetrapods to Steel Substrates: Mechanical and Thermal Stability

The interlocked ZnO nanotetrapods show rather poor adhesion to the etched steel substrates upon spray deposition. However, in order to improve the adhesion of ZnO nanotetrapods onto etched carbon steel, an amorphous SiO_2 shell is constituted by condensation of surface hydroxyl groups of the nanotetrapods and steel surfaces with silanols obtained by the base-catalyzed hydrolysis of TEOS. Three different configurations have been tested in terms of adhesion to clean steel surfaces: (a) an initial condensation of TEOS with the surface silanols of the steel surface followed by spray deposition of ZnO nanotetrapods; (b) spray deposition of ZnO nanotetrapods from a TEOS dispersion in ethanol and water; and (c) an overlayer of TEOS after spray deposition of the initial ZnO nanotetrapod layer. Figure A.1 shows the results of ASTM 3359 testing of the samples assessed on a standardized scale of 0B to 5B with higher numerical figures representing better adhesion. In the absence of TEOS, the deposited coating is removed from almost every region of the scribed grid with a rating of 0B. The application of an initial TEOS layer or spray-coating from a TEOS dispersion slightly improves the adhesion to 1B but a large amount of the coating is still readily removed by application of the adhesive tape. However, application of a top layer of TEOS to an initially spray-deposited ZnO nanotetrapod coating earns the highest rating of 5B. Notably, the tests have been performed on flat and clean steel substrates and thus etched substrates with a greater degree of surface roughness are expected to provide an event greater extent of adhesion. The top-coated substrates furthermore show an adhesion strength of 450—550 g in ASTM D2197 scrape adhesion tests as compared to 0 g for tetrapods spray deposited without a TEOS layer.

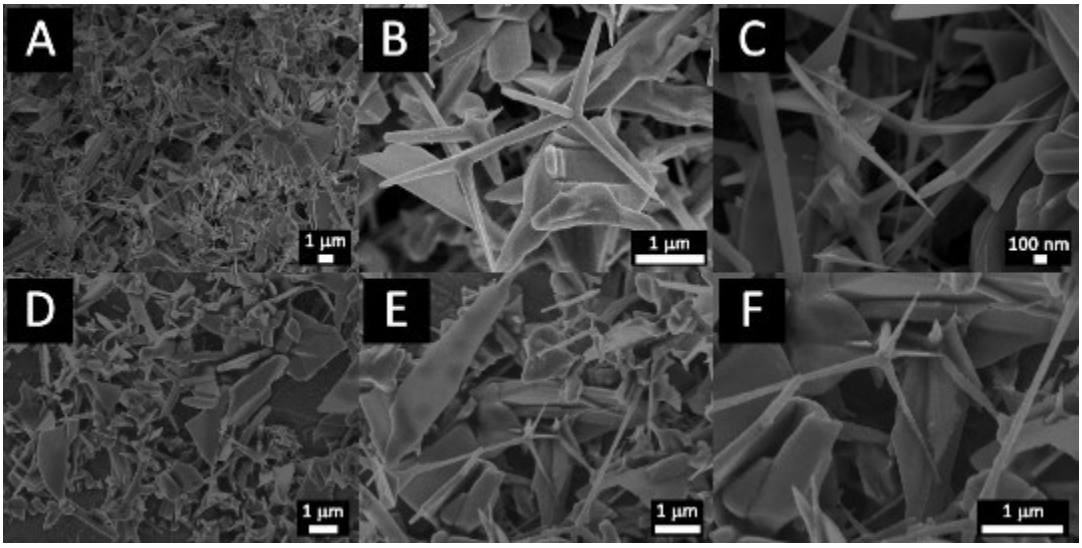

Figure IV.9. A-C) A ZnO nanotetrapod layer adhered to a steel substrate, etched with an HCl solution, using TEOS as the precursor to constitute a SiO_2 layer; D-F) A ZnO nanotetrapod layer adhered to a steel substrate, etched with a mixed acid solution, using TEOS as the precursor to constitute a SiO_2 layer. The panels show SEM images at increasingly higher magnifications.

Figure IV.9 shows the hierarchical texturation of etched steel substrates/ZnO nanotetrapod/TEOS-derived SiO_2 layers. The SEM images in Figure IV.9A—C correspond to steel substrates etched with an HCl solution, whereas the substrates depicted in Figure IV.9D—F have been etched with the mixed acid solution as described in Section IV.3.2. The highly porous and mesostructured topographies are easily discernible from the SEM images, demonstrating the scope for stabilizing air pockets between the ZnO nanotetrapods and the etched steel surfaces giving rise to synthetic plastrons.

Thermogravimetric analysis demonstrates that the ZnO tetrapods do not undergo any discernible weight loss up to a temperature of 900°C. Upon deposition of an amorphous layer of SiO_2, a small weight loss of ca. 3.8% is observed in the temperature range of ca. 160—325°C. This weight loss is attributed to the loss of residual water and hydroxyl groups from the porous SiO_2 layer, which leads to a greater degree of cross-linking and compaction of the silica matrix. The

inorganic components of the coating are thus thermally robust and compatible with high-temperature operation.

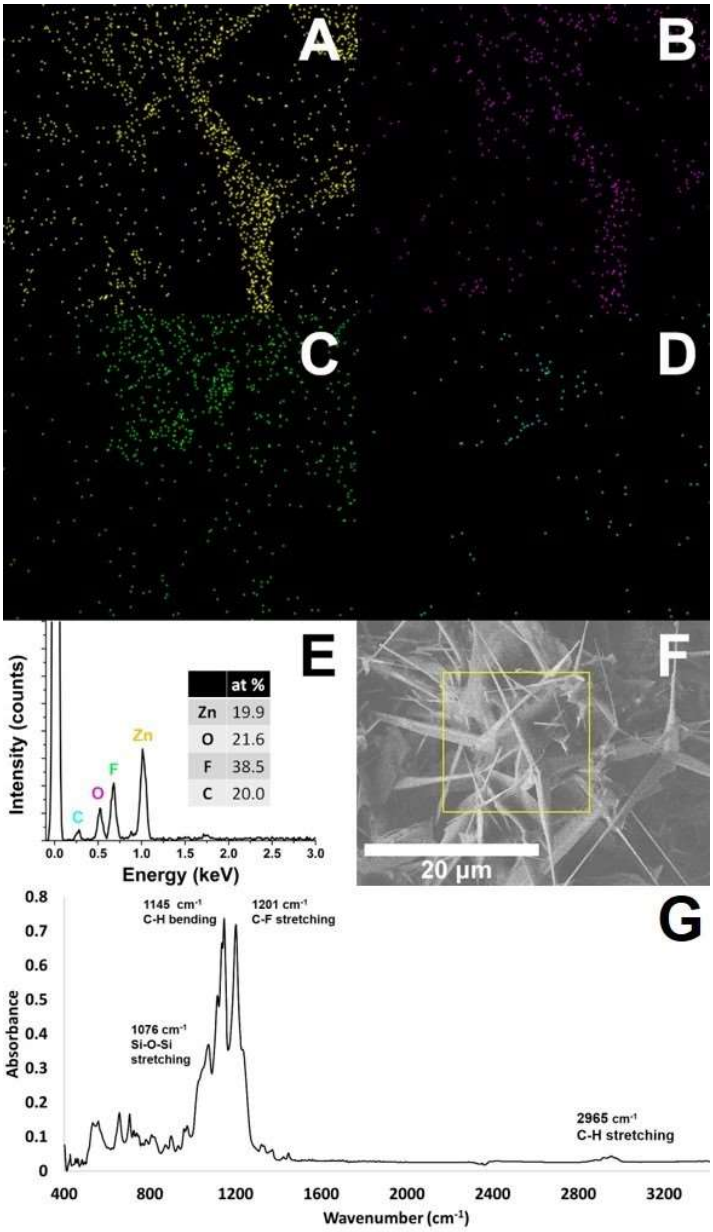

Figure IV.10. A) Zinc, B) oxygen, C) flourine, and D) carbon energy dispersive X-ray maps of ZnO nanotetrapod samples functionalized with a perfluorinated silane, (heptadecafluoro-1,1,2,2-tetrahydrodecyl) trimethoxysilane. The energy dispersive X-ray maps (A-D) have correspond to a 15 µm x 15 µm area. E) The EDX spectrum of the sample area analyzed in (F). (F) SEM image of the perfluorinated ZnO nanotetrapods; the yellow box delineated the region mapped by EDX. (G) attenuated total reflection (ATR) FTIR spectra of TEOS-coated ZnO soaked for 1 h in a 2.7 mM butanol solution of (heptadecafluoro-1,1,2,2-tetrahydrodecyl)trimethoxysilane.

IV.3.5 Surface Functionalization with Molecular Monolayers: Modulating Surface and Interfacial Energies

As indicated by Equation 2, a low surface energy is imperative to ensure non-wettability towards low-surface-tension liquids. Pendant fluorinated moieties are particularly useful owing to their minimal interactions with both water and hydrocarbons. The intermolecular interactions of C—F bonds are incompatible with hydrogen bonding favored by water molecules and dispersive interactions favored by hydrocarbons. As a consequence, when a water or hydrocarbon droplet impinges on a fluorinated surface, the adsorption enthalpy is strongly positive and thus the liquid—solid interfacial energies in Equation 1 remain quite large. In other words, the adhesive forces at a fluorinated surface are inadequate to overcome the cohesive forces between droplet molecules. The surface energy will depend on the surface grafting density of fluorinated moieties, which in turn is a function of the binding group, the length of the perfluorinated alkyl chains, and the processing conditions (concentration, temperature, and soak time). These parameters determine the extent to which the fluorinated silanes form a 2D crystalline monolayer on the nanotetrapodal surfaces.[9–11] In essence, crystalline packing of molecules within monolayers involves a trade-off between the decrease in enthalpy as C-F interactions are optimized along the length of the pendant groups and the decrease in entropy resulting from the loss of rotational degrees of freedom in ordered monolayers. The condensation of the fluorinated silanes to form oligomers in solution also competes with surface grafting of these species and becomes especially significant at higher concentrations.

Varying lengths of perfluorinated alkyl chains have been evaluated using water contact angle measurements with the supposition that all other things remaining the same the most ordered monolayers will yield the highest water contact angles. Triethoxyfluorosilane represents the

shortest chain length (C2), nonafluorohexyltriethoxysilane represents the medium chain derivative (C6), and heptadecafluoro-1,1,2,2-tetrahydrodecyl)trimethoxysiloxane represents the long chain derivative (C10). Hereafter, each fluorinated silane will be mentioned as C2, C6, and C10. As an example of an entirely distinct binding mode, 1H,1H,2H,2H-perfluorooctanephosphonic acid has also been used as a fluorinated derivative because it has previously been shown to have a high affinity for ZnO surfaces.[12] The phosphonic acid moiety can potentially directly bind ZnO surfaces, whereas the silanes are reactive towards surface hydroxyl groups.

The etched surfaces have been screened using the three types of silanes initially using water contact angles as a measure of the surface energy and roughness. The C6 fluorinated silane exhibits the highest degree of hydrophobicity with a contact angle of 158° for the HCl etched sample. **Figure IV.10** illustrates an EDX map acquired for ZnO tetrapods functionalized with the C6 perfluorinated silane. The localization of Zn and F signals verifies the surface grafting of the fluorinated moieties with a measured Zn:F ratio of 20:39. In addition the FTIR spectra acquired in attenuated total reflectance mode shown in Figure IV.10G indicates vibrational modes at 1201 and 1146 cm^{-1}, which can be assigned to C-F stretching and C-F bending modes of the perfluoralkyl chains of the (heptadecafluoro-1,1,2,2-tetrahydrodecyl) trimethoxysilane, respectively.[13] In addition, a Si-O-Si stretch at 1076 cm^{-1} derived from the TEOS coating is also observed.[13] Thermogravimetric analysis indicates ca. 25% weight loss in the temperature range of 300—500°C arising from breakdown and removal of pendant fluorinated groups from the silanes attached to the ZnO tetrapods, which suggests an excellent window of operation considering that most crude oil is handled below a temperature of 200°C.

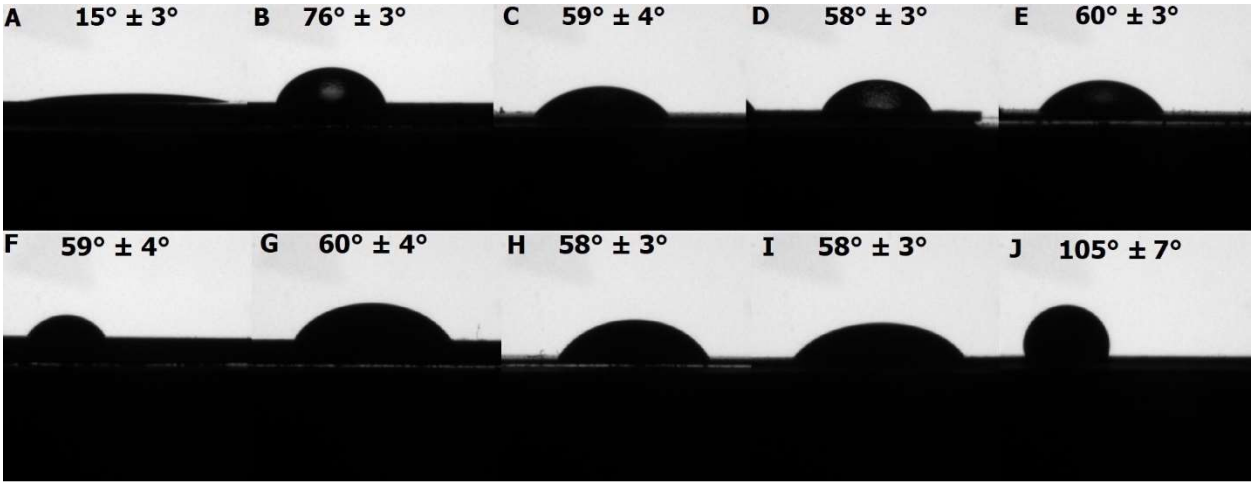

Figure IV.11. Hexadecane contact angles of (A) cleaned blank steel, (B) fluorinated cleaned blank steel, (C) steel etched with HCl at 80°C for 1 h and fluorinated, (D) steel etched with HCl at 80°C for 1 h, coated with ZnO nanotetrapods, and fluorinated, (E) steel etched with HCl at 80°C for 1 h, coated with ZnO nanotetrapods, TEOS coated, and fluorinated. F-J) heavy oil contact angles for samples A-E, respectively. In all cases, surface functionalization was achieved by immersion in a 2.7 mM butanol solution of the C6 perfluorinated silane for 1 h.

The better ordering of C6 as compared to C2 and C10 fluorinated silanes is thought to derive from the optimal balance of enthalpic gain and entropic loss at these chain lengths; C2 likely has only a marginal enthalpic stabilization given that it has just two carbon atoms, whereas for C10, slower kinetics arising from longer chain lengths likely give rise to higher thermal disorder[9] on surfaces and the slower diffusion of these more sterically encumbered species further hinders surface reorganization. It is worth noting the perfluorinated phosphonic acid yields comparable or superior results depending on the etching conditions. For the sample etched in a 1:1 HCl:H_2O solution for 60 min at 80°C, functionalization with perfluorinated phosphonic acid yields a contact angle of 140° ± 5°. Analogously, a water contact angle of 145° ± 2° has been obtained for blank steel etched with mixed acid at 93°C for 90 s and functionalized with perfluorinated phosphonic acid, whereas the C6 silane yields a water contact angle of 133° ± 3°.

These two moieties, the perfluorinated phosphonic acid and C6 silane, have been used to further functionalize the etched steel substrates coated with ZnO nanotetrapods as per the process flow depicted in Figure IV.2 and are further challenged with hexadecane and heavy oil as test liquids apart from water (selected values are noted in **Table 2**). The latter crude oil fraction is particularly relevant to real-world applications and is a viscous liquid that strongly wets pipelines and storage tanks.

Table IV.2. Selected water, hexadecane, and heavy oil contact angles measured for micro- and nanotextured steel substrates with ZnO nanotetrapods (optimized at 7.8 mg/cm^2) and TEOS (optimized at 3.9 µL/cm^2) and upon functionalization with either the C6 perfluorinated silane or perfluorinated phosphonic acid. The "best-in-class" sample is highlighted in bold.

Etching Agent	Time	ZnO Loading	TEOS Loading	Fluorinated Silane	CA Water	CA Hexadecane	CA Heavy Oil
None	None	None	None	None	63° ± 3°	15° ± 3°	59° ± 4°
None	None	None	None	2.7 mM M chain	108° ± 9°	76° ± 3°	60° ± 4°
None	None	7.8 mg/cm^2	3.9 µL/cm^2	2.7 mM, 9 h M chain	164° ± 2°	76° ± 4°	108° ± 6°
Mixed acid	45 s	7.8 mg/cm^2	3.9 µL/cm^2	2.7 mM M chain	165° ± 4°	51° ± 12°	92° ± 6°
Mixed acid	45 s	7.8 mg/cm^2	3.9 µL/cm^2	8.1 mM M chain	164° ± 3°	68° ± 2°	125° ± 7°
Mixed acid	45 s	7.8 mg/cm^2	3.9 µL/cm^2	2.7 mM, 9 h M chain	157° ± 4°	56° ± 3°	119° ± 4°
HCl	1 h	None	None	2.7 mM M chain	107° ± 2°	59° ± 4°	58° ± 3°
HCl	1 h	7.8 mg/cm^2	None	2.7 mM M chain	155° ± 6°	79° ± 3°	58° ± 3°
HCl	1 h	7.8 mg/cm^2	3.9 µL/cm^2	2.7 mM M chain	164° ± 5°	60° ± 2°	105° ± 7°
HCl	1 h	7.8 mg/cm^2	3.9 µL/cm^2	2.7 mM 9 h M chain	152° ± 4°	103° ± 4°	124° ± 8°
HCl	**1 h**	**7.8 mg/cm^2**	**3.9 µL/cm^2**	**8.1 mM M chain**	**168° ± 5°**	**91° ± 2°**	**139° ± 8°**
HCl	1 h	7.8 mg/cm^2	None	27.0 mM FPA	169° ± 3°		133° ± 1°

The results of water contact angle measurements for ZnO nanotetrapods deposited onto etched carbon steel and then modified with the C6 silane or the perfluorinated phosphonic acid are provided in Table 2. Functionalization of ZnO nanotetrapods on etched steel with the C6 perfluorinated silane yields the highest water contact angle for HCl and mixed acid etchants (165° and 164°, respectively), suggestive of strongly hydrophobic behavior. Indeed, these values represent conservative estimates since water droplets are strongly repelled by these surfaces. The superior non-wettability obtained for the perfluorinated C6 silane in comparison to the perfluorinated phosphonic acid (which yields values of 164°±5° and 153°±5°) is likely a result of the greater grafting density of the former on the TEOS coated surface that overcoats much of the ZnO nanotetrapod layer. Mixtures of the fluorinated silanes have also been examined by immersion of the substrates in two different silane solutions for 1 h each. In every case, the water contact angle is reduced in comparison to their single component monolayer counterparts no matter the etchant. It is hypothesized that mixed monolayers show a lower degree of ordering on the ZnO surfaces, which translates to a lower grafting density of pendant fluorinated species and thus yields a higher surface energy.

The C6 perfluorinated silane and 1H,1H,2H,2H-perfluorooctanephosphonic acid have been further examined as surface modifiers for the two most textured surfaces down-selected from the process flow mapped in Figure IV.2 based on measurements of water contact angles for etched steel with ZnO tetrapods and a TEOS topcoat. The functionalized substrates are challenged with heavy oil and hexadecane in addition to water (Table 2). As a control, the contact angles of hexadecane and heavy oil on flat carbon steel are 15° ± 3° (**Fig. IV.11A**) and 59° ± 4°, (**Fig. IV.11F**), respectively. The viscous heavy oil spreads to cover and wet the surface of blank steel and cannot be drained from the surface. Upon surface modification with the C6 perfluorinated

silane, the hexadecane contact angle increases to 76° ± 3° (Fig. IV.11B), whereas the heavy oil contact angle is essentially unchanged at 60° ± 4° (Fig. IV.11G). Fig IV.11C indicates that microscale texturation induced by etching with hydrochloric acid and successive fluorination increases the hexadecane contact angle to 59° ± 4° compared to a blank sample, whereas the heavy oil angle is essentially unchanged at 58° ± 3° (Fig. IV.11H). After the successive steps of HCl acid roughening, deposition of ZnO nanotetrapods, and surface modification with the fluorinated silane, the hexadecane and heavy oil contact angles are 58° ± 3° (Fig. IV.11D) and 58° ± 3° (Fig IV.11I), showing no measurable increase for the liquids. However, after HCl acid roughening, deposition of ZnO nanotetrapods, and TEOS spray coating followed by surface functionalization with the C6 perfluorinated silane, the hexadecane and heavy oil contact angles increase to 60° ± 3° (Fig. IV.11E) and 105° ± 7° (Fig IV.11J), respectively. Here we note that the amorphous SiO_2 layer provides additional sites to bind the perfluorinated monolayer, thereby greatly increasing the grafting density of the pendant fluorous groups. Based on Figure IV.9 and the relevant water contact angles listed in Table 2, the substrates are sufficiently structured to allow for superhydrophobicity to be derived from the combination of etching-induced micron-scale and nanotetrapod-induced nanoscale texturation. However, the surfaces of the ZnO nanotetrapods are not adequately functionalized by the perfluorinated silanes and only upon deposition of an amorphous SiO_2 layer is the grafting density of the perfluorinated silanes greatly increased allowing for manifestation of oleophobicity towards heavy oil.

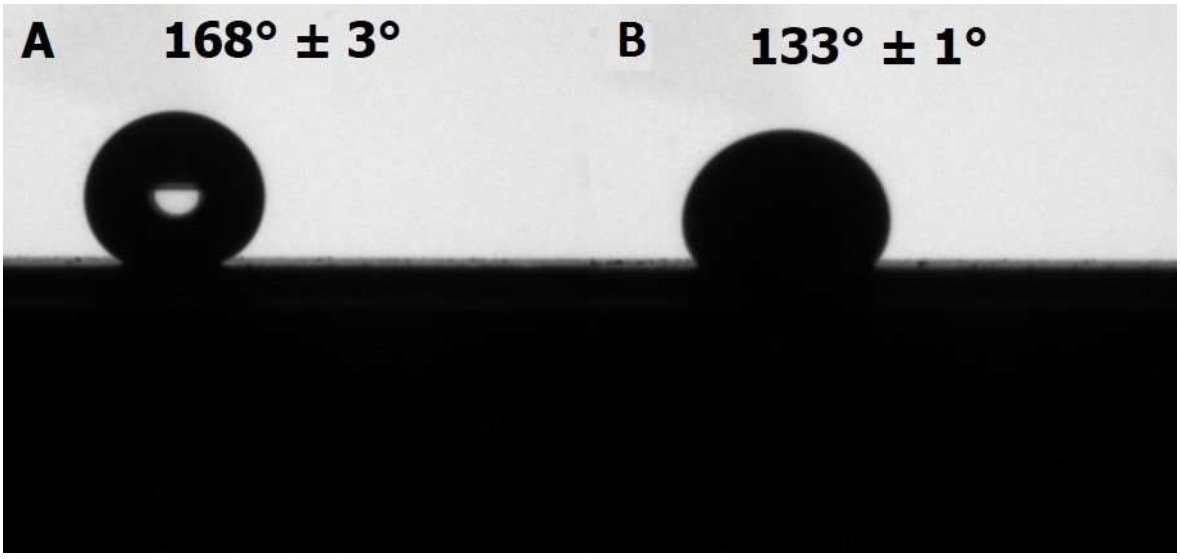

Figure IV.12. (A) Water contact angles of carbon steel after etching with HCl:H_2O solution at 80°C for 1 h, deposition of 7.8 mg/cm^2 of ZnO nanotetrapods, and surface functionalization with a 27.0 mM THF solution of 1H,1H,2H,2H-perfluorooctanephosphonic acid. (B) demonstrates the contact angle for heavy oil on the same sample.

The most promising sample from the process flow shown in Figure IV.2 is HCl etched steel integrated with ZnO nanotetrapods with an amorphous SiO_2 overlayer, which exhibits a water contact angle of 168° ± 5° (Table 2). In order to render this surface oleophobic (and indeed omniphobic), an attempt has been made to greatly increase the grafting density of fluorinated species. Upon increasing the concentration of the C6 perfluorinated silane to 8.1 mM, the hexadecane and heavy oil contact angles of this sample are further increased to 91°±2° and 139° ± 8°, respectively. The greatly enhanced heavy oil contact angles of this substrate suggests strong omniphobicity resulting from an optimal combination of low surface energy and hierarchical mesoscale texturation. This surface not only has trapped plastronic air pockets but the high grafting density of perfluorinated species imparts a low surface energy. Consequently, oil droplets are suspended across nanoscale and microscale topographies with relatively minimal

contact (in Cassie—Baxter mode as expressed in Chapter I, Eq. I.4) with a high value of γ_{SL} at the intermittent contact points.

Figure IV.12 indicates the water and heavy oil contact angles for a sample wherein a high density of the perfluorinated phosphonic acid is directly grafted onto the ZnO tetrapodal nanostructures. A heavy oil contact angle of 133 ± 1° is obtained indicating again that a high grafting density of the perfluorinated monolayer needs to be established to render a surface that is superhydrophobic by dint of nanotexturation (with a water contact angle of 168°) strongly oleophobic.

The motion of a droplet on a surface in the range of non-wettability depends on the balance of forces between gravity and surface tension (unbalanced Young's forces) at the contact line.[14] In the Cassie—Baxter regime, the contact line can become pinned resulting in hysteresis between advancing and receding contact angles. From a practical perspective, this implies that for omniphobic behavior of a liquid droplet, an optimal degree of nanotexturation is required. A very high degree of nanotexturation provides an abundance of sites to pin the liquid droplet, whereas with minimal nanotexturation, it becomes difficult to stabilize the droplet in the Cassie—Baxter regime and conformal wetting (Wenzel regime) becomes the preferred wetting regime. A ZnO loading of ca. 7.8 mg/cm^2 has been found to be optimal to facilitate not just higher water contact angles but also facile gliding of water droplets. A liquid droplet can glide across a surface when

$$\rho V \mathrm{g}\, sin\alpha \; > \pi r \gamma \; (\cos\theta_R - \cos\theta_A) \qquad (4)$$

where r is the radius of the contact line, γ is the surface tension of the liquid, θ_R and θ_A are the receding and advancing contact angles, respectively, ρ is the density of the liquid, V is the volume of the droplet, g is the acceleration due to gravity, and α is the angle by which the

substrate is tilted. Water droplets very readily glide across the substrates fabricated here. The facile motion of water droplets is facilitated by the high density of water (1000 kg m^{-3}) and the fact that the radius of the contact line is rather small given the high water contact angle (>160°, Fig. IV.12).[15] Consequently, the gliding of water droplets is relatively more forgiving of contact angle hysteresis due to defects. In contrast, the hydrocarbons have a relatively lower density and wet the surfaces relatively more (heavy oil contact angles in the range of 133—139°, Table 2), giving rise to a relatively larger radius of the contact line. As a consequence, reducing the contact angle hysteresis (to reduce the ($\cos\theta_R$-$\cos\theta_A$) term in Chapter I Eq. I.4) and further enhancing non-wettability (to reduce *r* in Eq. 4) is imperative to achieve gliding of the oil droplets at reasonable values of α and is indeed the focus of Chapters V and VI.

IV.4 Conclusions

A step-wise modular approach is used to arrive at thermally robust and mechanically resilient surfaces that exhibit robust universal non-wettbaility. The approach combines microscale and nanoscale texturation with surface modification to obtain surfaces that are both hydrophobic as well as oleophobic and repellant to highly viscous heavy oil. Microscale texturation is defined by etching carbon steel substrates selectively along dislocations to define terraces. Nanoscale texturation is introduced by the deposition of ZnO nanotetrapods. The distinctive morphology of the nanotetrapods with four protuberant arms defines a nanoscale topography on the etched steel substrates and facilitates the trapping of air pockets between the nanostructured layers and the steel substrates. TEOS is used as a precursor to constitute a thin layer of amorphous SiO_2 that binds the ZnO nanotetrapods to the steel surfaces based on condensation of silanols with surface hydroxyl groups on both the tetrapods and the surface oxides of the steel. Functionalization of the ZnO nanotetrapods with perfluorinated phosphonic acids and of the ZnO nanotetrapod/SiO_2

layers with perfluorinated silanes reduces the surface energy and yields surfaces that strongly repel water and oil. Liquid droplets impinging such surfaces are suspended in Cassie—Baxter states by the trapped air pockets within minimal contact points defined by the nanoscale terrain. The most omniphobic samples in terms of their ability to repel heavy oil and to allow gliding of heavy oil droplets obtained here correspond to carbon steel etched with a 1:1 mixture of HCl and H_2O for 1 h at 80°C, with a 7.8 mg/cm^2 loading of ZnO nanotetrapods, 3.9 μL/cm^2 overlayer of TEOS, and functionalization by 1 h immersion in a 8.1 mM solution of the C6 perfluorinated silane, which shows water and heavy oil contact angles of 168° ± 5° and 139° ± 8°, respectively. The direct integration of hierarchical texturation and surface modification onto steel substrates provides a viable solution for oil-handling that is scalable and compatible with existing infrastructure. Such ceramic omniphobic surfaces are stable up temperatures of 295° suggesting viability for applications in oil-handling equipment such as tanker trucks, railcars, and pipe interiors. In addition to base metal substrates, ZnO nanotetrapods can also be applied to stainless steel meshes in order to generate mesoscale textured surfaces without the need for selective etching procedures. The meshes provide an underlying micron-scale texturation that amplifies the influence of the tetrapods. In Chapter V, this process in conjunction with chemical functionalization using perfluorinated phosphonic acids highlights the intricacies of combining texturation and the reduction of surface energy in order to achieve the gliding of both water and viscous oil.

IV. 5 References

(1) Velazquez, J. M.; Baskaran, S.; Gaikwad, A. V; Ngo-Duc, T.-T.; He, X.; Oye, M. M.; Meyyappan, M.; Rout, T. K.; Fu, J. Y.; Banerjee, S. *ACS Appl. Mater. Interfaces* **2013**, *5*, 10650–10657.

(2) Stöber, W.; Fink, A.; Bohn, E. *J. Colloid Interface Sci.* **1968**, *26* (1), 62–69.

(3) Bramfitt, B. L.; Benscoter, A. O. *Metallographer's Guide: Practice and Procedures for Irons and Steels*; ASM International, 2001.

(4) Wang, Z. L. *MRS Bull.* **2007**, *32* (2), 109–116.

(5) Song, J.; Wang, X.; Riedo, E.; Wang, Z. L. *J. Phys. Chem. B* **2005**, *109* (20), 9869–9872.

(6) Jin, S.; Bierman, M. J.; Morin, S. A. *J. Phys. Chem. Lett.* **2010**, *1* (9), 1472–1480.

(7) Morin, S. A.; Bierman, M. J.; Tong, J.; Jin, S. *Science* **2010**, *328* (April), 476–480.

(8) Cuscó, R.; Alarcón-Lladó, E.; Ibáñez, J.; Artús, L.; Jiménez, J.; Wang, B.; Callahan, M. *Phys. Rev. B* **2007**, *75* (16), 165202.

(9) Ulman, a. *Chem. Rev.* **1996**, *96* (4), 1533–1554.

(10) Kern, M. E.; Watson, D. F. *Langmuir* **2013**, *29* (45), 13797–13807.

(11) Cho, J.; Choi, Y. H.; O'Loughlin, T. E.; De Jesus, L.; Banerjee, S. *Chem. Mater.* **2016**, *28* (19), 6909–6916.

(12) Timpel, M.; Nardi, M. V.; Krause, S.; Ligorio, G.; Christodoulou, C.; Pasquali, L.; Giglia, A.; Frisch, J.; Wegner, B.; Moras, P.; Koch, N. *Chem. Mater.* **2014**, *26* (17), 5042–5050.

(13) Park, J.-U.; Kim, W.-S.; Bae, B.-S. *J. Mater. Chem.* **2003**, *13* (4), 738–741.

(14) Bonn, D.; Eggers, J.; Indekeu, J.; Meunier, J. *Rev. Mod. Phys.* **2009**, *81* (2), 739–805.

(15) *CRC Handbook of Chemistry and Physics*, 97th ed.; Haynes, W. M., Bruno, T. J., Lide, D. R., Eds.; CRC Press: Boca Raton, 2016.

CHAPTER V

BIOMIMETIC PLASTRONIC SURFACES FOR HANDLING OF VISCOUS HEAVY OILS[*]

V.1 Outline

Unconventional deposits such as heavy crude oil and natural bitumen represent a steadily increasing proportion of extracted fuels. The rheological properties of heavy crude oil represents a formidable impediment to their extraction, transportation, and processing and have necessitated considerable retooling and changes to process design. The cleaning and maintenance of storage containers, pipelines and transportation vectors such as railcars represents a considerable cost as well as safety burden. Whilst considerable effort has focused on the design of engineered surfaces for facilitating the transport and handling of common liquids, options for handling of heavy crude oils are extremely sparse. Here we show highly textured inorganic substrates generated by depositing ZnO nanotetrapods onto periodically ordered stainless steel mesh substrates to bring about multiscale texturation and porosity characterized by trapping of plastronic air pockets at the solid/liquid interface. Such structures are strongly ejected upon immersion in water. Further reduction of the surface energy has been achieved by constituting a helical self-assembled monolayer of a perfluorinated phosphonic acid on the ZnO surfaces. The functionalized substrates demonstrate remarkable superoleophobic behavior towards heavy crude oil and are readily able to glide both water and heavy oil droplets.

---

[*] Reproduced with permission from "Biomimetic Plastronic Surfaces for Handling of Viscous Heavy Oils." O'Loghlin, T.E.; Dennis, R.V.; Fleer, N.A.; Alivio, T.E.G.; Ruus, S.; Wood, J.; Gupta, S.; and Banerjee, S. *Energy & Fuels,* **2017**, *31* (9), 9337-9344. Reproduced by permission of the American Chemical Society.

V.2 Introduction

The relentless increase of global energy consumption and declining reserves of light crude oil have led to increasing reliance on unconventional deposits such as heavy crude oil and natural-bitumen sourced from sub-surface deposits such as in Canada and Venezuela.[1–3] Advances in cold production, steam flooding, and enhanced oil recovery processes have nudged recovery metrics higher and rendered extraction of these deposits economically viable.[1] However, the handling, transport, and upgrading of these fuels comes with its own set of complex challenges.[4,5] Methods such as steam-assisted gravity drainage extract emulsions at high temperatures and the recovered oils tend to be highly viscous comprising large fractions of asphaltenes. The challenging rheological characteristics of these fluids render standard coatings for handling and transportation equipment, many of which are polymeric in nature, incompatible with prolonged operation. Current industrial practice involves handling at substantially elevated temperatures or the mixing of light oil fractions (diluents) with bitumen; the latter is commonly used to facilitate transport to refineries and represents a considerable penalty in terms of cost, process safety, and efficiency. A tremendous challenge is thus the design of surfaces that are not wetted by heavy oils and allow for the facile gliding of these viscous fluids.

Science has often looked to nature to provide inspiration and insight, especially since nature has evolved particularly useful tools for handling of complex fluids. Nature abounds with examples of plants and insects that present superhydrophobic surfaces with contact angles in excess of 150° and are thus not readily wetted by water droplets, even upon complete immersion.[6] Manifestation of hydrophobic behavior in nature allows for the effective self-cleaning of surfaces including in the famous example of the lotus leaf.[7,8] Such superhydrophobic behavior is derived from a combination of mesoscale texturation and chemical incompatibility of the waxy surfaces

with water, which results in water droplets gliding readily without adhesion.[9] As another prominent example, many insect and arachnid species possess fine hairs along their bodies that render them hydrophobic. These setae and densely packed microtrichia provide both micro- and nanoscale texturation, which allows for the trapping of air bubbles when the insects are submerged.[10,11] The bubbles thus serve as incompressible reservoirs of oxygen and carbon dioxide and can then be used by the insect during respiration; oxygen can furthermore continuously diffuse from water into the air film (plastron).[10,12,13] However, as a result of the lower surface tension of oil droplets, rendering surfaces superoleophobic is much more difficult and indeed there are no examples of naturally occurring oleophobic surfaces. Oleophobicity has been successfully induced in surfaces through a combination of reentrant curvature, low surface energy, and multiscale texturation.[14,15] However, most such engineered surfaces tend to require polymeric layers or lithographic patterning, limiting their applicability in large-area formats such as required for processing millions of barrels of oil. Furthermore, the gliding of viscous oils has yet to be realized.

In this article, we demonstrate a scalable plastron architecture constructed by integrating ZnO nanotetrapods onto a stainless steel mesh with micron-scale texturation. The hierarchical texturation renders the architecture superhydrophobic and indeed coated substrates immersed in water are rapidly ejected from the surface. Functionalization of the ZnO nanosurfaces with perfluorinated phosphonic acids yields a well-ordered self-assembled monolayer. The resulting low-surface-energy hierarchically textured surface is rendered superoleophobic and indeed readily allows for gliding of droplets of heavy oil.

V.3 Materials and Methods

ZnO nanotetrapods were generated using a previously deployed technique based on oxidation of Zn metal in air as described in Chapter II.[16,17] The resulting ZnO tetrapods were harvested and dispersed in 2-propanol (99.9%, Fisher Scientific). The solutions were then spray coated onto 316 stainless steel meshes (McMaster-Carr) using an airbrush with a nozzle diameter of 0.5 mm, aided by an air compressor set at 45 psi.

In order to reduce the surface energy of the samples, fluorination was achieved using 1H,1H,2H,2H-perfluorooctanephosphonic acid (Sigma-Aldrich). A concentration of 27 mM perfluorinated phosphonic acid in tetrahydrofuran (Millipore) was found to be optimal based on systematic screening of concentrations and immersion time. The ZnO-coated substrates were immersed in THF solution and allowed to soak for 1 h, followed by drying under air.

V.3.1 Characterization

A CAM 200 Optical Goniometer was used to measure all contact angles. All test liquids had a drop size of *ca.* 10 μL. A mechanical pipette was used to apply doubly distilled and deionized water (ρ = 18.2 MΩ cm^{-1}); and a manual micropipette was used to apply heavy oil droplets. The heavy oil used here was obtained from Cenovus Energy, Inc. and was extracted from the Northern Alberta Oil Sands using the steam-assisted gravity drainage method. The heavy oil used has a viscosity of *ca.* 140,005 mPa·s at 25°C. All listed contact angles in Chapter V are a result of at least three averaged values measured on different parts of the prepared substrates.

XPS spectra were collected with an Omicron XPS/UPS system equipped with an Argus detector using Mg Kα X-rays (source energy of 1253.6 eV) with sample charge neutralization achieved

using a CN10 electron flood source. A spectral resolution of 0.8 eV was used in the measurements. High-resolution spectra were collected at a pass energy of 150 eV (in constant analyzer energy (CAE) mode) and at an energy step size of 0.05 eV. High-resolution spectra were calibrated against the C 1s line of adventitious carbon (284.8 eV). FTIR data were acquired using a Bruker Vertex-70 FTIR instrument equipped with a Pike MIRacle™ single reflection horizontal attenuated total reflectance (ATR) accessory.

The morphology of the ZnO tetrapods was imaged using a JEOL JSM-7500F field-emission scanning electron microscope (FE-SEM) equipped with a high brightness conical FE gun and a low aberration conical objective lens. A cold cathode UHV field emission conical anode gun was used as the source. Imaging was performed at an accelerating voltage of 10 kV. The instrument resolution was ca. 1.0 nm. False-color elemental maps were generated using an Oxford energy-dispersive X-ray (EDX) system. During the analysis, the following parameters were used: accelerating voltage of 15 kV, emission current of 9 μA, and probe current of 11 μA. False-color elemental composition maps were generated using the Inca Suite 5.05 software.

V.4 Results and Discussion

Chapter II, we have demonstrated the fabrication of membranes for water/oil separation based on the orthogonal wettability of ZnO nanotetrapods towards the two liquids.[17] In this chapter, we demonstrate that ZnO nanotetrapods integrated onto stainless steel mesh substrates form plastronic architectures by dint of trapped air pockets. The use of metal meshes instead of continuous steel surfaces gives rise to a dynamic interconnected porous plastronic network.[5,6] Such an architecture is schematically illustrated in **Figure V.1** and is strongly hydrophobic and is

additionally rendered oleophobic towards viscous heavy oils by surface functionalization with self-assembled monolayers of a perfluorinated phosphonic acid.

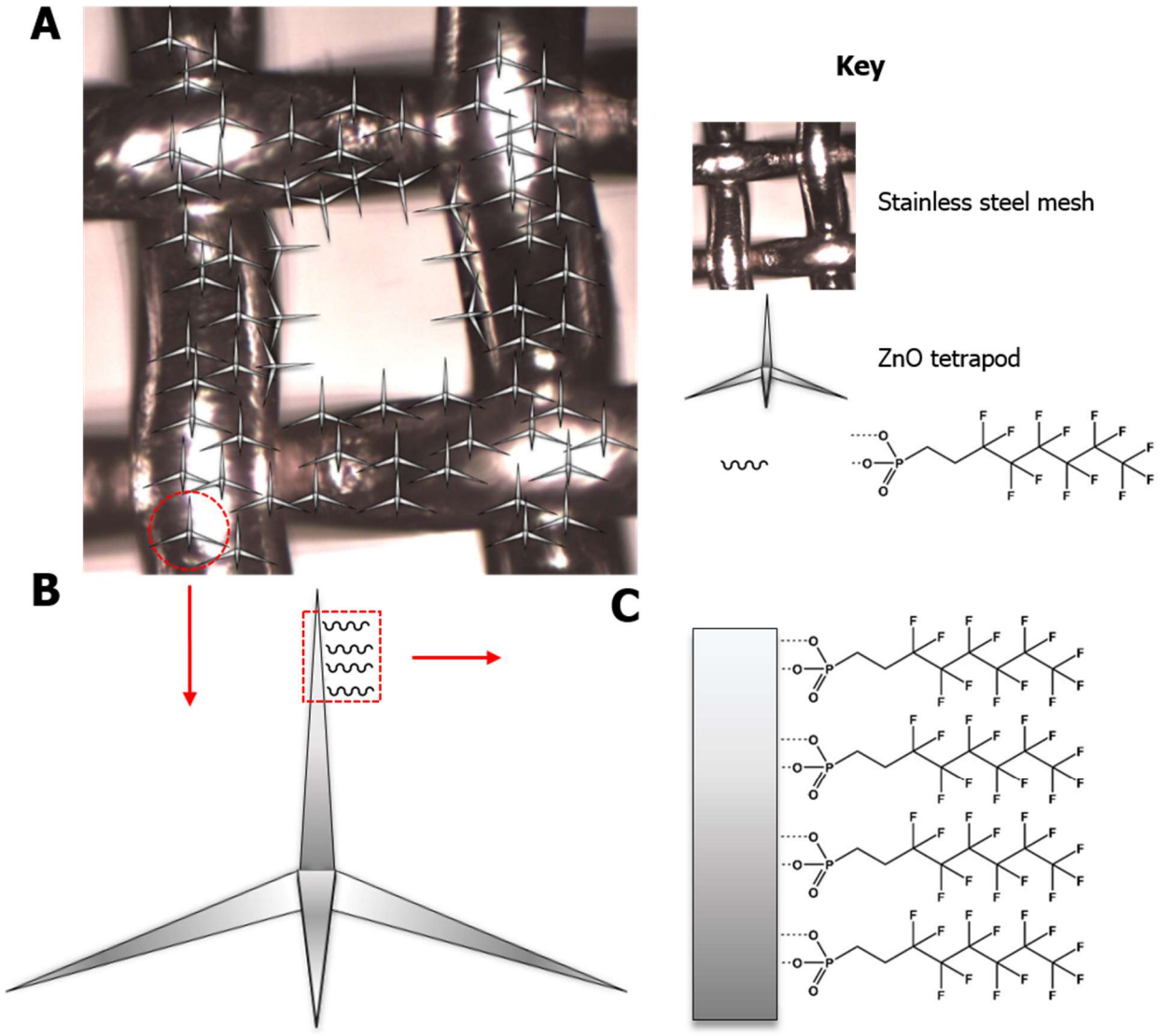

Figure V.1. (A) Schematic depiction of a plastronic architecture designed to glide heavy oil droplets. ZnO tetrapods shown in (B) are arrayed onto a microtextured stainless steel mesh. The ZnO nanotetrapods are further functionalized with 1H,1H,2H,2H-perfluorooctanephosphonic acid that forms a self-assembled monolayer as depicted in (C).

The nanotetrapodal geometry of the ZnO nanostructures provides an excellent means for achieving nanoscale surface texturation since even upon aggregation one or more arms remain protuberant from the mesh substrate,[18] as illustrated by the SEM images in **Figure V.2**. An interconnected network with a protruding nanoscale topography is obtained even upon deposition by spray coating without need for specific lithographic patterning. The tetrapodal morphology provides re-entrant curvature, allows for trapping of air within the porous domains, and ensures there is only a limited area where a liquid/solid interface can be established.

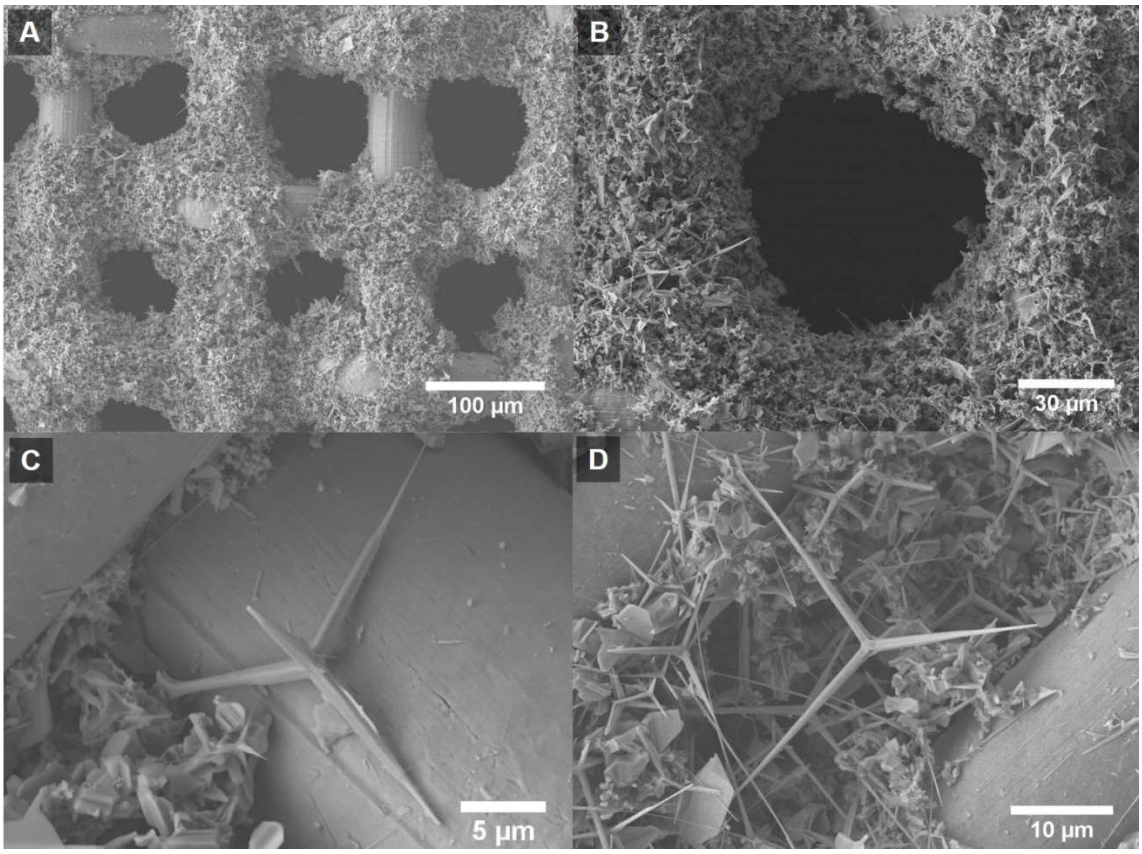

Figure V.2. SEM images of (A) a stainless steel mesh with a pore size of ca. 84 µm coated with ZnO tetrapods; (B) magnified view of a single pore of the ZnO-coated mesh; (C) a lone tetrapod suspended on the stainless steel mesh; (D) an interconnected network of ZnO tetrapods.

Figures **V.3A-F** depict contact angles for water and heavy oil droplets measured for a bare cleaned stainless steel mesh substrate (with a pore size of 180 μm) and for the same substrate loaded with a 7 mg/cm^2 coating of ZnO tetrapods. The addition of the tetrapods brings about an increase of hydrophobic character as reflected by a ca. 20° increase of the contact angle. However, the surface remains oleophilic and the contact angle for heavy oil measured after 60 s is 0°, which corresponds to complete wetting and permeation of the oil droplets.[17] Figures V.3E and F illustrate water and heavy oil contact angles measured upon functionalization of the ZnO nanotetrapod surfaces with 1H,1H,2H,2H-perfluorooctanephosphonic acid, respectively. In addition to a further enhancement of the hydrophobicity, the surface is rendered superoleophobic with a heavy oil contact angle of 156±1°. Figure V.3G depicts a high-resolution digital photograph of water and heavy oil droplets placed on a homogenously coated stainless steel mesh. The image indicates that the water droplet is pinned only at a few points on the surface of the substrate corresponding to the protruding ZnO ends at the perimeter of the pores. Based on the morphology discernible in Figure V.2, coated mesh substrates offer a combination of micro- and nanoscale texturation that suspends the water droplets in the Cassie-Baxter regime. Figures V.3H and I indicate that the substrate acquires a shiny lustrous appearance upon immersion in water, which reflects the trapped air pockets enclosed by the tetrapodal structures. **Video A.2** (Supplementary Information) depicts the remarkable complete ejection of the substrate upon partial immersion in water, which reflects the high water repellency of these superhydrophobic substrates. The plastronic features result from the individual micron-sized pores being further interconnected by the tetrapodal structures at their periphery, which serve to yield an extended porous network. The trapped air renders the substrates buoyant over the span of several months without loss of water repellency. Unlike in the case of isolated plastronic pockets reported in the

literature,[19] the interconnected network of pores ensures that the plastrons are not destroyed upon immersion as long as a part of the substrate is not submerged. The plastronic architectures here are reminiscent of buoyant rafts formed by collectives of fire ants.[11] While one ant is hydrophobic and slightly buoyant, a collective of ants assembles to trap an array of plastrons that renders the resulting ensemble highly buoyant and difficult to submerge.[11] **Video A.3** (Supporting Information) depicts that water droplets impinging on the surface ricochet from the surface as a result of the high water repellency of the coated substrates.

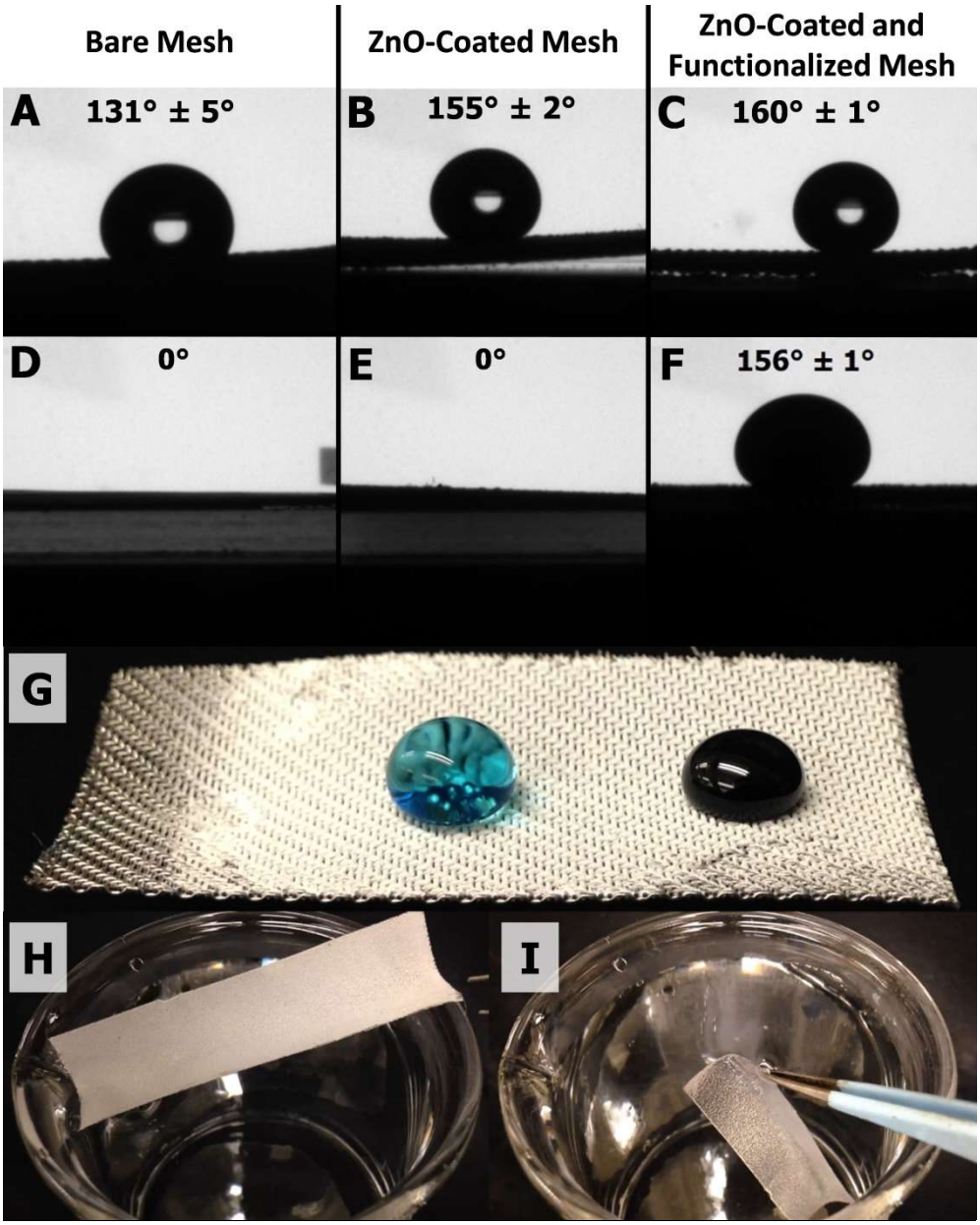

Figure V.3. Contact angles measured for A,D) a bare stainless steel mesh; B,E) stainless steel mesh with 7 mg/cm^2 of ZnO tetrapods; and C,F) the ZnO-coated mesh further functionalized with of 1H,1H,2H,2H-perfluorooctanephosphonic acid. The top images correspond to water contact angles, whereas the bottom images correspond to heavy oil contact angles. G) Digital photograph of water and sales oil droplets on a functionalized ZnO-coated mesh. Air pockets are discernible below the droplet. H, I) Digital photographs of a dry functionalized ZnO-coated mesh and a mesh immersed in water.

The surface functionalization of the ZnO tetrapods with 1H,1H,2H,2H-perfluorooctanephosphonic acid has been characterized by energy dispersive X-ray (EDX) spectroscopy, X-ray photoelectron spectroscopy, and Fourier transform infrared spectroscopy as depicted in **Figures V.4 and 5**. Figure V.4E depicts an EDX spectrum acquired for an individual tetrapod shown in Figure V.4A. EDX maps corresponding to characteristic fluorescent X-rays detected for Zn, O, and F are depicted as Figures V.4B-D and indicate localization of surface functionalization to the oxide tetrapodal surfaces. Homogeneous surface functionalization is detected within the limits of spatial resolution across the surface of the tetrapod.

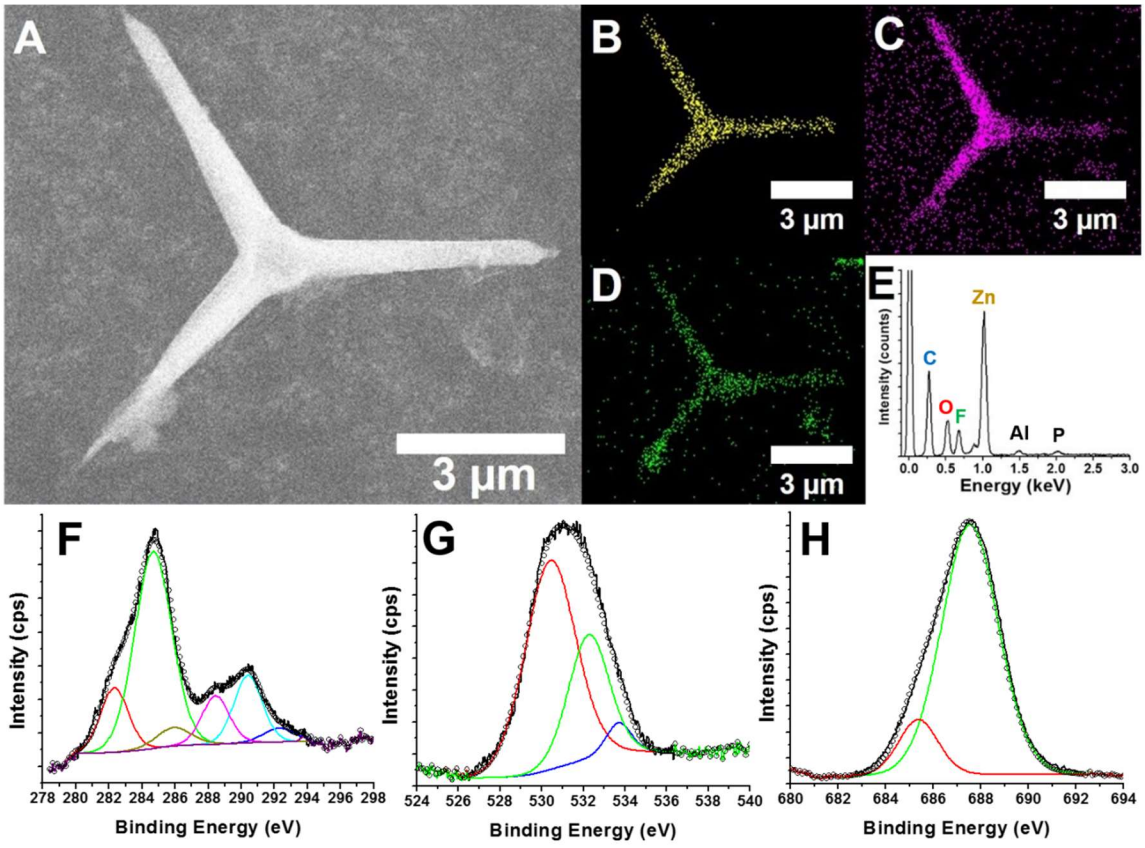

Figure V.4. SEM image depicting a single ZnO tetrapod functionalized with 1H,1H,2H,2H-perfluorooctanephosphonic acid (A) and corresponding EDX maps depicting the distribution of zinc (B), oxygen (O), and fluorine (D). E) Integrated EDX spectrum acquired for the tetrapod. (F) C 1s, (G) O 1s, and (H) F 1s high-resolution XPS spectra acquired for functionalized ZnO tetrapods.

Several distinct chemical bonding environments are discernible in high-resolution C1s XPS spectra acquired for the functionalized ZnO tetrapods. The feature centered at 284.8 eV arises from both adventitious hydrocarbons (inevitably physisorbed onto nanostructured surfaces exposed to ambient conditions and also observed prior to functionalization) and methylene carbons from the phosphonic acid ligand.[20,21] The feature centered at 285.9 eV can be assigned to both C—P and $–CH_2$ groups next to a $–CF_2$ group ($-CF_2—\mathbf{CH_2}-$).[20,21] The feature centered at 290.4 eV can be attributed to $–CF_2$ groups situated immediately adjacent to a $–CH_2$ group ($-\mathbf{CF_2}—CH_2-$). The feature centered at 292.5 eV can be attributed to $–CF_2$ groups adjacent to another $–CF_2$ group ($-\mathbf{CF_2}—CF_2-$). Finally, the feature centered at 293.8 eV can be attributed to $–CF_3$ groups next to a $–CF_2$ group ($-CF_2—\mathbf{CF_3}$).[22] The O 1s high-resolution XPS spectrum is characterized by three distinctive features. Features centered at 530.1 and 531.9 eV, which are also observed for the ZnO tetrapods prior to functionalization can be attributed to lattice oxygen atoms bonded to Zn atoms in the hexagonal zincite structure and to surficial oxygen from hydroxyl groups on ZnO, respectively.[21,23,24] Upon surface functionalization, a distinctive feature centered at 533.8 eV is observed and can be ascribed to **O**—P bonds of 1H,1H,2H,2H-perfluorooctanephosphonic acid bonded in a bidentate fashion to ZnO.[21] Figure V.1 depicts the bidentate coordination of the phosphonic acid to the ZnO surfaces. Figure V.4F shows F 1s XPS spectra acquired for the functionalized ZnO tetrapods (no fluorine is detectable prior to functionalization). The high-resolution F 1s XPS spectrum comprises a major feature at 687.7 eV, which can be attributed to fluorine atoms bonded to carbon in $–CF_2$ and $–CF_3$ groups of 1H,1H,2H,2H-perfluorooctanephosphonic acid,[22,25] analogous to values noted for spectra acquired for perfluorinated monolayers of phosphonic acids and thiols. A minor peak centered at 685.4 eV denotes the presence of inorganic fluoride impurities.[24,26,27]

Further analysis has been performed using FTIR spectroscopy to characterize the ordering of the functionalizing moiety on the ZnO surfaces. **Figure V.5** contrasts the FTIR ATR spectra of 1H,1H,2H,2H-perfluorooctanephosphonic acid functionalized ZnO tetrapods with that of the free phosphonic acid. The peaks observed at 1140 and 1232 cm^{-1} are suggestive of the ordering of perfluorinated groups forming a self-assembled monolayer on the tetrapod surfaces.[28–31] These two modes correspond to asymmetric CF_2 stretches perpendicular to the helical axis of fluoroalkanes that are ordered with a helical-tilt orientation.[28,29] Further corroboration of said helical configuration within the monolayers is derived from the observation of characteristic modes at 1325 and 1367 cm^{-1}, which confirm the presence of symmetrical CF_2 stretching parallel to the fluoroalkyl helical axis.[28–30] These values are indicative of the relatively close packing of the fluoroalkyl chains, which translates to a low surface energy and thus superhydrophobicity and superoleophobicity.[28,29] A band observed at 2947 cm^{-1} (**Figure A.8**, Supporting Information) is ascribed to asymmetric CH_2 stretching and is blue-shifted from the free acid[30–33] indicating that the CH_2 groups immediately adjacent to the phosphonic acid binding groups of the fluoroalkyl chains are less ordered.[32,33] The relatively large steric footprint of the phosphoryl binding groups likely restricts the packing of adjacent CH_2 groups. However, in stark contrast, the fluoroalkyl chains that are further away from the phosphoryl binding groups can interact to form helical assemblies such as depicted in the inset of Figure IV.5.[33] Notably, the retention of helical self-assembly of perfluorinated groups on surfaces presenting re-entrant curvature has not hitherto been observed to the best of our knowledge. Bands observed at 951, 955, and 1011 cm^{-1} are furthermore observed, which are ascribed to P-O and P-OH stretching.[30,34] A broad band discernible in the 2100—3100 cm^{-1} range is characteristic of $(OH)_2P{=}O$ groups (**Figure A.9**, Supporting Information).[34]

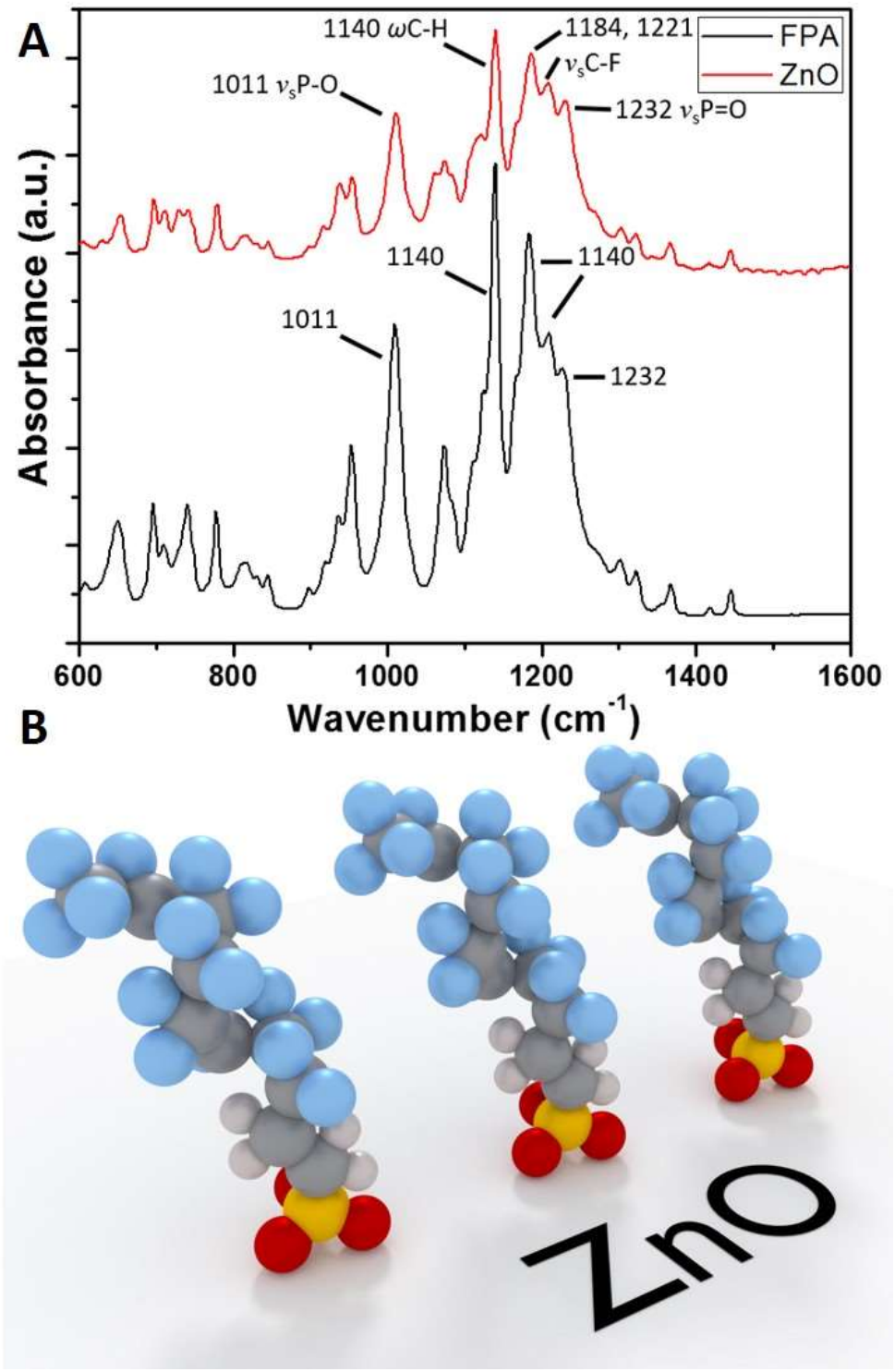

Figure V.5. (A) FTIR ATR spectra (A) of 1H,1H,2H,2H-perfluorooctanephosphonic acid (black) and 1H,1H,2H,2H-perfluorooctanephosphonic acid functionalized ZnO tetrapods (red). (B) A representation of the helical structure of 1H,1H,2H,2H-perfluorooctanephosphonic acid attached to ZnO.

Thermogravimetric analysis of the coating systems performed in air suggest that the ZnO tetrapods maintain their structural integrity to temperatures of 900°C, whereas for the perfluorinated systems, degradation is initiated at ca. 295°C, well above typical handling temperatures for heavy oils.

The combination of a low surface energy result from stabilization of a well-ordered helical perfluorinated monolayer and hierarchical nanoscale and microscale texturation yields a surface that is very difficult to wet as indicated by the remarkable rejection of water manifested in Videos A.2 and A.3 (Supporting Information) and the superoleophobicity observed in Figure IV.3G. The ability to repel low surface tension hydrocarbons is particularly remarkable since the lower cohesive forces in these liquids gives rise to a much larger predilection for surface wetting (adhesive interfacial forces can readily overcome the weak van der Waals' cohesive forces in liquid hydrocarbons).

In the Cassie—Baxter formalism of suspended water droplets (Fig. IV.3G),[35] the effective contact angle θ_c is denoted as:

$$cos\theta_c = f_s(cos\theta_e + 1) - 1 \qquad \text{(V.1)}$$

where f_s is the fraction of the solid that touches the liquid and Θ_e is the equilibrium contact angle for a flat substrate. The nanotextured geometry and the presence of large micron-sized pores that trap air greatly reduces the available area for solid—liquid contact. While this alone is sufficient to suspend water droplets, the interfacial area is still large enough to allow for lower surface tension oil to wet the surface (contrast Fig. IV.3B and 3E). A further increase of the equilibrium contact angle thus needs to be brought about by functionalization with a fluorous phase, which reduces the solid/vapor and increases the solid/liquid interfacial energies in Eq. V.2

$$cos\theta_e = \frac{\gamma_{SV} - \gamma_{SL}}{\gamma_{LV}} \quad \text{(V.2)}$$

where γ terms are the interfacial energies for the solid–vapor (SV), solid–liquid (SL), and liquid–vapor (LV) surfaces.

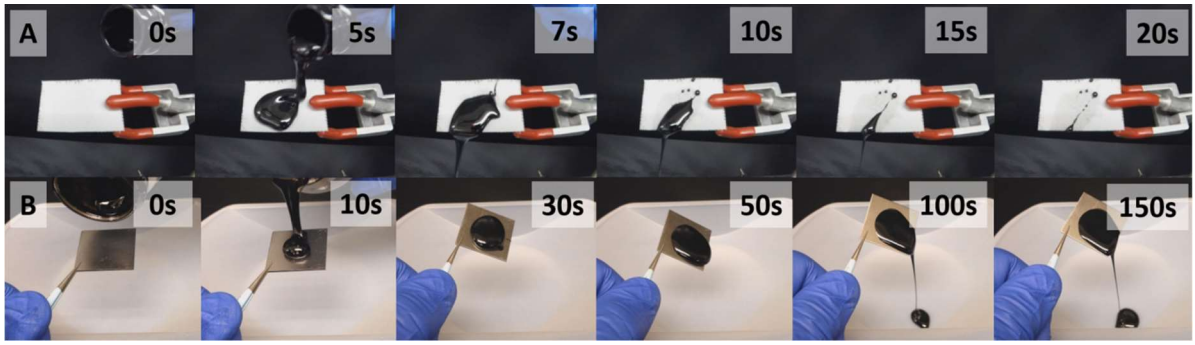

Figure V.6. Time lapse images of heavy oil droplets placed on a (A) ZnO-coated and fluorinated mesh contrasted to (B) images acquired for untreated mesh substrate. Video A.4 (Supporting Information) illustrates the stark contrast between these samples.

The implications of the greatly diminished wettability achieved here for handling of heavy oils is illustrated in **Figure V.6A** depicts a sequence of time lapse digital photographs when viscous heavy oil is poured onto a coated substrate with a pore size of *ca.* 180 μm and a loading of 7 mg/cm^2. Remarkably, within a period of 20 s, the viscous oil entirely glides off the tilted surface, whereas for an uncoated mesh substrate, Figure V.6B depicts that most of the heavy oil is retained on the surface. **Video A.4** (Supporting Information) contrasts the behavior of heavy oil droplets poured onto coated and uncoated substrates. The facile gliding of viscous heavy oils has heretofore not been demonstrated. The heavy oil droplets glide readily since the contact radius of the droplets is greatly diminished, reducing their adhesion to the surface and allowing gravity to facilitate downwards flow.

V.5 Conclusions

A robust inorganic surface has been designed comprising stainless steel mesh substrates with periodic micron-sized pores coated with nanoscale ZnO tetrapods, yielding a biomimetic plastronic architecture trapping a continuous interconnected network of air pockets. The helical self-assembly of a perfluorinated phosphonic acid on the tetrapodal surfaces serves to further reduce the surface energy of the system. The resulting coating system yields unprecedented water and heavy oil contact angles of 160°±1° and 156°±1°, respectively. The substrates are strongly ejected upon immersion in water and demonstrate bouncing of water droplets and gliding of viscous heavy oil droplets. The remarkable ability of this coating system to simultaneously glide water and viscous heavy oils along with the high thermal stability of these systems renders these materials viable for handling of unconventional bitumen and dense hydrocarbons with challenging rheological properties. Such coating systems are potentially useful for deployment in railroad cars, pipelines, and other oil-handling equipment where they are expected to greatly facilitate cleaning and reduce transportation losses. Additionally, the same principles applied in Chapter V are further explored in Chapter VI where another inorganic surface comprised of TiO_2 with multiscale texturation utilizes perfluorinated phosphonic acid to demonstrate the gliding of oil and water.

V.6 Associated Content

Supporting Information is available free of charge via the Internet at http://pubs.acs.org. Videos depicting the ejection of coated substrates upon immersion in water; ricocheting of water droplets on water substrate; and comparison of gliding of heavy oil droplets on coated and functionalized as compared to uncoated substrates. FTIR spectrum of 1H,1H,2H,2H-

perfluorooctanephosphonic acid and 1H,1H,2H,2H-perfluorooctanephosphonic acid functionalized ZnO tetrapods.

V.7 References

(1) Shah, A.; Fishwick, R.; Wood, J.; Leeke, G.; Rigby, S.; Greaves, M. *Energy Environ. Sci.* **2010**, *3* (6), 700.

(2) Butler, R. M. *Thermal Recovery of Oil and Bitumen*; Prentice Hall Inc.: Old Tappan, 1991.

(3) Canada National Energy Board. *Canada's Oil Sands Opportunities and Challenges To 2015: An Update*; 2006.

(4) Rana, M. S.; Sámano, V.; Ancheyta, J.; Diaz, J. A. I. *Fuel* **2007**, *86* (9 SPEC. ISS.), 1216–1231.

(5) Upreti, S. R.; Lohi, A.; Kapadia, R. A.; El-Haj, R. *Energy and Fuels* **2007**, *21* (3), 1562–1574.

(6) O'Loughlin, T. E.; Waetzig, G. R.; Davidson, R. E.; Dennis, R. V.; Banerjee, S. *Encycl. Inorg. Bioinorg. Chem.* **2017**, p 1, DOI: 10.1002/9781119951438.eibc2493.

(7) Neinhuis, C.; Barthlott, W. *Ann. Bot.* **1997**, *79* (6), 667–677.

(8) Barthlott, W.; Neinhuis, C. *Planta* **1997**, *202* (1), 1–8.

(9) Shirtcliffe, N. J.; McHale, G.; Newton, M. I.; Perry, C. C.; Pyatt, F. B. *Appl. Phys. Lett.* **2006**, *89* (10), 10–12.

(10) Balmert, A.; Florian Bohn, H.; Ditsche-Kuru, P.; Barthlott, W. *J. Morphol.* **2011**, *272* (4), 442–451.

(11) Mlot, N. J.; Tovey, C. a; Hu, D. L. *Proc. Natl. Acad. Sci. U. S. A.* **2011**, *108* (19), 7669–7673.

(12) Brewer, S. A.; Willis, C. R. *Appl. Surf. Sci.* **2008**, *254* (20), 6450–6454.

(13) Flynn, M. R.; Bush, J. W. M. *J. Fluid Mech.* **2008**, *608* (Wenzel 1936), 275–296.

(14) Tuteja, A.; Choi, W.; Ma, M.; Mabry, J. M.; Mazzella, S. A.; Rutledge, G. C.; McKinley, G. H.; Cohen, R. E. *Science (80-.).* **2007**, *318* (5856), 1618–1622.

(15) Pan, S.; Kota, A. K.; Mabry, J. M.; Tuteja, A. *J. Am. Chem. Soc.* **2013**, *135* (2), 578–581.

(16) Velazquez, J. M.; Gaikwad, A. V.; Rout, T. K.; Rzayev, J.; Banerjee, S. *ACS Appl. Mater. Interfaces* **2011**, *3* (4), 1238–1244.

(17) O'Loughlin, T. E.; Martens, S.; Ren, S. R.; McKay, P.; Banerjee, S. *Adv. Eng. Mater.* **2017**, *19* (5), 1600808.

(18) Sinkovits, D. W.; Luijten, E. *Nano Lett.* **2012**, *12* (4), 1743–1748.

(19) Poetes, R.; Holtzmann, K.; Franze, K.; Steiner, U. *Phys. Rev. Lett.* **2010**, *105* (16), 1–4.

(20) Tan, J.; Fessehaie, M.; J, S. L. S. **1993**, *9* (3), 740–748.

(21) Timpel, M.; Nardi, M. V.; Krause, S.; Ligorio, G.; Christodoulou, C.; Pasquali, L.; Giglia, A.; Frisch, J.; Wegner, B.; Moras, P.; Koch, N. *Chem. Mater.* **2014**, *26* (17), 5042–5050.

(22) Paniagua, S. A.; Hotchkiss, P. J.; Jones, S. C.; Marder, S. R.; Mudalige, A.; Marrikar, F. S.; Pemberton, J. E.; Armstrong, N. R. *J. Phys. Chem. C* **2008**, *112* (21), 7809–7817.

(23) Park, Y. O.; Masel, R. I. *Surf. Sci. Lett.* **1983**, *131*, 385–389.

(24) National Institute of Standards and Technology. NIST X-ray Photoelectron Spectroscopy Database, Version 4.1 http://srdata.nist.gov/xps/. (accessed Jan 1, 2017).

(25) Zenasni, O.; Marquez, M. D.; Jamison, A. C.; Lee, H. J.; Czader, A.; Lee, T. R. *Chem. Mater.* **2015**, *27* (21), 7433–7446.

(26) Ro, C.; Linton, R. *Surf. Sci. Spectra* **1992**, *1* (3), 277.

(27) Kutsuna, S.; Nagaoka, Y.; Takeuchi, K.; Hori, H. *Environ. Sci. Technol.* **2006**, *40* (21),

6824–6829.

(28) Lenk, T. J.; Hallmark, V. M.; Hoffmann, C. L.; Rabolt, J. F.; Castner, D. G.; Erdelen, C.; Ringsdorf, H. *Langmuir* **1994**, *10* (12), 4610–4617.

(29) Shaporenko, A.; Cyganik, P.; Buck, M.; Ulman, A.; Zharnikov, M. *Langmuir* **2005**, *21* (18), 8204–8213.

(30) Silverstein, R. M.; Clayton Bassler, G.; Morris, T. C. *Spectrometric identification of organic compounds*, 6th ed.; Wiley, 1980.

(31) Lambert, J. B.; Shurvell, H. F.; Lightner, D. A.; Cooks, R. G. *Organic Structural Spectroscopy*; Prentice Hall, 1998.

(32) Luscombe, C. K.; Li, H.; Huck, W. T. S.; Holmes, A. B. *Langmuir* **2003**, *19* (13), 5273–5278.

(33) Markovich, I.; Mandler, D. *J. Electroanal. Chem.* **2001**, *500* (1), 453–460.

(34) Danilich, M. J.; Burton, D. J.; Marchant, R. E. *Vib. Spectrosc.* **1995**, *9* (3), 229–234.

(35) Cassie, A. B. D.; Baxter, S. *Trans. Faraday Soc.* **1944**, *40* (5), 546–551.

CHAPTER VI

OUTLOOK, SUMMARY, AND OTHER STRATEGIES

VI.1 Introduction

Difficulties with transportation and handling of heavy viscous oil and bitumen (accessed using enhanced oil recovery methods in the Alberta Oil Sands) are directly attributable to their challenging rheological characteristics and contribute greatly to overall production costs. A tremendous challenge is the design of surfaces that are not wetted by viscous oils and allow for the facile gliding of these fluids, as discussed previously in Chapters IV and V. Such surfaces could greatly mitigate the need for dilution with lighter molecular mass hydrocarbons (diluent) as is the current practice to facilitate transportation. Diluent availability constraints have previously inspired efforts to reduce costs thought the development of techniques such as blending high gravity synthetic crude oil with raw bitumen (SynBit).[1] Reliance on diluent reduces capacity of pipelines; indeed, an estimated 15% of existing capacity is used just to flow diluent across North America. This represents a significant inefficiency and is a considerable cost burden on heavy oil producers.[1–3] The surface wetting characteristics of heavy oil further give rise to considerable amounts of retained liquids and surface fouling, thereby necessitating maintenance costs pertaining to flushing of pipelines and scrubbing of rail cars; the accumulation of deposits (such as from asphaltene precipitation) in constricted regions of tubing furthermore represents a major maintenance challenge with grave safety and cost implications. The ability to glide heavy oil droplets will open up alternative modes of transportation, greatly diminish maintenance needs, and reduce energy costs of transportation if pressure drops and friction losses across pipelines can be reduced. In this concluding chapter, I discuss an alternative colloidal crystal templating strategy for inducing nanotexturation based on sacrificial elimination of

polystyrene sphere templates. Functionalization of such surfaces with a perfluorinated phosphonic acid yields surfaces exhibiting hitherto unprecedented gliding of viscous oil droplets. The facile spray coating application of a highly textured coating has potential for application at scale.

A primary application for omniphobic surfaces is expected to be within pipelines wherein they can reduce frictional losses and by serving as effective barriers dimnigh corrosion. Several experimentally accessible quantities provide a measure of the extent to which a liquid wets a surface and the resistance to fluid flow. Contact and tilt angles provide a local measurement of the balance between cohesive and adhesive forces. When the former exceeds the latter, the liquid droplet is unable to completely wet the surface defining a high contact angle, which is often used as a proxy for the affinity (or lack thereof) of the liquid towards the surface. Liquid droplets are nevertheless often pinned to specific regions of the surface; the tilt angle describes the perturbation required to induce gliding of the droplet. In other words, the contact angle is a very local measure of liquid—surface interactions, whereas the tilt angle provides a better measure of fluid flow. However, a far global metric that is relevant to design of flow systems is the pressure drop as measured under different (laminar or turbulent) flow conditions. The frictional dissipation and pressure drop across a straight section of tubing as evaluated using Bernoulli's formalism allows for characterization of frictional losses across the section, thereby providing a more direct measure of resistance to fluid flow. An apparatus for measuring frictional losses has been designed and will provide a means of evaluating the efficacy of the omniphobic coatings discussed in Chapters IV, V as well as subsequent sections of this chapter in mitigating frictional losses.

VI.2 Experimental Methods for Preparation of Colloidally Templated TiO_2 Surfaces

VI.2.1 Preparation of Polystyrene Spheres

Polystyrene (PS) microspheres were synthesized based on a modified dispersion polymerization approach.[4,5] Briefly, 17 mL of styrene, 1.5 g of 40,000 MW poly(vinylpyrrolidone) and 98 mL of anhydrous ethanol were added to a three neck round bottom flask. The solution was stirred at 200 rpm and kept at a constant temperature of 70° C while nitrogen was bubbled into the system. After 30 minutes nitrogen bubbling was stopped, 0.15 g of 2,2′-azobis(2- methylpropionitrile) in 28 mL of ethanol was added to the flask and the system was allowed to react for 24 hours. The synthesized microspheres were then centrifuged at 10,000 rpm for 15 minutes and washed with ethanol three times. Stocks of 4% w/w of polystyrene/ethanol mixtures were prepared. The nominal diameter of the PS microspheres were approximately 2.4 μm.

VI.2.2 Fabrication of TiO_2 Coatings

In a typical process, coatings were prepared by combining 7.5 wt.% 1500 nm TiO_2 (US Research Nanomaterials, Inc) and deionized water with an aliquot of the prepared polystyrene (4.1 wt.%) in ethanol solution with a ratio of 1:1 (w/w) of TiO_2 colloidal dispersion: polystyrene colloidal dispersion. The mixture was then agitated and spray coated directly onto cleaned A36 steel substrates 1” by 1” on a hot plate set to approximately 200°C. The steel was cleaned with hexane, ethanol, 1 wt.% Alconox^{TM} solution, and deionized water prior to coating. The polystyrene serving as a sacrificial template was removed upon annealing of the coated substrates at 400°C for 2 h.

VI.2.3 Characterization

Contact angles were measured with a CAM 200 Optical Goniometer where a mechanical pipet dispensed doubly distilled and deionized water (ρ = 18.2 MΩ cm^{-}1) of ca. 10 µL. Viscous oil was applied using a manual micropipette and was supplied by Cenovus Energy, Inc. The viscous oil was extracted using steam-assisted gravity drainage method in the Northern Alberta Oil Sands and it has a viscosity of ca. 210 mPa·s at 25 °C. The reported contact angles are an average of at minimum three measurements taken across the substrate.

The morphology of the colloidally templated TiO_2 structures were imaged using a JEOL JSM-7500F field-emission scanning electron microscope (FE-SEM) equipped with a high brightness conical FE gun and a low aberration conical objective lens. A cold cathode UHV field emission conical anode gun was used as the source. Micrographs were collected at an accelerating voltage of 5 kV with resolution of *ca*. 1.0 nm.

VI.3 Colloidally Templated TiO_2 Coated Surfaces: A Potential Addition to the Omniphobic Toolkit

Engineering oleophobic surfaces requires a combination of reentrant curvature, low surface energy, and multiscale texturation.[6,7] To realize such surfaces, polystyrene spheres have been used as sacrificial templates to prepare textured TiO_2 surfaces that exhibit concurrent superhydrophobic and superoleophobic properties. The use of an appropriate ratio of polystyrene spheres and TiO_2 nanoparticles allows for considerable control over surface texturation.[8,9] The mixture of spheres are sprayed onto substrates followed by elimination of the polystyrene spheres by thermal annealing. The resulting structures demonstrate mesoscale topography comprising micron-scale pores and nanoscale TiO_2 particles (**Figure VI.1**). In order to evaluate

the influence of the specific pore dimensionality on wettability, water and oil contact angles have been evaluated as a function of the TiO_2 particle size while keeping the TiO_2:polystyrene ratio constant at 1:1 (w/w). Figure VI.1 demonstrates the topographical differences induced upon varying the size of TiO_2 nanoparticles from 40 nm—1500 nm while keeping the relative ratio of TiO_2 nanoparticles:PS spheres constant at 1:1 (w/w).

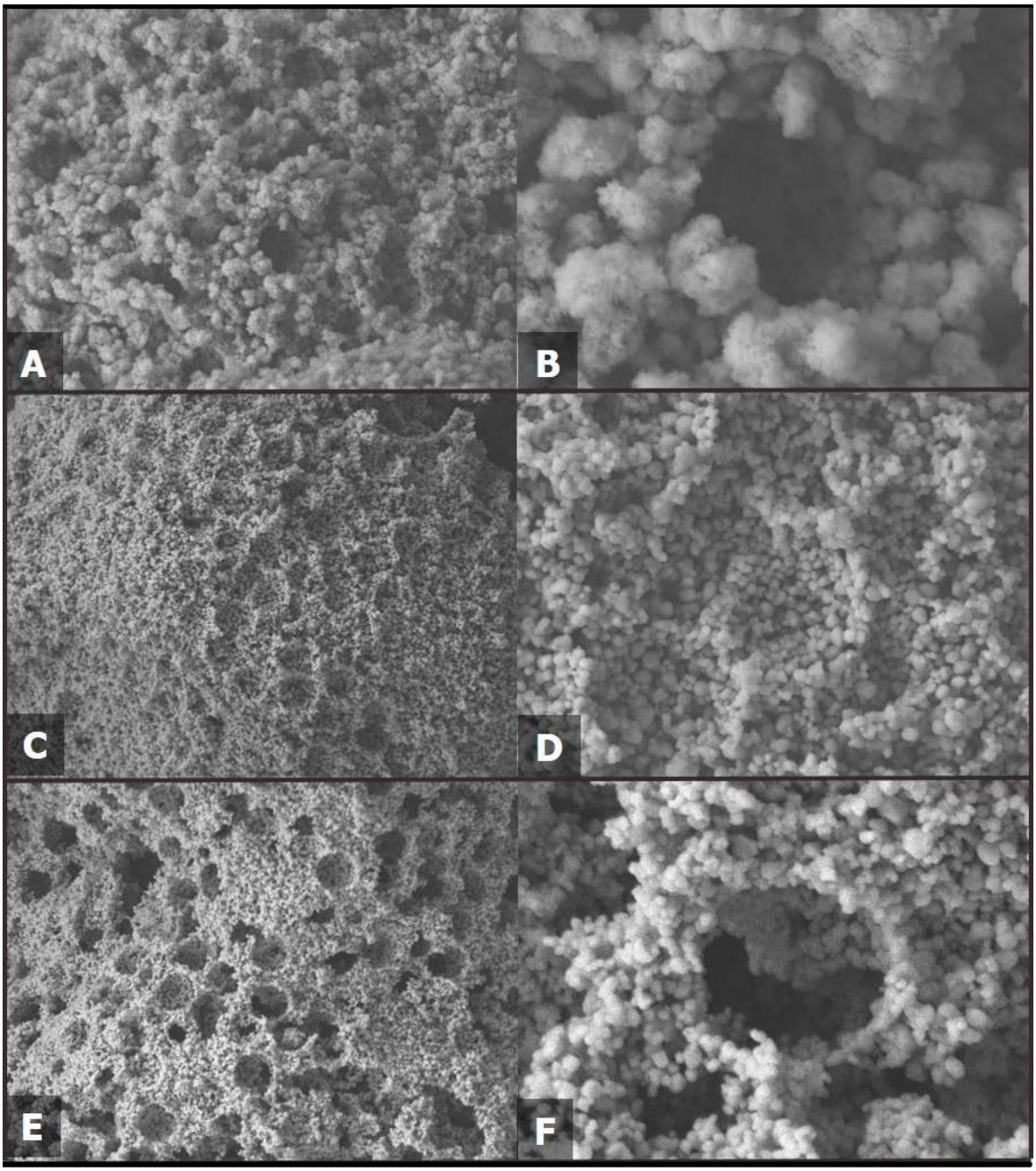

Figure VI.1. Scanning electron microscopy images of templated 40 nm (A, B), 800 nm (C, D), and 1500 nm (E, F) TiO_2 nanoparticles with microscale pores that have been generated by the permeation of TiO_2 particles within interstitial domains of inverse opal structures constituted from polystyrene spheres, followed by subsequent removal of polystyrene spheres upon annealing of the coated substrates at 400°C for 2 h. The relative ratio of TiO_2 nanoparticles:PS spheres was maintained at a constant at 1:1 (w/w).

In addition to a high degree of texturation, generation of oleophobic surfaces also require a drastic reduction in surface energy. After the steel substrates were coated with TiO_2, their surface energy was greatly reduced with the functionalization of 1H,1H,2H,2H perfluorooctane phosphonic acid. This treatment was selected due to the compound's ability to form a densely packed self-assembling monolayer (SAM) and its characteristically strong affinity to bind to metal oxide surfaces, as noted in Chapters IV and V. In this chapter we note that after a treatment *via* immersion in a 2.7 mM solution of 1H,1H,2H,2H perfluorinated phosphonic acid (THF as solvent) for 1 h, the surfaces were rendered omniphobic, repelling both water and viscous oil. To quantitate the results, contact angles were obtained for the three selected particle sizes. The texturation (observed from micrographs in Figure VI.1) combined with the reduced surface energy after functionalization consistently produced omniphobic surfaces across all selected TiO_2 particle sizes, as indicated in **Figure VI.2.** This figure shows contact angles for 40 nm templated TiO_2 nanoparticles of 165° ± 4° and 143° ± 6° (Figure VI.2 A, B) for water and viscous oil, respectively; contact angles of 160° ± 4° and 152° ± 6° are measured for water and viscous oil, respectively, for templated assemblies constituted from 800 nm TiO_2 nanoparticles (Figure VI.2 C, D); and finally, contact angles of 164° ± 5° and 161° ± 2° have been observed for water and viscous oil, respectively for templated thin films comprising 1500 nm TiO_2 nanoparticles, (Figure VI.2 E, F). Based on these observations and considering that larger particle sizes become considerably more polydisperse, 1500 nm TiO_2 nanoparticles have been down selected for further evaluation of optimal loading ratios. Figure VI.2 demonstrates the remarkable oleophobic behavior of these configurations, which yield contact angles in excess of 160° and readily manifest the gliding of viscous oil.

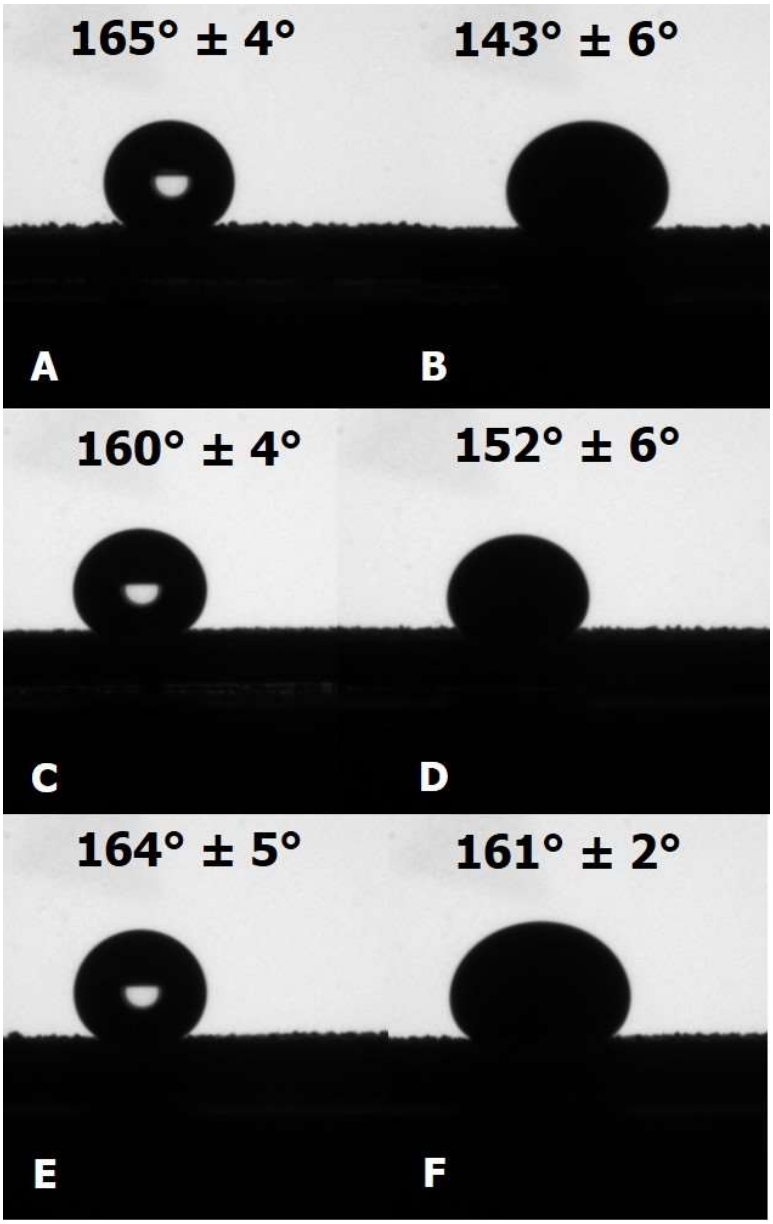

Figure VI.2. Contact angles for water (A) and viscous oil (B) on templated TiO_2 nanoparticle coatings built from 40 nm TiO_2 particles, water (C) and viscous oil (D) on templated TiO_2 nanoparticle coatings built from 800 nm TiO_2 particles, and water (E) and viscous oil (D) on templated TiO_2 nanoparticle coatings built from 1500 nm TiO_2 particles. All surfaces were made with 1:1 (w/w) TiO_2:polystyrene coatings on A36 steel substrates and subsequently treated with 2.7 mM 1H,1H,2H,2H perfluorooctane phosphonic acid for a period of 1 hour.

In attempts to increase the extent of texturization and thereby potentially the omniphobicity of the colloidally templated surfaces, the relative ratios of TiO_2 particles:polystyrene spheres has been adjusted in order to tune the porosity of the surfaces. In order to observe the differences in topography, scanning electron microscopy imahes have been collected for various ratios of TiO_2 particles:polystyrene spheres, while keeping the particle size constant at 1500 nm, as demonstrated in **Figure VI.3**. It is worth noting that all of the surfaces were prepared using polystyrene spheres that are approximately 2.5 μm in diameter. In addition to evaluation of texturation by scanning electron microscopy, the evolution of the water and oil contact angles as a function of the relative ratio of TiO_2 particles to polystyrene spheres has examined using measurements of water and viscous oil contact angles.

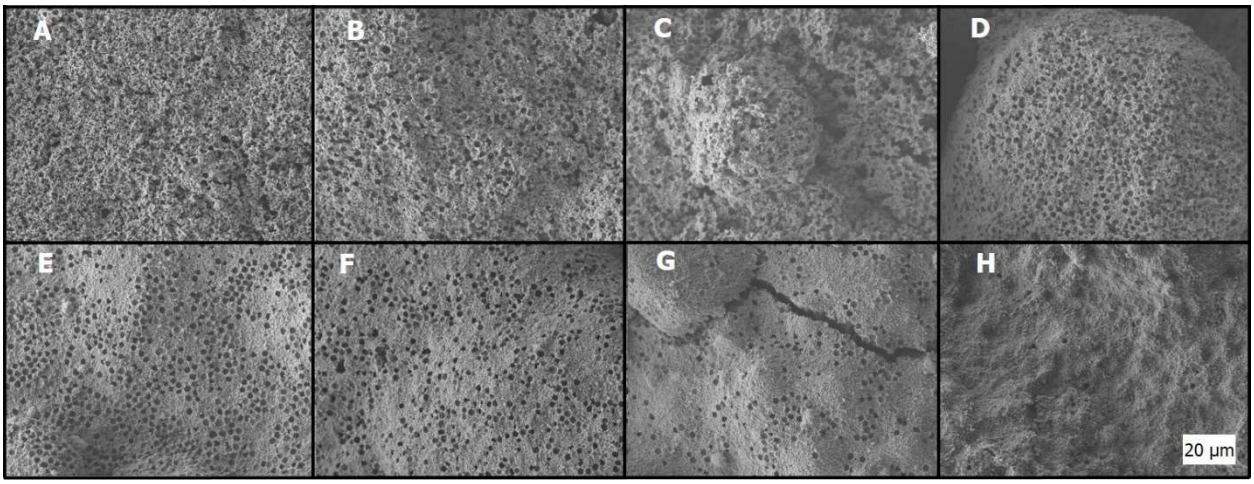

Figure VI.3. Scanning electron microscopy images of different ratios of TiO_2 nanoparticles: polystyrene spheres examined at different loading ratios: 9:1 (A), 8:2 (B), 7:3 (C), 6:4 (D), 4:6 (E), 3:7 (F), 2:8 (G), and 1:9 (H). The particles have been templated onto A36 steel substrates in each case.

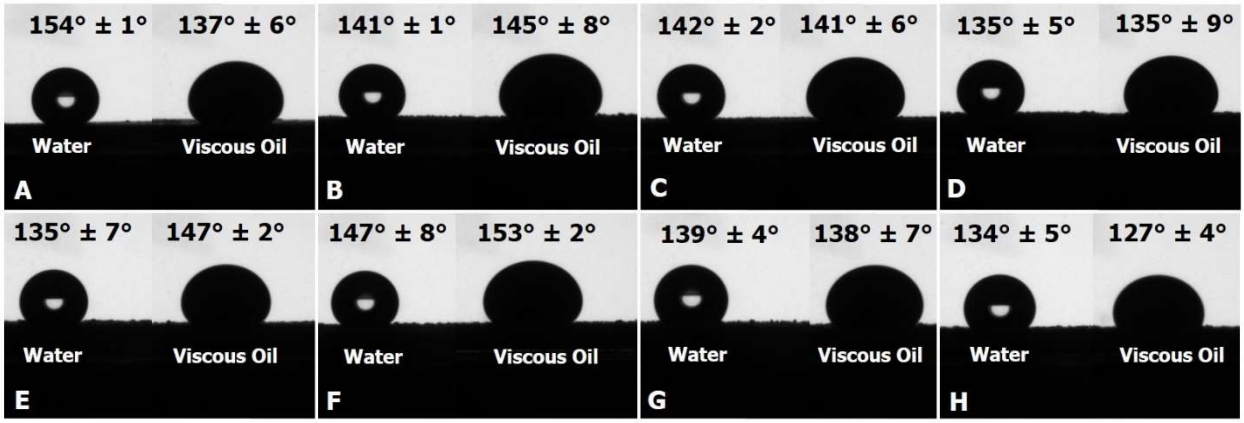

Figure VI.4. Contact angles for water and viscous oil of 9:1 (A), 8:2 (B), 7:3 (C), 6:4 (D), 4:6 (E), 3:7 (F), 2:8 (G), and 1:9 (H) TiO_2:polystyrene (w/w) templated into A36 steel substrates. All substrates were treated by soaking in a 2.7 mM 1H,1H,2H,2H perfluorooctane phosphonic acid solution for 1 hour.

Despite the superhydrophobic and superomniphobic contact angles and the facile gliding of heavy oil droplets, the extent of adhesion on planar steel substrates is relatively low, approaching *ca*. 50—100 g in scrape adhesion tests. Additional screenings to increase the adhesion strength are required, with one promising candidate being the application of $Ti(O^iPr)_4$ to form oxo linkages. With the use of titanium isopropoxide, it may be possible to increase adhesion strength while preserving the surface chemistry by forming an amorphous TiO_2 layer. With the addition of this powerful colloidal templating strategy to our toolkit of ZnO coated surfaces described in Chapters IV and V, pipelines with omniphobic surfaces may soon come to fruition.

VI.4 Future Outlook: Pipeline Coatings

VI.4.1 Methodology

In addition to the colloidally templated TiO_2 coatings discussed in the preceding section, the availability of ZnO tetrapods arrayed onto stainless steel mesh substrates and functionalized with

helically ordered self-assembled monolayers of perfluorinated phosphonic acid as noted in Chapters IV and V provides an excellent system for further evaluation from a pipeline perspective. As previously mentioned, these coatings are compatible with spray processes, which will facilitate the coating of tubular samples. These structures give rise to a quasi-continuous network of air pockets akin to plastrons, which allow them to readily glide heavy oil droplets and strongly reject water droplets. Figure V.2 illustrates that water contact angles of 160° and viscous oil contact angles of 156° have been achieved along with rapid gliding of heavy oil (Video A.4) for a ZnO tetrapod coated stainless steel mesh with a pore size of *ca.* 180 μm and a ZnO loading of 7 mg/cm^2, which has been treated by soaking in a 2.7 mM 1H,1H,2H,2H perfluorooctane phosphonic acid for 1 hour.

Two distinct methods for coating tubing interiors (either with TiO_2 or ZnO) are envisioned. In one approach, planar substrates will be coated using spray deposition (or electroless plating of metallic thin films) and then rolled and welded (**Figure VI.3, Method I**). In a second approach, a lathe-based spray coating method can be implemented inside the tube (**Figure VI.3, Method II**). In both cases, the surfaces of the coatings can be functionalized with a perfluorinated compound by immersion in a solution of the appropriate precursor (such as perfluorinated phosphonic acid, perfluorinated butyric acid, or potassium perfluorooctane sulfonate).

Initial characterization will be performed by using cross-sectional scanning electron microscopy (after first sectioning the samples); water and viscous oil contact angle measurements, and standardized ASTM tests of adhesion (the latter can be performed for planar substrates, examples of ASTM tests include methods D3359 and D2197). A series of coated and functionalized tubes with varying coating thicknesses will be prepared by the methods described above for use in fluid flow measurements. Multiple replicates will be performed to ensure reproducibility and

establish sufficient statistics for analysis in such measurements, thereby allowing for systematic pressure and flow rate correlations.

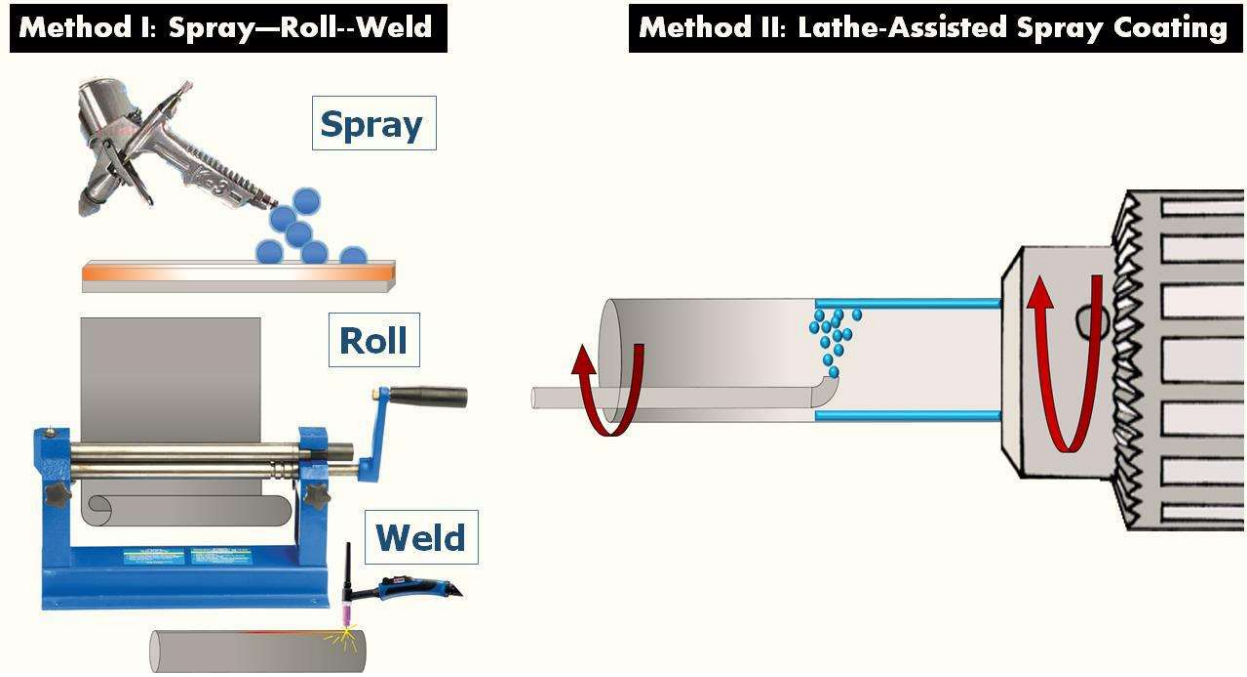

Figure VI.5. Schematic depictions of two methods for the application and construction of coated pipelines.

VI.4.2 Constructing and Benchmarking of an Apparatus for Testing of Fluid Flow

An apparatus for flow characterization in straight tubing sections has been constructed comprising the following components: (i) a variable speed pump; (ii) a fluid reservoir; (iii) a straight tubing section (where components constructed in Task 1 can be tested); (iv) inline liquid flowmeter; (v) multiple pressure gauges; (vi) fluid flow valves; and (vii) sundry pipe joints and fittings. The flow behavior across this unit can be benchmarked using uncoated tubing of different types at various flow conditions using a number of different test liquids, such as water and viscous oil.

VI.4.3 Measurement of Pressure Drops across Coated Tubes

Appropriately positioned pressure gauges will be used to characterize pressure drops across straight sections of tubing coated and functionalized as noted in Chapter VI.3. Pressure drops will be measured for deionized water and viscous oil as a function of the flow rate. The evolution of the pressure drop across the tubing section will also be monitored as a function of time to ensure that sloughing of the coating or accumulation of surface debris does not give rise to increased resistance. Such a system is schematically represented in **Figure VI.6.** Utilizing such a setup, the resistance to flow at different flow rates will be calculated for the different omniphobic coating formulations developed in this dissertation.

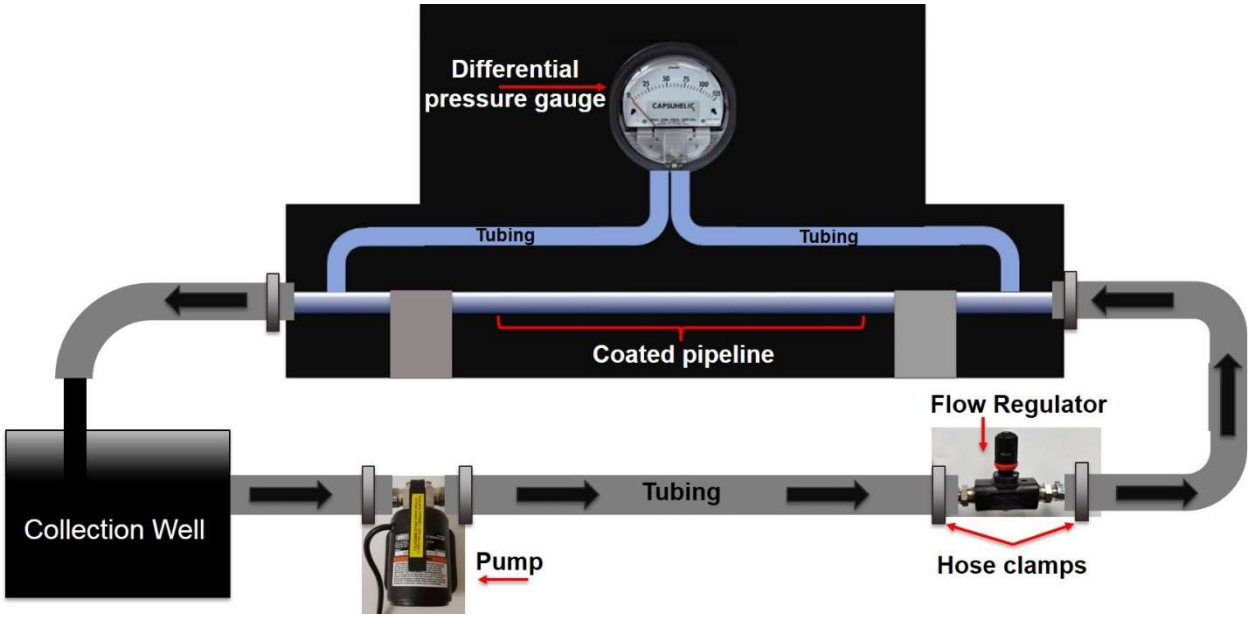

Figure VI.6. Schematic representation of a possible flow system to be used for pressure drop measurements across a coated pipeline.

The measured resistance to flow will be correlated to (i) active particle loading within the coating (the loading of ZnO/TiO_2); (ii) surface functionalization; and (iii) coating homogeneity. It will be intriguing to examine the extent to which values such as contact and tilt angles serve as predictors of the pressure drop and resistance to fluid flow. The development of such correlations will iteratively inform the design of next-generation omniphobic coatings, bringing about a transformative change in the transportation of hydrocarbons across North America.

VI.5 References

(1) Dusseault, M. B.; ShafieiI, A. In *Ullmann's Encylopedia of Industrial Chemistry*; 2011; Vol. 25, pp 263–314.

(2) Shah, A.; Fishwick, R.; Wood, J.; Leeke, G.; Rigby, S.; Greaves, M. *Energy Environ. Sci.* **2010**, *3* (6), 700–714.

(3) Alberta Energy Regulator. *Alberta's Energy Reserv. 2014 Supply/Demand Outlook* **2015**, 299.

(4) Song, J. S.; Winnik, M. A. *Macromolecules* **2005**, *38* (20), 8300–8307.

(5) Li, F.; Geng, C.; Yan, Q. *J. Polym.* **2013**, *2013*, 1–7.

(6) Tuteja, A.; Choi, W.; Ma, M.; Mabry, J. M.; Mazzella, S. A.; Rutledge, G. C.; McKinley, G. H.; Cohen, R. E. *Science (80-.).* **2007**, *318* (5856), 1618–1622.

(7) Pan, S.; Kota, A. K.; Mabry, J. M.; Tuteja, A. *J. Am. Chem. Soc.* **2013**, *135* (2), 578–581.

(8) Stein, A.; Wilson, B. E.; Rudisill, S. G. *Chem. Soc. Rev.* **2013**, *42* (7), 2763–2803.

(9) Iskandar, F.; Nandiyanto, A. B. D.; Yun, K. M.; Hogan, C. J.; Okuyama, K.; Biswas, P. *Adv. Mater.* **2007**, *19* (10), 1408–1412.

APPENDIX A

FIGURES

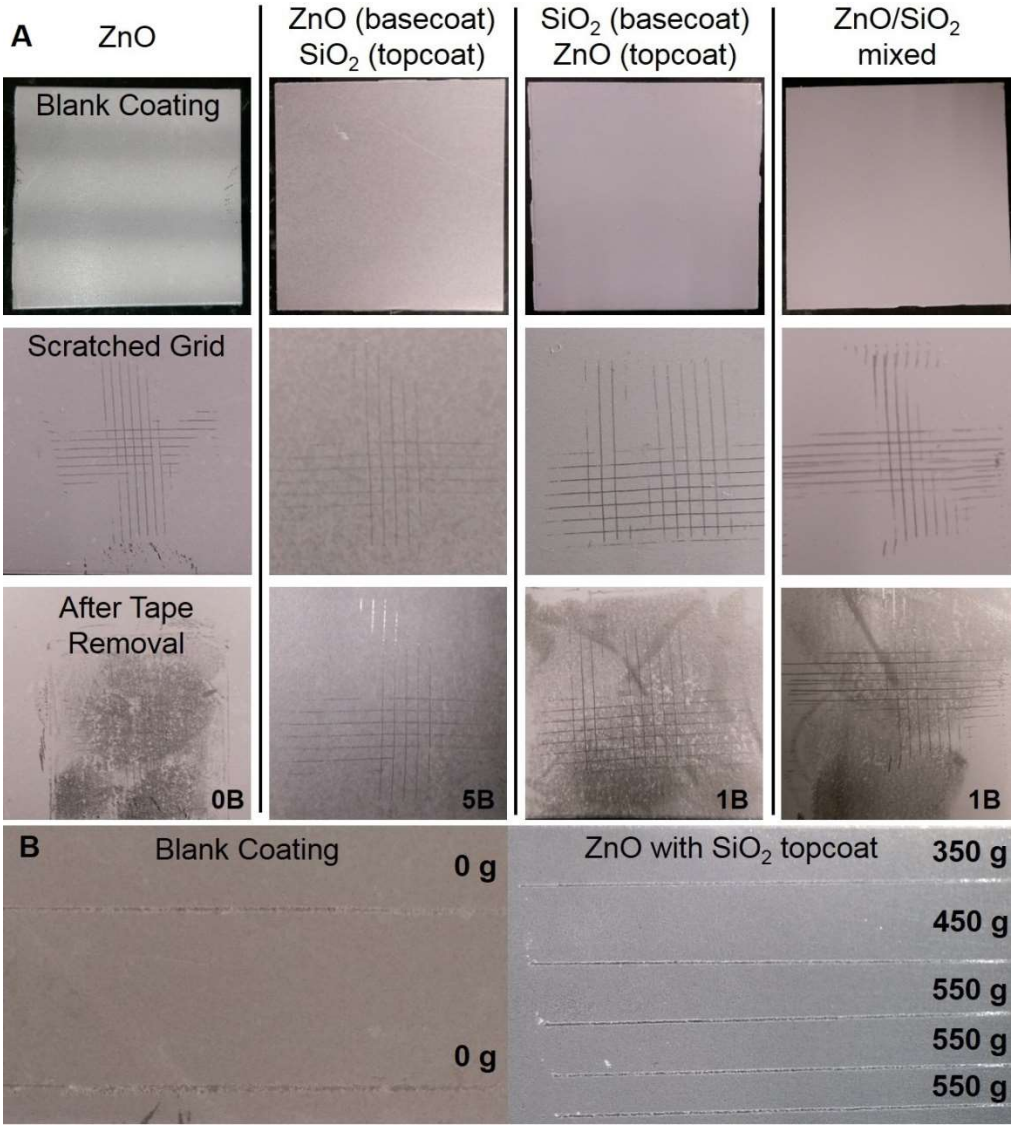

Figure A.1. Three different configurations of ZnO nanotetrapods on A36 steel were tested with ASTM D3359 (A). The configuration with a topcoat of TEOS exhibiting drastically improved adhesion with the highest rating of 5B. The top row of A demonstrates the pristine ZnO with a TEOS coating on top; the middle row represents the samples after scribing using a specified scribing tool; and the bottom row displayes the coatings after application and removal of a standardized adhesive tape. ASTM D2197 testing (B) was performed on the sample configuration of ZnO basecoat with a TEOS topcoat. Comparing unmodified ZnO scrape test (B, left) to that of ZnO with a SiO_2 topcoat (B, right) an improvement of 405-550 g was noted.

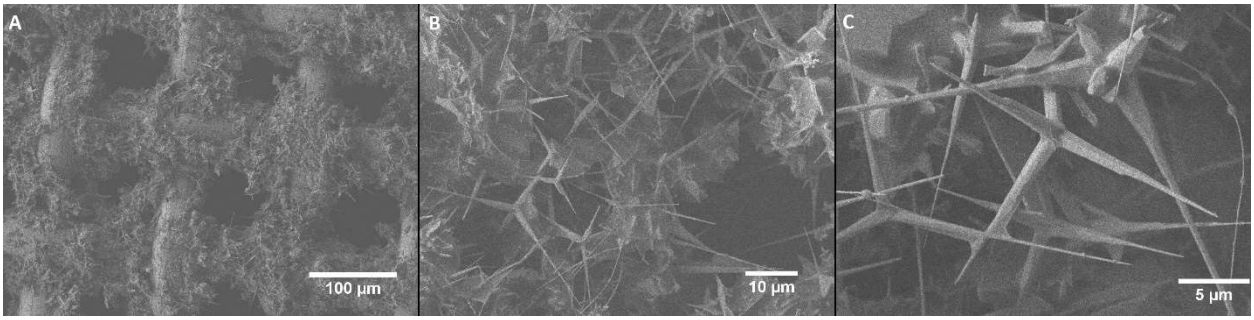

Figure A.2. SEM images at increasing magnification from A to C of ZnO tetrapods integrated onto a stainless steel mesh after functionalization with heptadecafluoro-1,1,2,2-tetrahydrodecyl)trimethoxysilane. The interconnected network of nanotetrapods is preserved after functionalization.

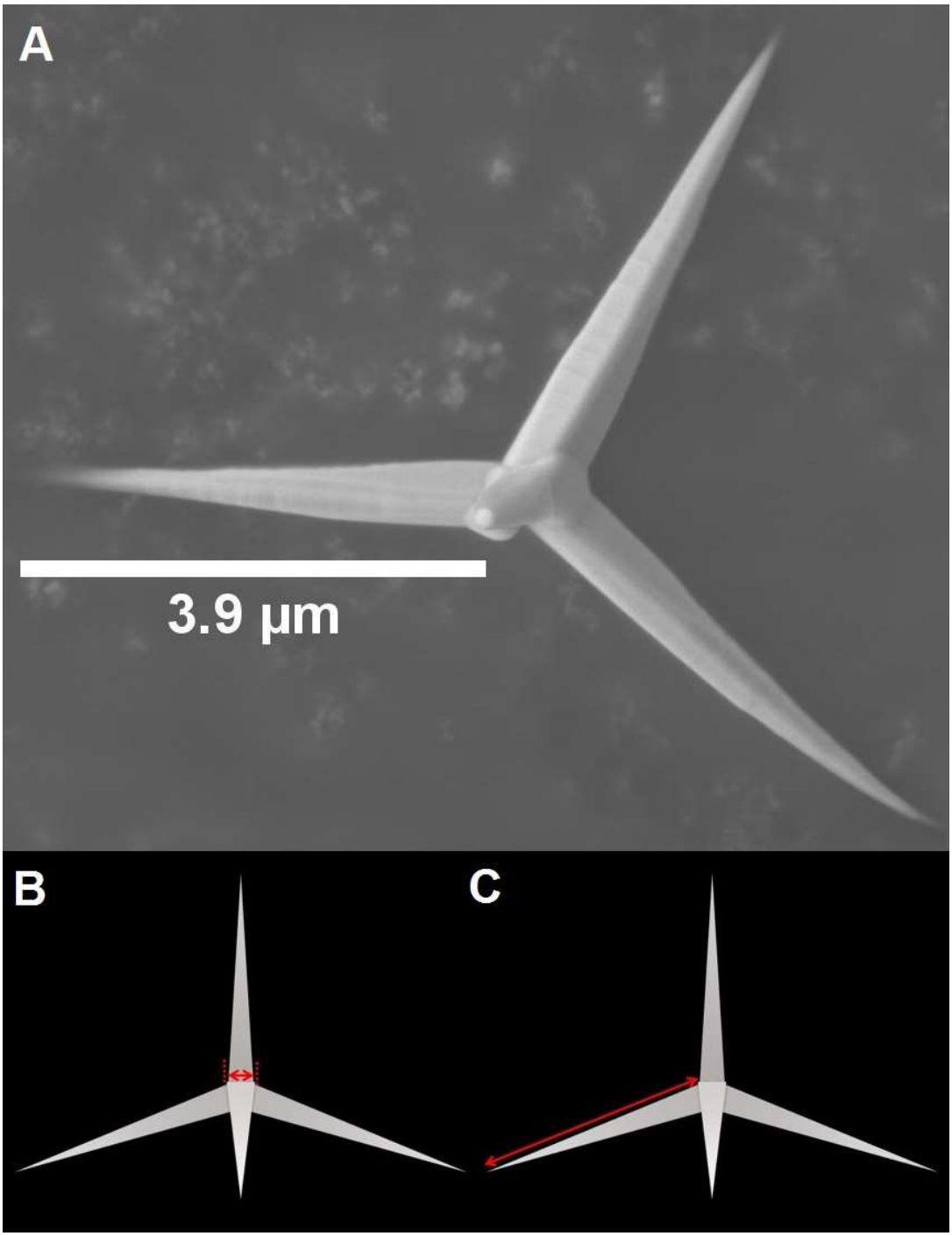

Figure A.3. (A) SEM image of an individual ZnO tetrapod. The average length of each of the tetrapod arms is ca. 3.93 µm the average diameter is ca. 0.56 µm. (B), (C) Geometrical reconstruction of the tetrapods approximating the arms as cones. A roughness *r* value of 4.5, is deduced based on these dimensions, and is defined as the ratio of the surface area of an individual tetrapod as compared to the surface area of a smooth surface.

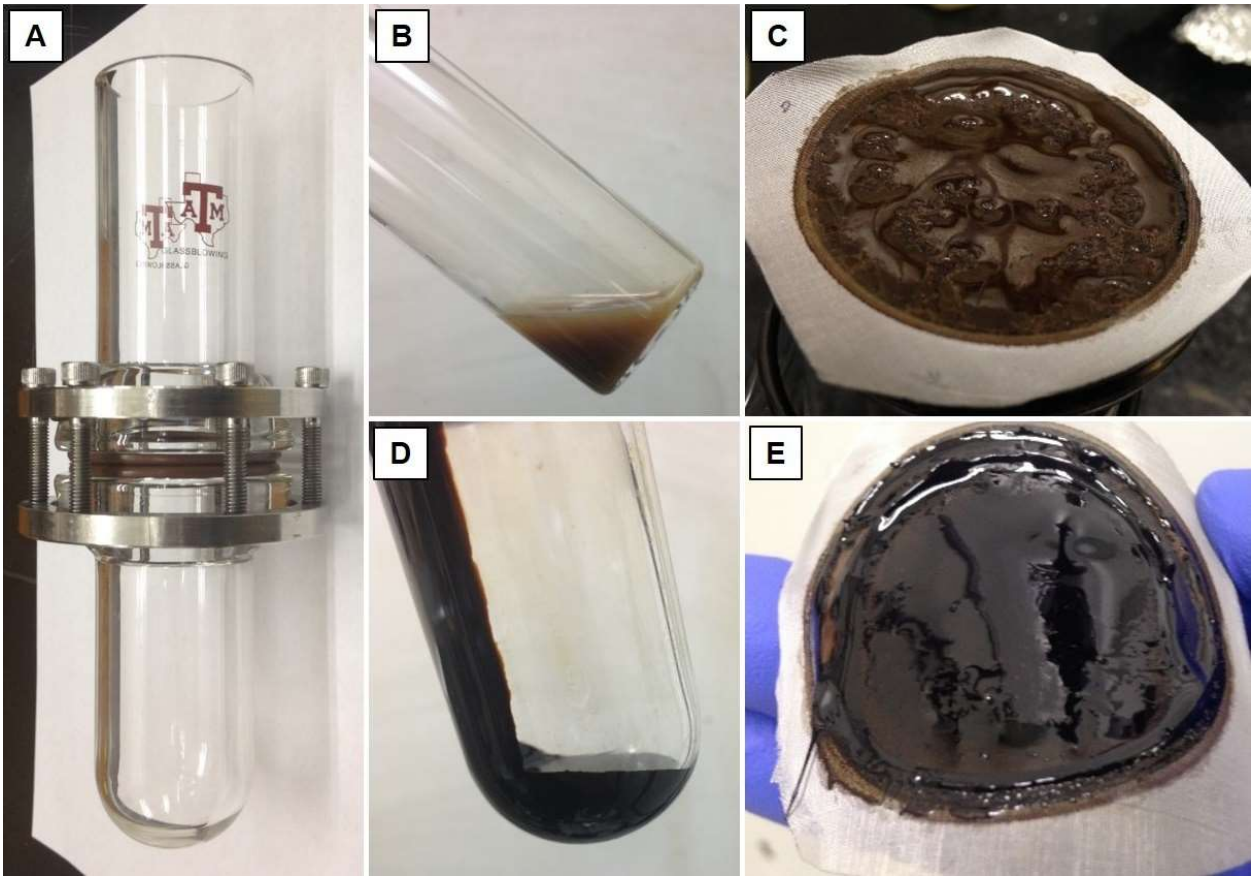

Figure A.4. Digital photographs acquired before and after separation of the emulsion. (A) A custom glass insert where the ZnO-tetrapod-coated stainless steel mesh is held between rubber o-rings and the emulsion is placed on top and allowed to permeate at a programmed temperature and pressure. (B) A decanted portion of the fraction that remains on top of the membrane. The brown coloration is characteristic of produced water contains clay and silt debris. (C) Digital photograph of the top of the membrane containing retained water with soil debris. The membrane utilized in this instance comprises a 180 gauge mesh with a pore-size of 84 μm with a ZnO loading of 7.0 mg/cm^2. (D) The permeated oil, which is darker in color as compared to the original emulsion and contains no visible water. (E) Digital photograph of the bottom of the membrane. The black color is characteristic of permeated viscous oil.

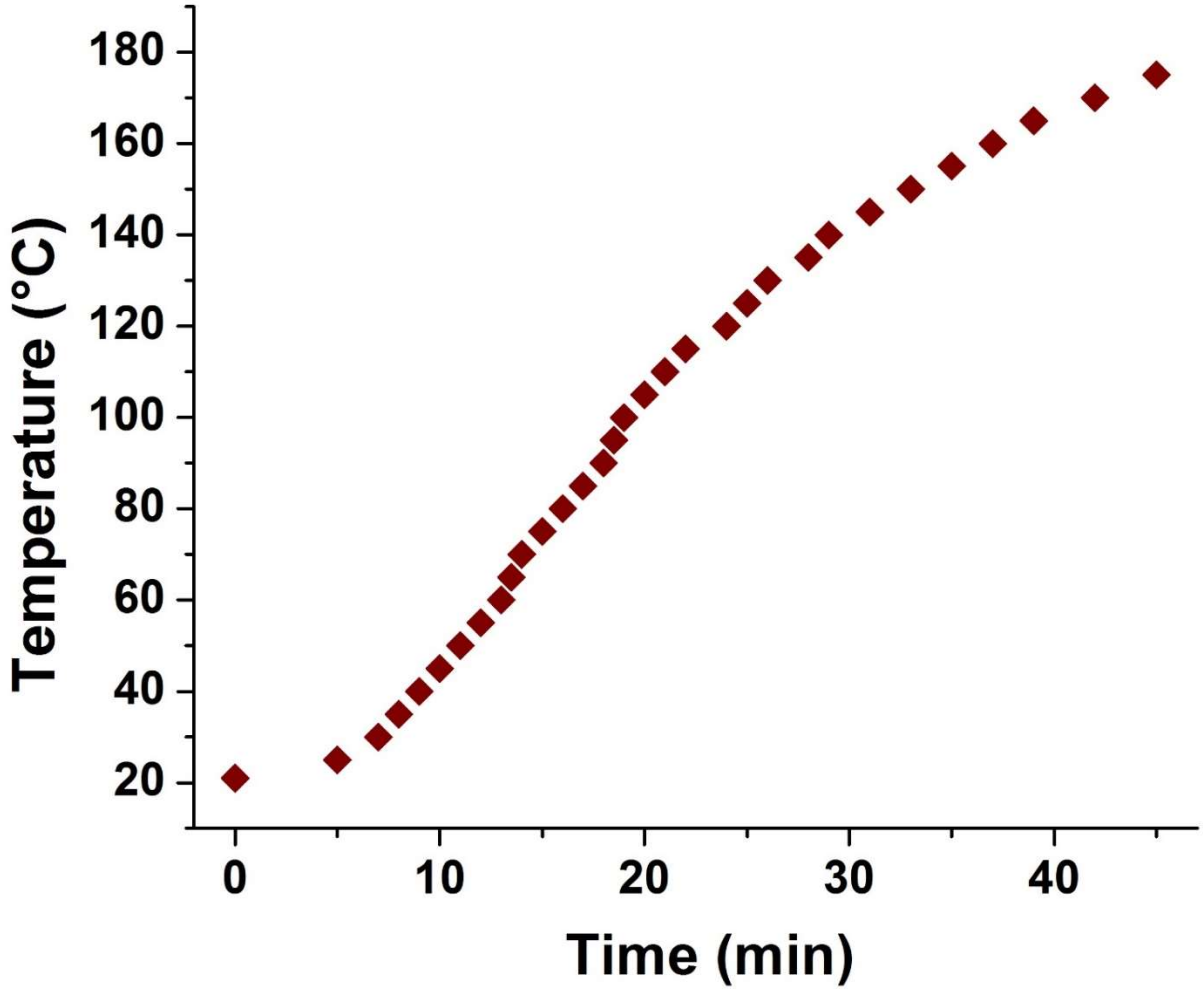

Figure A.5. Heating rate of the thermal autoclave as a function of time. The autoclave vessel is filled with 250 mL of deionized water in order to generate steam and replicate the high temperature and pressure conditions characteristic of the SAGD process. The vessel is heated from room temperature (22°C.) to a maximum temperature of 175°C.

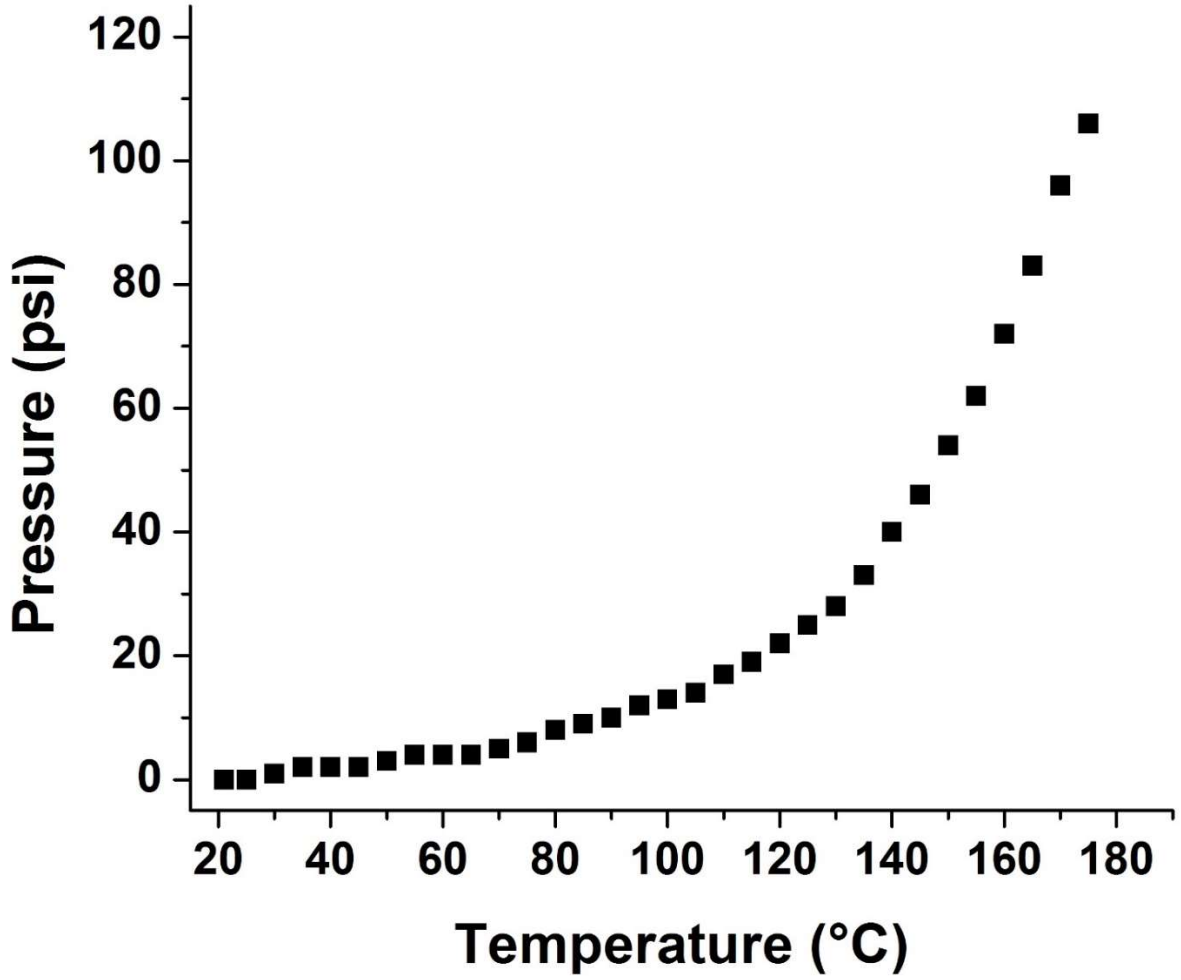

Figure A.6. Evolution of autogenous pressure as a function of temperature upon heating water within the thermal autoclave used for separation of SAGD emulsions. In this experiment, the autoclave vessel is filled with 250 mL of deionized water in order to generate steam and replicate the high temperature and pressure conditions characteristic of the SAGD process. The vessel is heated from room temperature (22°C) to a maximum temperature of 175°C yielding a maximum pressure of 106 psi at the highest temperature.

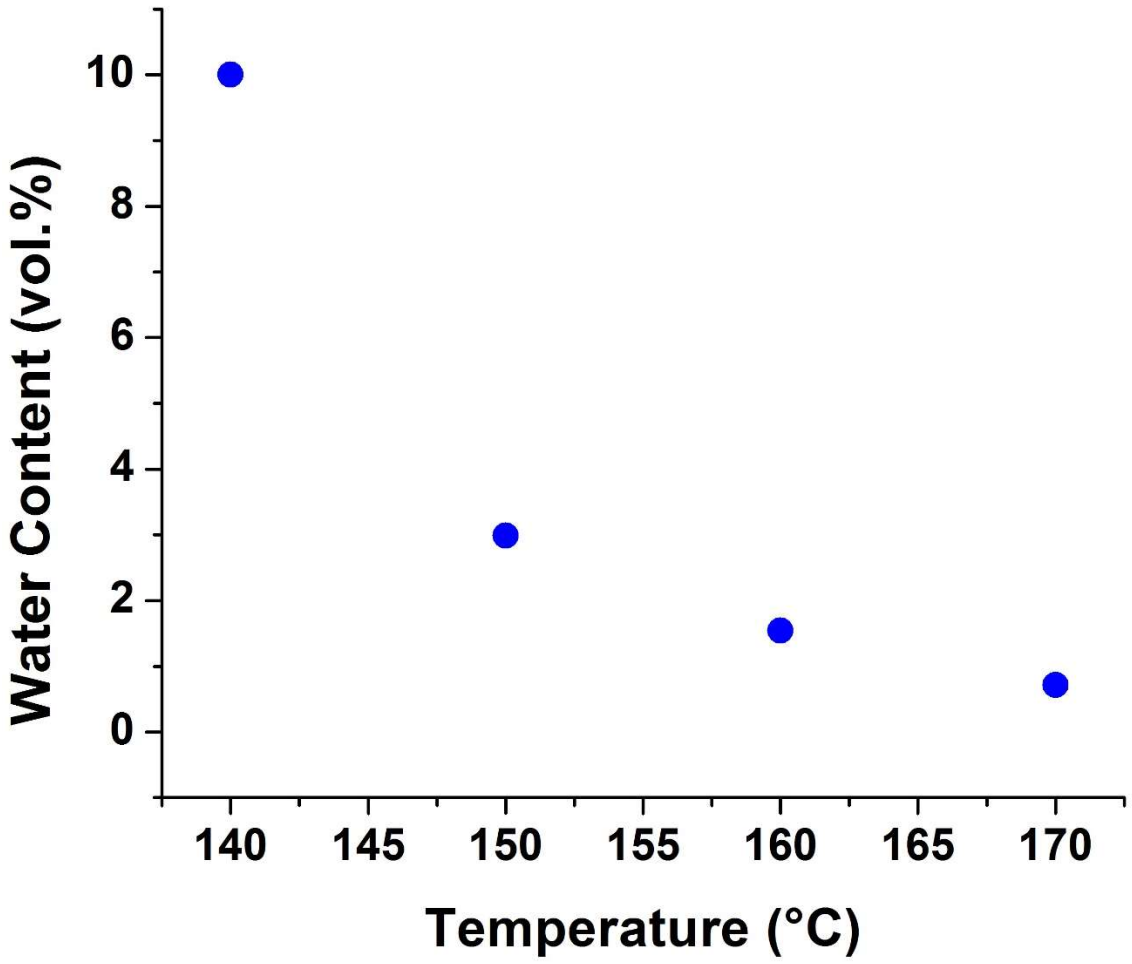

Figure A.7. Plot of water content in the permeate fraction as a function of temperature for separated using a 325-gauge stainless steel mesh with a pore size of 43 μm and a loading of 14 mg/cm^2 of ZnO tetrapods.

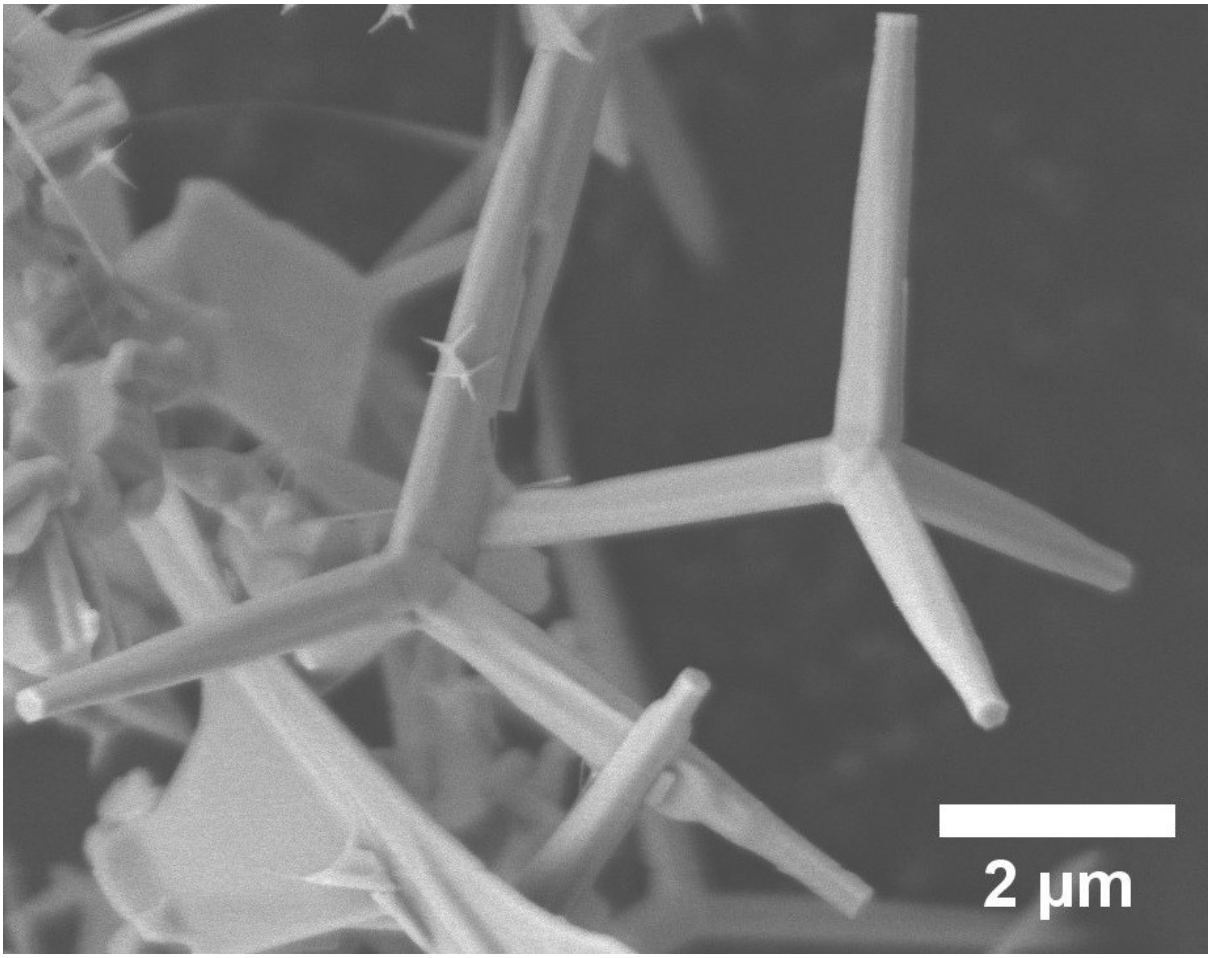

Figure A.8. SEM image of ZnO tetrapods after surface functionalization with PFOPA. No discernible changes in morphology are observed upon functionalization.

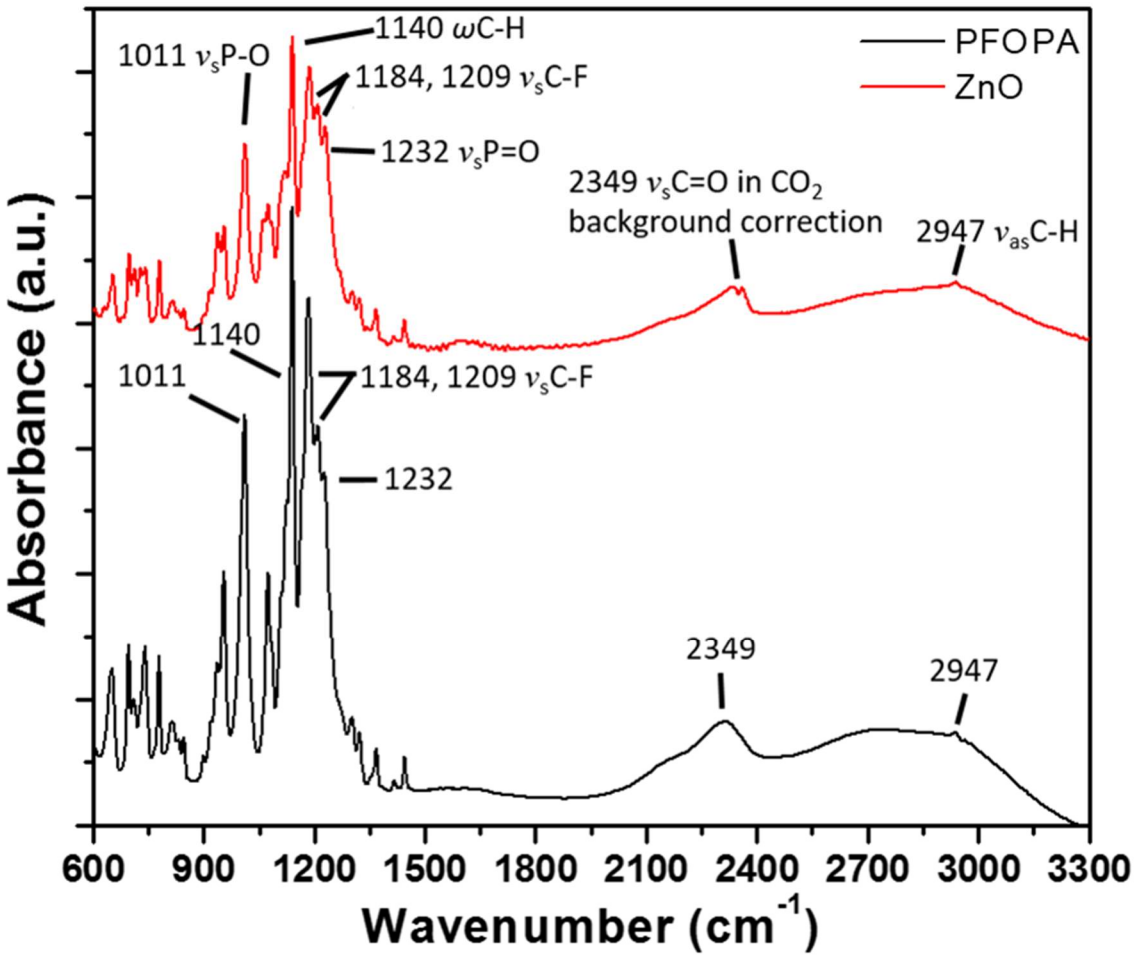

Figure A.9. FTIR ATR spectra of PFOPA (black) and PFOPA-functionalized ZnO tetrapods (red).

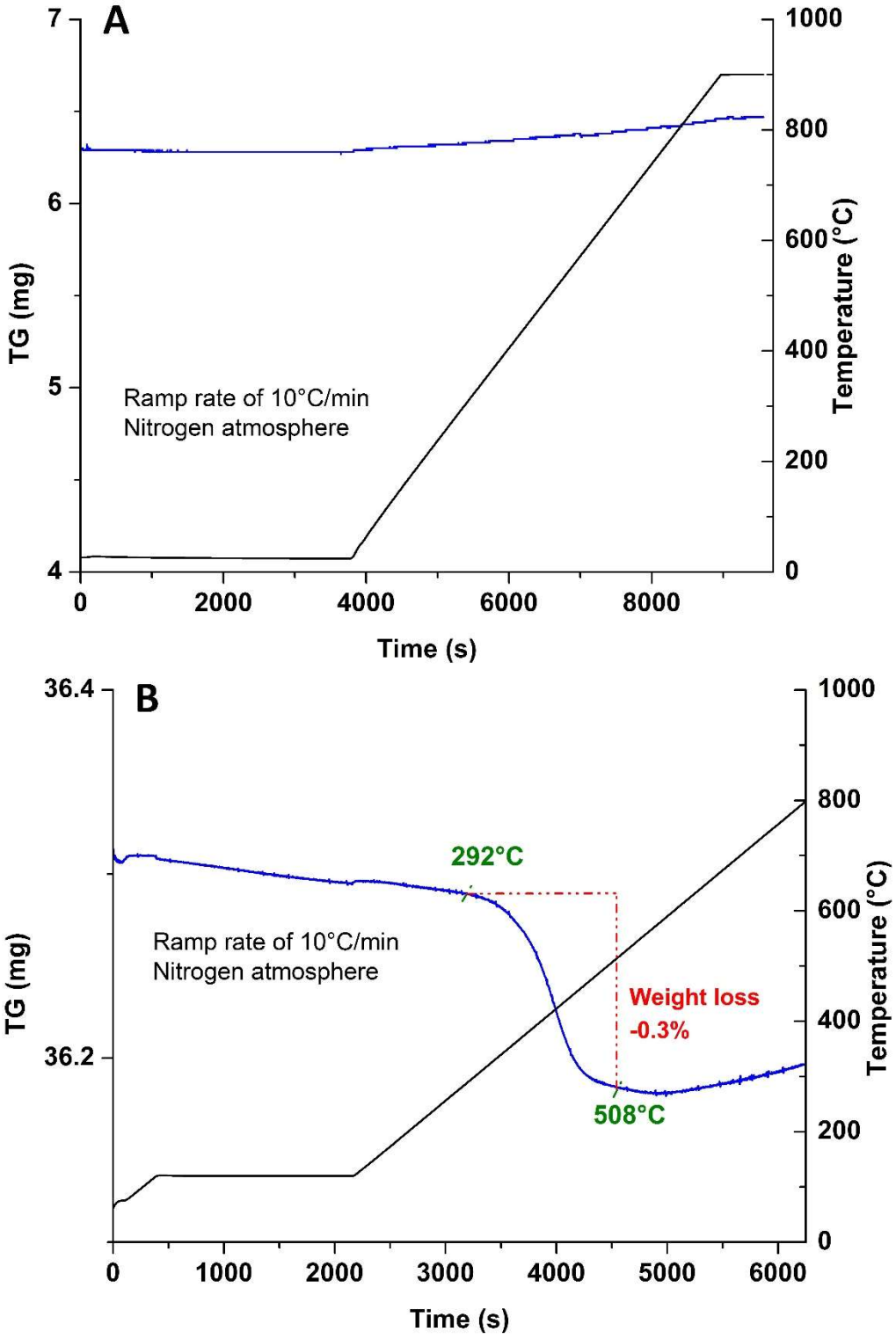

Figure A.10. Thermogravimetric analysis of (A) ZnO tetrapods and (B) PFOPA-functionalized ZnO tetrapods.

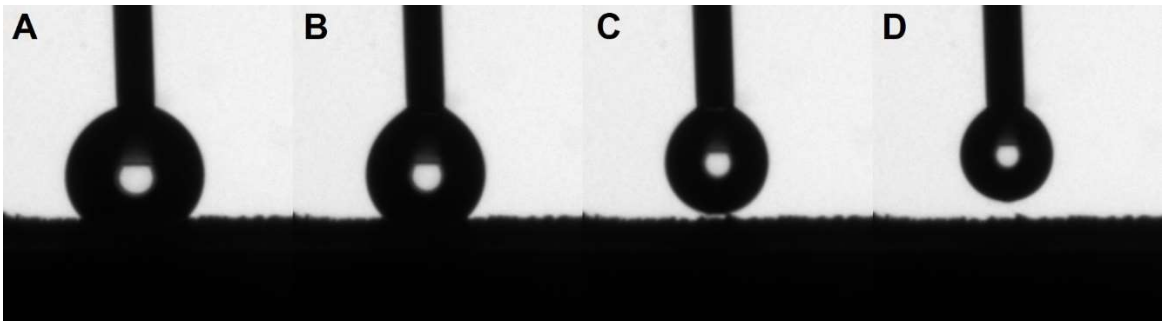

Figure A.11. Images of contact angles of water on a PFOPA functionalized ZnO coated stainless steel mesh. Here the droplets contact the surface (A) and are completely removed during the dynamic angle measurements (B-D) due to the extreme hydrophobic behavior, precluding an accurate measurement while displaying the complete inability of water to adhere to the surface.